

# SUPERPARAMAGNETIC CONTRAST AGENTS FOR MAGNETIC RESONANCE IMAGING

by

Tueng Shen

B.A., Wellesley College  
1989

Submitted to the Harvard University-Massachusetts Institute of Technology  
Division of Health Sciences and Technology  
in partial fulfillment of the requirements for the degree of

Doctor of Philosophy

in Medical Engineering and Medical Physics

at the

MASSACHUSETTS INSTITUTE OF TECHNOLOGY

April 1994

© Tueng Shen, 1994


The author hereby grants to MIT permission to reproduce  
and to distribute copies of this thesis document in whole or in part.

MIT LIBRARIES

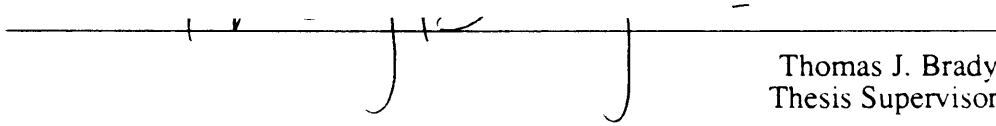
JUL 18 1994

SCHERING

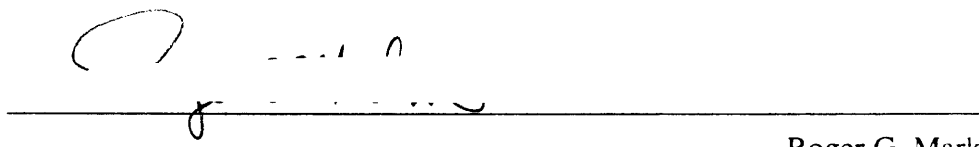
Signature of Author

  
Harvard University/Massachusetts Institute of Technology  
Division of Health Sciences and Technology  
April, 1994

Certified by

  
Thomas J. Brady  
Thesis Supervisor

Accepted by

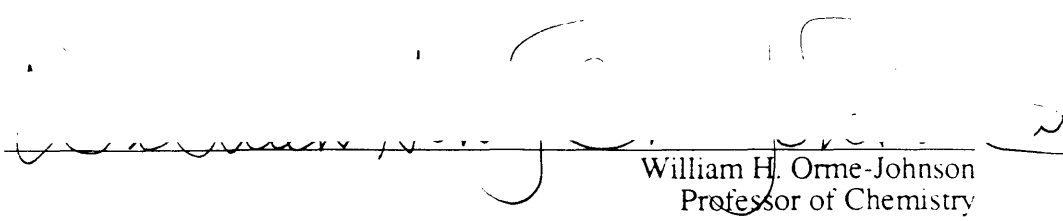
  
Roger G. Mark  
Chairman, Committee on Graduate Students  
MASSACHUSETTS INSTITUTE  
OF TECHNOLOGY

MAY 02 1994

LIBRARIES

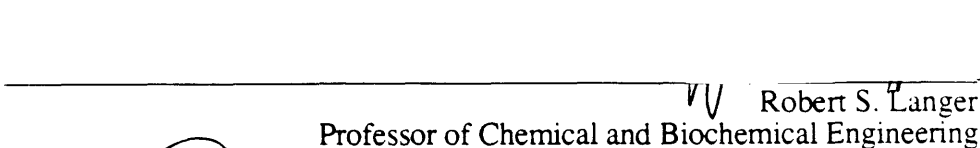
SCHEMATIC

Certified by

A handwritten signature in black ink, appearing to read 'William H. Orme-Johnson', is written over a horizontal line. The signature is somewhat cursive and spans most of the line.

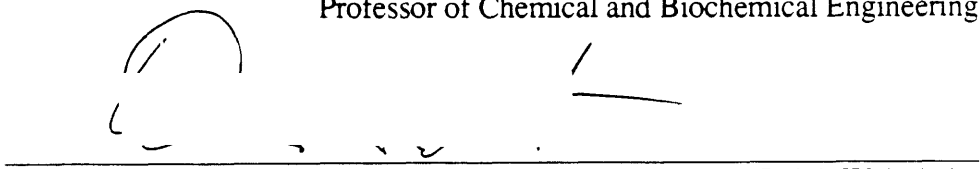
William H. Orme-Johnson  
Professor of Chemistry

Certified by

A handwritten signature in black ink, appearing to read 'Robert S. Langer', is written over a horizontal line. The signature is more formal and spans most of the line.

Robert S. Langer  
Professor of Chemical and Biochemical Engineering

Certified by

A handwritten signature in black ink, appearing to read 'Ralph Weissleder', is written over a horizontal line. The signature is somewhat cursive and spans most of the line.

Ralph Weissleder  
Thesis Co-supervisor

# SUPERPARAMAGNETIC CONTRAST AGENTS FOR MAGNETIC RESONANCE IMAGING

Tueng Shen

Submitted to the Harvard University-Massachusetts Institute of Technology  
Division of Health Sciences and Technology  
on April 29, 1994 in partial fulfillment of the requirements for the degree of  
Doctor of Philosophy in Medical Engineering/Medical Physics

## Abstract

Magnetic resonance imaging (MRI) is a non-invasive, sensitive diagnostic tool with high spatial resolution that provides detailed anatomic information. However, the diagnostic accuracy can be limited by the lack of inherent difference between normal and pathologic tissues. Under these circumstances, it is necessary to administer MR contrast agents which selectively alter the tissue characteristics by changing the magnetic environment of the region of interest. Currently, the only MR contrast agent approved for clinical use is gadolinium diethylenetriaminepentaacetic acid (Gd-DTPA), a paramagnetic agent which non-specifically enhances the longitudinal relaxation rate of protons in tissues. However, Gd-DTPA requires high tissue concentrations to be detectable by MR, making it less suitable for target-specific MRI.

Superparamagnetic iron oxides have much higher magnetic moments, and therefore require a lower dose for similar contrast enhancement. A prototype of a superparamagnetic monocrystalline iron oxide nanocompound (MION) has been synthesized and characterized as a universal magnetic label for target-specific MR imaging. The physicochemical properties of MION were characterized using high resolution transmission electron microscopy (HRTEM), X-ray diffraction, column chromatography, spectrophotometry, Mössbauer spectroscopy, and relaxometry. MION fulfills the criteria for a targetable agent with its small size (size of central iron oxide containing core  $4.6 \pm 1.2$  nm) allowing passage through the capillary endothelium while still retaining superparamagnetic behavior. Further studies of pharmacological properties and *in vivo* MR imaging in animal models demonstrated that MION can be delivered to a variety of targets, including human receptor systems, antigenic sites, and intracellular structures. This approach opens new avenues to *in vivo* MR imaging in both medicine and research.

Thesis Advisors: Thomas J. Brady, M.D.  
Ralph Weissleder, M.D., Ph.D.  
Thesis Committee: William H. Orme-Johnson, Ph.D.  
Robert S. Langer, Sc.D.

## **Acknowledgments**

It is finally spring, and it is thundering outside. As I print the last pages of this thesis, and look back at my graduate career, it seems to have been such a long winter. This portion of my thesis has been thought of and visited most often during the past five years, especially during difficult times because many people have contributed to make this work possible.

I was most privileged to have Professor Thomas J. Brady as my thesis advisor, who has guided each important step of my graduate career. He has been a mentor whom I have always been able to count on for advice and support. Professor Brady has given me tremendous independence in research, yet he has always been there in good spirit just when I needed help the most.

It has been a wonderful experience to be a student of Professor Ralph Weissleder. Ralph has taught me the ways of doing research hand in hand, and his enthusiasm and devotion to research have been my constant envy and inspiration.

I am thankful to Professor Bruce Rosen for providing me the opportunity to explore many research projects in the MGH-NMR Center at the beginning of my graduate career, and especially for introducing me to my thesis advisor Professor Brady.

I am indebted to all the collaborators at MIT and MGH who have taught me many techniques necessary for my thesis research. I have learned a great deal from all of you: Dr. G. Papaefthymiou and Dr. S. Foner for the characterization of magnetic properties, especially by SQUID and Mössbauer spectroscopy; Dr. Q. Li for offering his expertise on SEM and TEM; Dr. W. Gao for the X-ray analysis of iron oxides, and Dr. B. Foy for providing reliable hepatocytes for the cell experiments.

I am grateful to all the members (past and present) of MRPP for their encouragement; I am appreciative to the colleagues at the MGH-NMR Center, for their helpful advice and fruitful discussions which made my research more enjoyable.

I was the first student coming to MEMP through the department of Chemistry. I thank Professor Roger G. Mark, Professor William H. Orme-Johnson, Professor Robert S. Langer and many other faculty members in both HST and Chemistry for their advice and effort which guided me through this process.

There are several people who have been instrumental as educators, and who have changed my life through education for the better.

I wish to thank Professor Nancy H. Kolodny, my undergraduate thesis advisor, for being a great mentor and a role model, especially in the difficult times through graduate school.

I would like to thank my grandfather Qing Nang Shen for educating me by his devotion to science, his constant optimism and effort to use science to better the world, despite of the war and political chaos he lived in. It is, however, most regretful that, by difference of one month, my grandfather could not see the completion of this document for himself.

The encouragement and sacrifices of my parents have provided me constant motivation to venture into this new world. They have been my first and best teachers. Without Lu's humor and naughtiness, life could never be as much fun. I am fortunate to have a sister who is one of my closest friends in this world.

I would like to thank Jan for his trust in my abilities, his encouragement and support to my studies and his understanding of me working during many weekends and holidays. I am grateful that although most unexpectedly, we had the chance to journey through the ups and downs of graduate school at MIT together. This will be part of our most memorable experiences as we look ahead for a life together for many years to come.

# Contents

<b>Abstract .....</b>	<b>3</b>
<b>Acknowledgments.....</b>	<b>4</b>
<b>Contents.....</b>	<b>5</b>
<b>List of figures.....</b>	<b>7</b>
<b>List of tables.....</b>	<b>9</b>
<b>Chapter I Introduction .....</b>	<b>10</b>
1.1 Historic Aspects of NMR.....	10
1.2 Magnetic Resonance Imaging (MRI) .....	12
1.3 MR Contrast Agents.....	25
1.3.1 Relaxivity .....	25
1.3.2 Classification .....	26
1.4 Research Objectives .....	30
<b>Chapter II Background.....</b>	<b>31</b>
2.1 Magnetic Materials.....	31
2.1.1 Structures and Properties .....	32
2.1.2 Ferrites .....	37
2.2 Magnetic Iron Oxides.....	41
2.2.1 Physical Properties of Iron Oxides .....	41
2.2.2 Reaction Mechanisms .....	42
<b>Chapter III Synthesis .....</b>	<b>49</b>
3.0 An ideal Biocompatible Iron Oxide .....	49
3.1 Core Structure.....	52
3.2 Core Size.....	57
3.3 Stability .....	63
3.3.1 Polymeric Stabilizing Agents.....	63
3.3.2 Effect of Surface Coating on Magnetic Properties .....	64
3.3.3 Stability of MION.....	66
3.4 Conjugation to Carrier Molecules.....	68
3.5 Summary.....	71

---

<b>Chapter IV</b>	<b>Physicochemical Characterization .....</b>	<b>72</b>
4.1	Crystal Structure .....	73
4.2	Particle Size.....	77
	4.2.1 Electron Microscopy (EM) Analysis.....	77
	4.2.2 Hydrodynamic Radii by LLS.....	79
4.3	Magnetic Properties of the Core.....	82
	4.3.1 Superconducting Quantum Interference Device (SQUID) .....	82
	4.3.2 Mössbauer Spectroscopy .....	86
	4.3.3 NMR Relaxation Studies.....	90
4.4	Chemical Composition .....	91
4.5	Summary.....	94
<b>Chapter V</b>	<b>Biological Interactions .....</b>	<b>95</b>
5.1	Cellular Toxicity .....	95
	5.1.1 Preparation of Hepatocyte Culture.....	95
	5.1.2 Enzyme-linked Immunosorbent Assay (ELISA).....	97
	5.1.3 MION Incubation .....	98
5.2	Interaction with Blood Components.....	100
5.3	Blood half-lives of MION .....	102
<b>Chapter VI</b>	<b>In vivo MR Imaging .....</b>	<b>105</b>
6.1	Conventional MR Imaging.....	105
	6.1.1 Animal Preparation .....	105
	6.1.2 Imaging Experiment.....	105
6.2	Fast in vivo MR Imaging of MION and MION-ASF.....	108
<b>Chapter VII</b>	<b>Conclusion .....</b>	<b>110</b>
<b>References</b> .....		<b>115</b>
<b>Appendix (Facilities)</b> .....		<b>118</b>

## **List of figures**

Figure 1.1	Nuclei spin .....	12
Figure 1.2	Energy levels of a spin system.....	14
Figure 1.3	Radio Frequency Pulses.....	17
Figure 1.4	Relaxation process .....	19
Figure 1.5	Measurement of T1 .....	20
Figure 1.6	Measurement of T2 (CPMG pulse sequence).....	21
Figure 1.7	Synthesis of Image contrast from a spin echo pulse sequence.....	24
Figure 2.1	Schematics of spin arrangements in different magnetic materials .....	35
Figure 2.2	Saturation magnetization of ferrites verses temperature .....	40
Figure 2.3	Reaction mechanism in aqueous solution .....	47
Figure 3.1	MION: An ideal picture.....	50
Figure 3.2	Schematics of iron oxide synthesis .....	51
Figure 3.3	Schematic representation of the ratio experiments.....	53
Figure 3.4	X-ray diffraction spectra of iron oxides .....	56
Figure 3.5	Core size optimization experiment set-up .....	59
Figure 3.6	Scanning electron micrographs of freeze-dried MION preparations .....	60
Figure 3.7	Particle size distribution of two preparations from Figure 3.6.....	61
Figure 3.8	The effect of initial reaction temperature on the average particle size .....	62
Figure 3.9	The effect of polymeric stabilizing agents on colloidal solution .....	64

Figure 3.10	Attachment of IgG to MION.....	69
Figure 4.1	Organization of physicochemical characterization techniques.....	73
Figure 4.2	X-ray powder diffraction spectrum of MION .....	75
Figure 4.3	Diffraction pattern of a single crystal MION core.....	76
Figure 4.4	A high resolution electron micrograph of a MION preparation.....	78
Figure 4.5	Schematics of laser light scattering equipment.....	80
Figure 4.6	A typical LLS measurement of MION in aqueous solution .....	81
Figure 4.7	Schematic representation of SQUID.....	84
Figure 4.8	Induced magnetization.....	85
Figure 4.9	Schematics of Mössbauer Experiment.....	88
Figure 4.10	Mössbauer spectra of MION-37 at various temperatures.....	89
Figure 4.11	A Typical relaxivity plot of MION .....	90
Figure 4.12	Molecular model of a monocrystalline iron oxide nanocompound.....	93
Figure 5.1	The albumin secretion rate of hepatocytes.....	99
Figure 5.2	Experimental set-up of the interactions of MION with blood.....	101
Figure 5.3	MION association with components of whole rat blood .....	102
Figure 5.4	A typical blood half-life plot of an unlabeled MION in rats.....	104
Figure 6.1	In vivo liver signal reduction by MION .....	107
Figure 6.2	In vivo liver signal intensity of MION and MION-ASF.....	109



## **List of tables**

Table 1.1	Common biologically relevant NMR-detectable isotopes .....	15
Table 1.2	Classification of MR Contrast Agents .....	28
Table 1.3	Currently available MR Contrast Agents .....	29
Table 2.1	Classification of materials according to magnetic properties.....	34
Table 2.2	Properties of Ferrites .....	39
Table 2.3	Physical properties of iron oxides.....	41
Table 3.1	Ratio Experiments.....	55
Table 3.2	Effects of surface coatings on relaxivity.....	65
Table 3.3	Thermal stability evaluation.....	66
Table 4.1	Lattice spacings in MION crystal.....	74
Table 4.2	Chemical composition of two MION preparations.....	92
Table 5.1	Blood half-lives of MION samples .....	104
Table 6.1	Relative signal intensity change .....	106

# Chapter I

## Introduction

The purpose of this chapter is to put this thesis research in the broader perspective of the rapidly expanding field of nuclear magnetic resonance (NMR or MR) in medicine. Basic principles of the NMR phenomenon are briefly reviewed in this chapter. Emphasis is placed on the parameters most relevant to this thesis research. Several important building blocks of MR imaging techniques such as radio frequency (RF) pulses and common imaging pulse sequences are briefly described. Classification of MR contrast agents and their relaxation mechanisms is then introduced to derive important prerequisites of useful superparamagnetic contrast agents.

### 1.1 Historic Aspects of NMR

In 1939 Rabi and his co-workers conducted the following experiment: A beam of hydrogen molecules was sent, first through an inhomogeneous magnetic field, and then through a homogeneous one in which radio frequency electromagnetic energy was applied to the molecules. At a sharply-defined frequency, this energy was absorbed by the molecular beam. Consequently the beam underwent a small deflection. This was the first observation of nuclear magnetic resonance (NMR), but it was performed under very high vacuum (Rabi, Millman et al. 1939). It was not until 1946, that Purcell, Torrey and Pound at Harvard University, and Bloch, Hansen and Packard at Stanford University, simultaneously demonstrated the phenomenon of NMR in bulk materials, such as paraffin wax and water, in the liquid state (Bloch, Hansen et al. 1946; Purcell, Torrey et al. 1946). Both groups received the Nobel Prize in 1952 for this discovery. Shortly after Purcell and

Bloch discovered the phenomenon of NMR in solids and liquids, it was found that the precise resonance frequency of a nucleus depends upon the state of its chemical environment (Knight 1949; Dickinson 1950; Lindström 1950; Proctor and Yu 1950). In 1951, separate resonance lines were observed for chemically different protons (Arnold, Dharmatti et al. 1951) in the same molecule. Since then, NMR has become increasingly important in all branches of chemistry. For example, the combination of proton ( $^1\text{H}$ ) and carbon-13 ( $^{13}\text{C}$ ) NMR spectroscopy provides an important probe which is widely exploited by organic chemists for solving structural problems of organic molecules. The NMR technique has also been applied to the studies of complex molecules with biological significance, providing, for example, structural information on proteins and nucleic acids. In 1971, the potential of NMR to discriminate between different tissues was recognized by Damadian (Damadian 1971). In 1973, Lauterbur successfully produced the first MR image from a conventional NMR spectrometer with addition of linear magnetic field gradients to incorporate the spatial information of protons for magnetic resonance imaging (MRI; Lauterbur 1973). The potential of such a technique for diagnostic medicine was immediately realized. During the past two decades, facilitated by further improvements in instrumentation (superconducting magnets and faster computers) and the employment of imaging techniques (back-projection or two-dimensional Fourier image reconstruction (Housefield and Ambrose 1973; Kumar, Welti et al. 1975)), MR imaging and spectroscopy techniques have become available for non-invasive clinical studies of human anatomy and metabolism. For example, in United States alone, the number of operational MR imaging facilities increased from 3 in 1981 to more than 1500 in 1992. MR imaging techniques have the advantage over other imaging techniques, such as Computed Tomography (CT), to provide high soft tissue contrast while not employing ionizing radiation (Fisher, Wall et al. 1985). For these reasons, MRI has become a routine clinical tool for the diagnosis of many pathological conditions and for evaluating metabolic functions.

## 1.2 Magnetic Resonance Imaging (MRI)

### Fundamental principles

MRI makes use of a unique physical property of nuclei with odd mass number which have the property of spin (figure 1.1). The spin angular momentum can be expressed as in equation 1.1:

$$\mu_N = \gamma_N \cdot \frac{h}{2\pi} \cdot I \quad (1.1)$$

where  $\mu_N$  is the magnetic moment of the nucleus, and  $\gamma_N$  is the magnetogyric ratio of the nucleus, which is a unique constant for each type of nucleus (radians $\cdot$ sec $^{-1}$  $\cdot$ Gauss $^{-1}$ ),  $h$  is Planck's constant, and  $I$  is the nuclear spin quantum number of the nucleus.

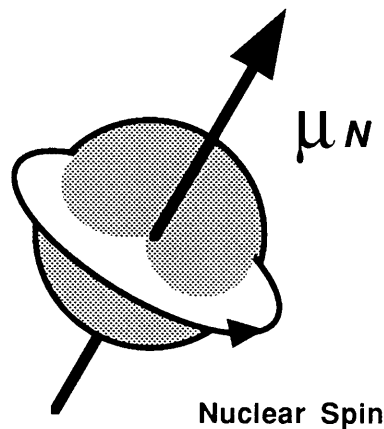


**Figure 1.1** Nuclei with odd mass number have the property of spin with the spin angular momentum  $\mu_N$  expressed as:  $\mu_N = \gamma_N \cdot \frac{h}{2\pi} \cdot I$

For example, protons ( $^1\text{H}$ ) have a nuclear spin quantum number  $I=1/2$ ,  $\gamma_N=2.6753 \times 10^4$  radians $\cdot$ sec $^{-1}$  $\cdot$ Gauss $^{-1}$  (or 42.58 MHz $\cdot$ Tesla $^{-1}$ ). Only the nuclei with spin can be detected by NMR techniques. Table 1.1 summarizes some biologically relevant MR detectable

isotopes, their nuclear spin quantum numbers and their magnetogyric ratios. In the following discussion, the proton ( $^1\text{H}$ ) will be used as an example because it is the most abundant nucleus in the body, most commonly used in MRI and therefore most relevant to this thesis.

In the absence of a magnetic field, the magnetic moments of protons in the body are oriented randomly. However, in the presence of a constant magnetic field, ( $B_0$  with direction  $z$ ), the nuclear spin states allowed ( $E_m$ ) are quantized (equation 1.2), and the quantum number  $m_I$  can only take up a set of discrete values from  $+I, (I-1), \dots -I$ .

$$E_m = -\gamma \frac{h}{2\pi} m_I B_0 \quad (1.2)$$

In the case of protons, with  $I = 1/2$ ,  $m_I$  can only take values of  $+1/2$  and  $-1/2$ . Therefore, only two nuclear spin directions [Figure 1.2], representing two energy levels that the protons occupy, are allowed. The lower energy level ( $m = +1/2$ ) corresponds to the situation that the nuclear moment aligns parallel to the steady field, and the higher energy level ( $m = -1/2$ ) represents the anti-parallel situation.

At equilibrium, the protons are distributed over the two possible energy states according to the Boltzmann distribution law:

$$\frac{N_{-\frac{1}{2}}}{N_{+\frac{1}{2}}} = e^{-\Delta E / kT} \quad (1.3)$$

where  $\Delta E$  is the energy difference between the two levels,  $k$  is Boltzmann's constant, and  $T$  is temperature in Kelvin. When an electromagnetic field perpendicular to the constant field  $B_0$  is applied to a system with a frequency  $\nu$  satisfying equation 1.4, absorption of energy occurs in the spin system and transitions take place between the two nuclear spin levels.

$$\Delta E = \nu \cdot h = \gamma \cdot \frac{h}{2\pi} \cdot B_0 \quad (1.4)$$

This frequency is defined as *resonance frequency* of the nucleus. In the case of protons again, the resonance frequency at 1.5 Tesla (common clinical field strength) is 64 MHz.

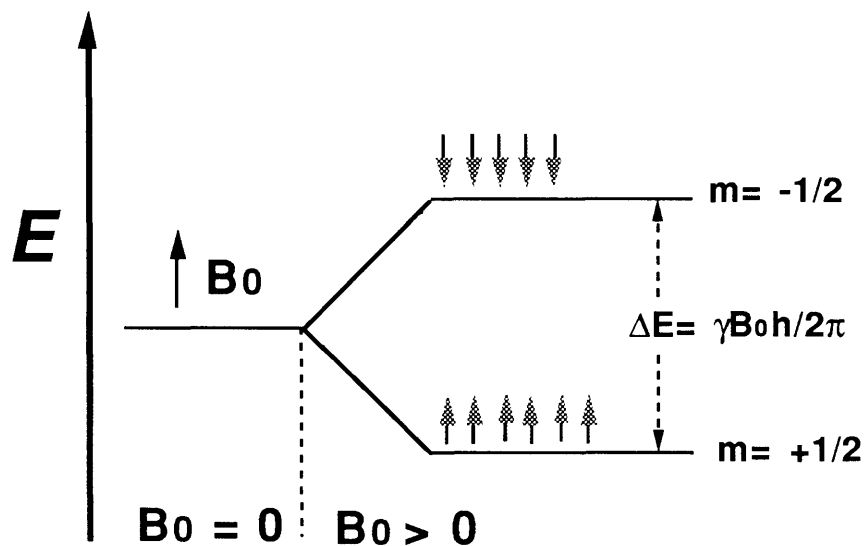


**Figure 1.2** A schematic representation of energy levels of a spin system in the absence of the magnetic field ( $B_0=0$ ) and in the presence of a steady field ( $B_0>0$ ). In the case of proton ( $I=1/2$ ), there are only two allowed nuclear spin directions in the presence of a magnetic field. The lower energy level ( $m = +1/2$ ) corresponds to the nuclear moment aligns parallel to the steady field, and the higher energy level ( $m = -1/2$ ) represents the anti-parallel situation. A typical magnetic field strength of a clinical MR imaging facility is 1.5 Tesla, corresponding to a resonance frequency of 64 MHz for protons.

**Table 1.1 Common biologically relevant NMR-detectable isotopes**

Elements	Nuclear Spin Quantum number (I)	% Natural Abundance	NMR Frequency (MHz/Tesla)
Hydrogen ( $^1\text{H}$ )	1/2	99.98	42.57
Lithium ( $^7\text{Li}$ )	3/2	92.58	16.55
Carbon ( $^{13}\text{C}$ )	1/2	1.11	10.71
Nitrogen ( $^{15}\text{N}$ )	1/2	0.36	4.31
Oxygen ( $^{17}\text{O}$ )	5/2	0.04	5.77
Fluorine ( $^{19}\text{F}$ )	1/2	100.00	40.05
Sodium ( $^{23}\text{Na}$ )	3/2	100.00	11.26
Magnesium ( $^{25}\text{Mg}$ )	5/2	10.13	2.61
Phosphorus ( $^{31}\text{P}$ )	1/2	100.00	17.23
Sulphur ( $^{33}\text{S}$ )	3/2	0.74	3.27
Chlorine ( $^{35}\text{Cl}$ )	3/2	75.53	4.17
Chlorine ( $^{37}\text{Cl}$ )	3/2	24.47	3.47
Potassium ( $^{39}\text{K}$ )	3/2	93.10	1.99
Potassium ( $^{41}\text{K}$ )	3/2	6.88	1.09
Calcium ( $^{43}\text{Ca}$ )	7/2	0.15	2.86

## RF Pulses

The energy which causes the transition of protons between the nuclear spin states can be applied in a package of radio frequency oscillations, called a radio frequency (RF) pulse. Macroscopically, the vector sum of the magnetic dipole moments of the nuclear spin system at equilibrium in the presence of  $B_0$  can be represented as  $M$  [Figure 1.3a]. Various types of RF pulses have been used in MR imaging, and the following are most common ones:

An “excitation pulse” converts the equilibrium magnetization ( $M$ ) into the transverse plane (XY). It is therefore often called a  $90^\circ$  pulse (Figure 1.3b).

A pulse which converts  $M$  into  $-M$  is a  $180^\circ$  pulse, also called an inversion pulse (Figure 1.3c). This pulse is employed at the beginning of an inversion recovery sequence which is commonly used to measure  $T_1$  relaxation times.

Another type of  $180^\circ$  pulse is employed to convert the precessing magnetization vectors of the XY plane to their mirror-image position with respect to the pulse axis (Figure 1.3d). If this pulse is applied at time  $\tau$  after a  $90^\circ$  pulse, the magnetization vectors of the spins precessing at different frequencies will start to precess in the opposite direction. Thus, at time  $2\tau$ , the magnetization vectors of the spins will refocus along the original magnetization vector, generating an echo. This pulse is often referred to as a refocusing pulse, commonly used in spin-echo experiments.



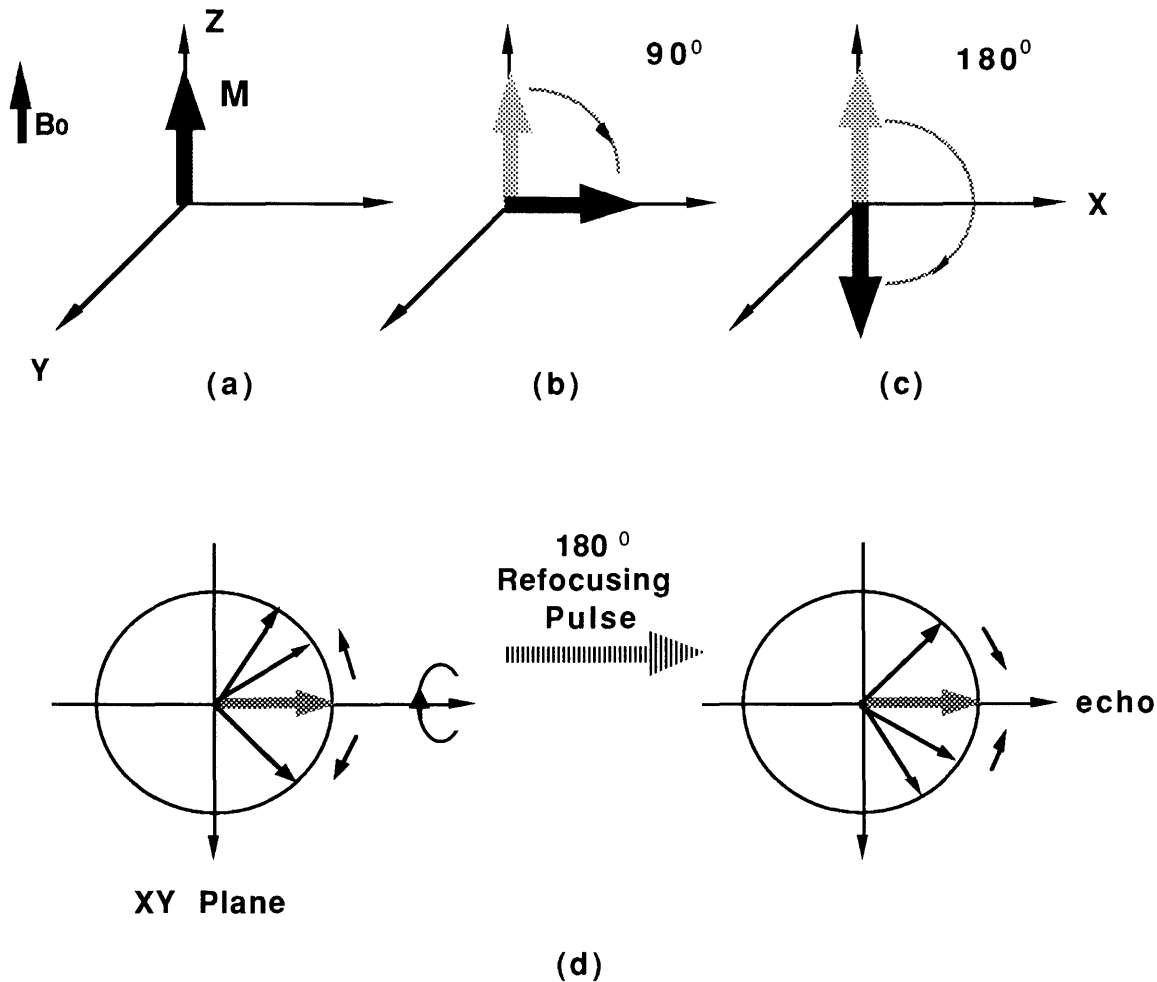


**Figure 1.3** Radio Frequency Pulses: (a) the equilibrium magnetization ( $M$ ) (b) an “excitation pulse”, or a  $90^\circ$  pulse converts  $M$  into the transverse plane ( $XY$ ) (c) an inversion pulse, or a  $180^\circ$  pulse, converts  $M$  into  $-M$  which is employed at the beginning of an inversion recovery sequence to measure  $T_1$  relaxation times (d) a refocusing pulse (another type of  $180^\circ$  pulse) converts the precessing magnetization vectors of the  $XY$  plane to their mirror-image position with respect to the pulse axis. This pulse is often used generating an echo in spin-echo experiments.

### Spin-Lattice Relaxation ( $T_1$ )

When a perturbation in the form of a RF pulse is applied,  $M$  [Figure 1.4.] tips towards the  $xy$  plane while precessing around the steady external magnetic field  $B_0$ . When this perturbation is terminated, the nuclear spin system will "relax" to the equilibrium by dissipating the excess energy to its surroundings via thermal exchange. This process is called spin-lattice relaxation and the equilibrium condition is reached by a first order process characterized by a time constant,  $T_1$ , the spin-lattice relaxation time. If a  $180^\circ$  RF pulse is applied, the recovery of  $M_z$  can be described as in equation 1.5:

$$M_z(t) = M_z(0) [1 - 2e^{-\frac{t}{T_1}}] \quad (1.5)$$

An inversion recovery pulse sequence ( $180^\circ - \tau - 90^\circ$ ) is commonly used to measure the  $T_1$  relaxation time: an inversion pulse ( $180^\circ$ ) is applied to convert  $M_z$  to  $-M_z$ , and the magnetization is allowed to recover. At a delay time  $\tau$ , a  $90^\circ$  pulse is employed. The precession of the magnetic moment around  $B_0$  (flux of  $M$ ) then induces an electric potential in the radio frequency coil, which can be measured. The experiment is repeated at different  $\tau$  values to follow the recovery process, as schematically represented in Figure 1.5.

### Spin-Spin Relaxation ( $T_2$ )

When this RF pulse is applied, the moments in the  $xy$  plane begin to lose their precessing phase coherence, due to the natural processes that cause nuclei to exchange energy with each other. As a result of this process, called spin-spin relaxation, the net  $M_{xy}$  magnetization decays to zero exponentially with time (equation 1.6), characterized by the time constant  $T_2$  which is often measured by a CPMG sequence as illustrated in figure 1.6.

$$M_{XY}(t) = M_{XY}(0) \cdot e^{-\frac{t}{T_2}} \quad (1.6)$$

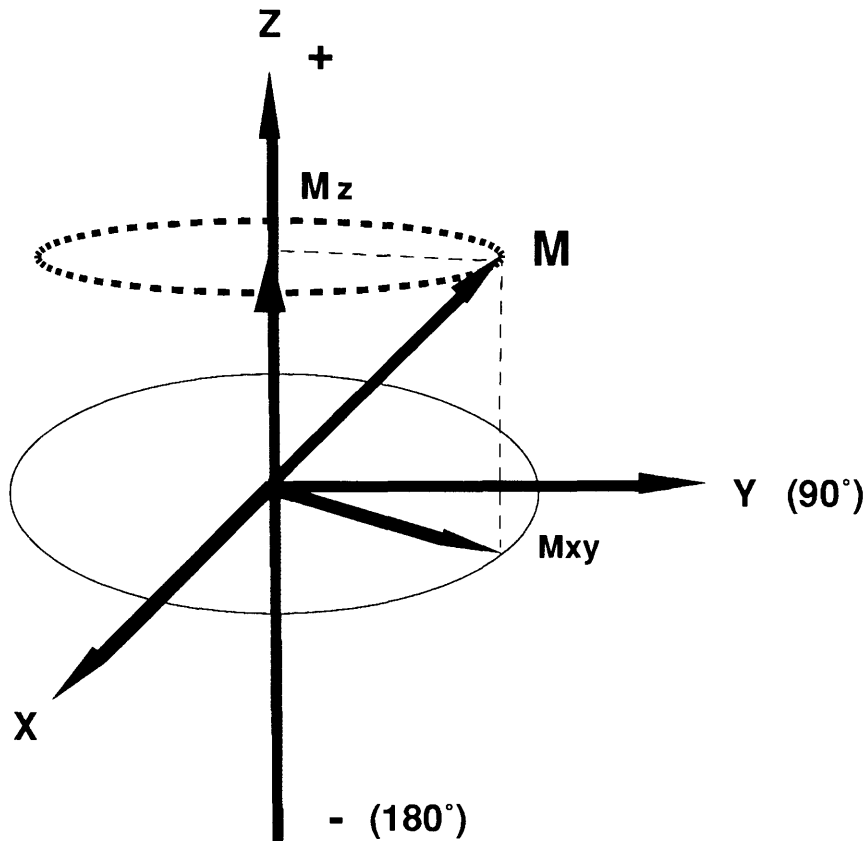


**Figure 1.4** Relaxation process of the vector sum of the magnetic moment of the spin system,  $M$ , after being tipped away from the direction of the main magnetic field ( $Z$ ), precesses about  $Z$  axis.  $M_z$  will relax back to  $M_0$  with a time constant characterized as  $T_1$  (Spin-lattice relaxation time) which can be calculated from:  $M_z(t) = M_z(0) [1 - e^{-\frac{t}{T_1}}]$ .  $M_{xy}$  on the other hand, will diminish to zero at the time constant  $T_2$  (spin-spin relaxation time) which can be calculated from:  $M_{xy}(t) = M_{xy}(0) \cdot e^{-\frac{t}{T_2}}$

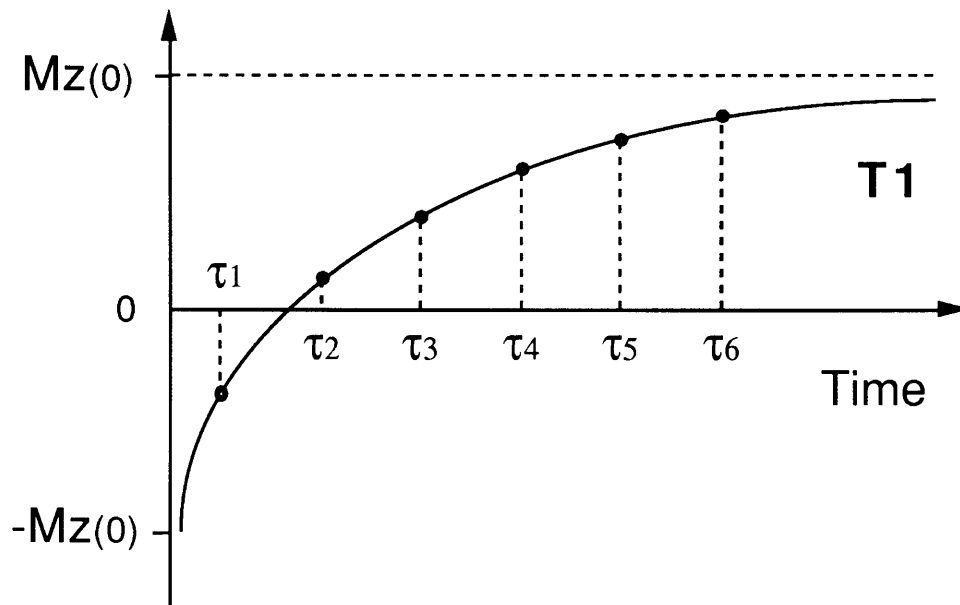


**Figure 1.5** Measurement of  $T_1$ . The inversion recovery pulse sequence is routinely used to measure  $T_1$  relaxation times. An inversion pulse ( $180^\circ$ ) is applied to convert  $M_z$  to  $-M_z$ , and the magnetization is allowed to recover. At the time  $\tau_i$ , a  $90^\circ$  pulse is employed to detect a electric signal, which can be converted to a magnetization. The recovery process is an exponential function expressed in  $T_1$  and  $\tau_i$  as:  $M_z(t) = M_z(0) [1 - 2e^{-\frac{t}{T_1}}]$

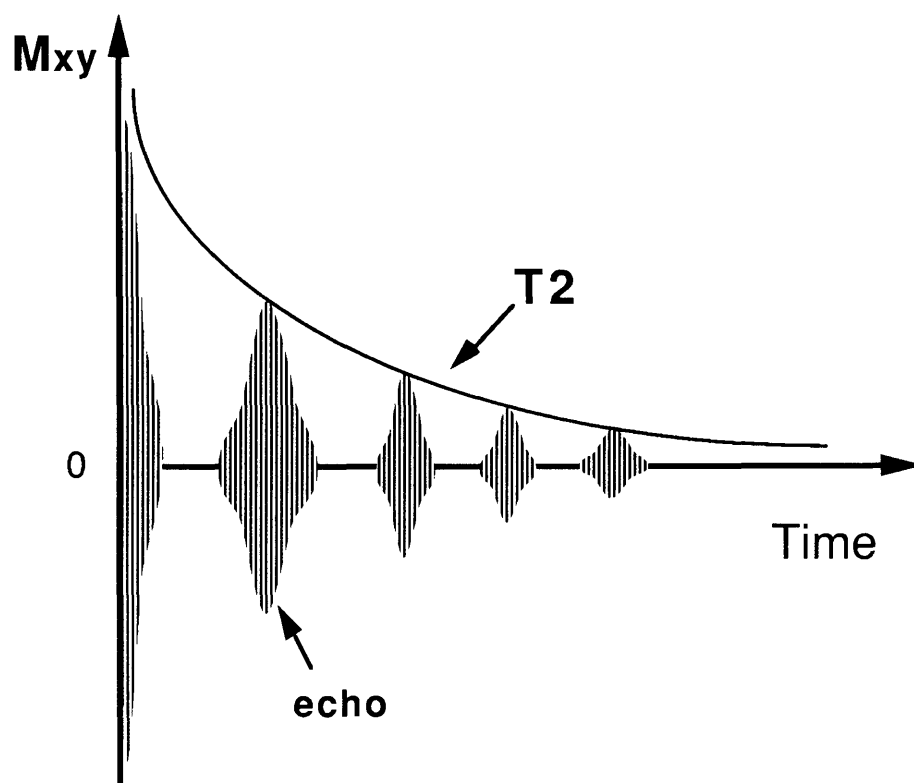


**Figure 1.6** Measurement of  $T_2$  (CPMG pulse sequence). The FID (Free Induction Decay) following the  $90^\circ$  RF pulse and the spin echo generated by a train of  $180^\circ$  refocusing pulses.

The peaks of the FID decay exponentially to zero with a time constant  $T_2$ :

$$M_{XY}(t) = M_{XY}(0) \cdot e^{-\frac{t}{T_2}}$$

## Image Contrast

The tissue contrast to noise ratio (CNR, equation 1.7) appearing on an MR image forms the basis for medical diagnosis. The CNR can be altered by the choice of specific pulse sequences and the associated timing parameters.

$$\text{CNR} = \frac{(SI_1 - SI_2)}{\text{noise}} \quad (1.7)$$

$SI_1$  and  $SI_2$  represent the signal intensities of two adjacent regions on an MR image. The magnitude of the detected signal depends upon the spin density (number of protons available),  $T_1$  and  $T_2$  characteristics of tissues, chemical shift, temperature, and flow phenomena. Among these parameters, the relaxation characteristics are most influential to the signal intensity. Therefore the tissue contrast of an MR image can be  $T_1$  or  $T_2$  weighted. In the spin-echo imaging sequence (the most common pulse sequence), for example, the type of image weighting can be manipulated by the repetition time ( $T_R$ ) and the echo time ( $T_E$ ). Figure 1.7 schematically illustrates the possibilities of generating different contrast from two types of tissues with different relaxation characteristics. A  $90^\circ$  excitation pulse is followed by a  $180^\circ$  refocusing pulse, generating an echo at  $T_E$ . The signal intensity of the image can be approximated by equation 1.8:

$$SI = M_z(\theta) \left[ 1 - e^{-\left(\frac{T_R}{T_1}\right)} \right] \cdot e^{-\left(\frac{T_E}{T_2}\right)} \quad (1.8)$$

where  $SI$  is signal intensity on an MR image,  $T_R$  is the repetition time, and  $T_E$  is the echo time in a pulse sequence.  $T_R$  determines the extent of  $T_1$  relaxation. The initial  $90^\circ$  excitation pulse completely tips the longitudinal magnetization into the transverse plane, and a time interval ( $T_R$ ) is allowed to elapse between excitations, during which time the spins undergo  $T_1$  relaxation. A long  $T_R$  ( $\gg 5 T_1$ ) allows enough time to for a complete  $T_1$

relaxation. Similarly,  $T_E$  determines the extent of  $T_2$  relaxation. The longer the time interval  $T_E$  the greater the extent of  $T_2$  relaxation. Spin-echo images acquired with short  $T_R$  ( $T_R \sim T_1$ ) and a short  $T_E$  ( $T_E < T_2$ ) are  $T_1$ -weighted. With shorter  $T_R$  values, tissues such as fat which have short  $T_1$  values appear bright, whereas tissues such as tumors and edema, that have longer  $T_1$  values, and therefore take more time to relax towards equilibrium, appear dark. The short  $T_E$  value diminishes the importance of tissue  $T_2$  differences. On the other hand, images acquired with long  $T_R$  and long  $T_E$  ( $T_E \sim T_2$ ) are  $T_2$ -weighted. Therefore, tissues with long  $T_2$ , such as tumors, edema, and cysts, appear bright, whereas tissues that have short  $T_2$ , such as muscle and liver, appear dark.

In summary, the MR image contrast is a function of several parameters including  $T_1$  and  $T_2$  relaxation times, proton density, chemical shift, temperature, magnetic susceptibility, and motion. Image contrast between tissues with different physicochemical properties is determined by the different image signal intensities each tissue produces in response to  $T_R$  and  $T_E$  in the case of a spin echo pulse sequence. This in return is determined by  $M_z(0)$ , directly corresponding to the proton density,  $T_1$  and  $T_2$  relaxation times.

The  $T_1$  and  $T_2$  relaxation times are therefore crucial parameters in MR imaging experiments. With conventional MR imaging techniques, however, the relaxation characteristics of the normal and pathological conditions are often very small. This makes the accurate diagnosis based on the contrast from the MR image difficult. For example, due to the lack of inherent difference between tumor and normal tissues, up to 20% of metastases of the liver can escape detection (Gilbert and Kagan 1976). Therefore it is important to increase the contrast between the normal tissue and pathological conditions on an MR image to improve the diagnostic accuracy. Since the variation of relaxation characteristics has a profound effect on the tissue contrast, the selective enhancement of tissue contrast can be achieved by the administration of magnetopharmaceuticals, i.e. MR

contrast agents, which change the local environment of protons and thereby change their relaxation characteristics.

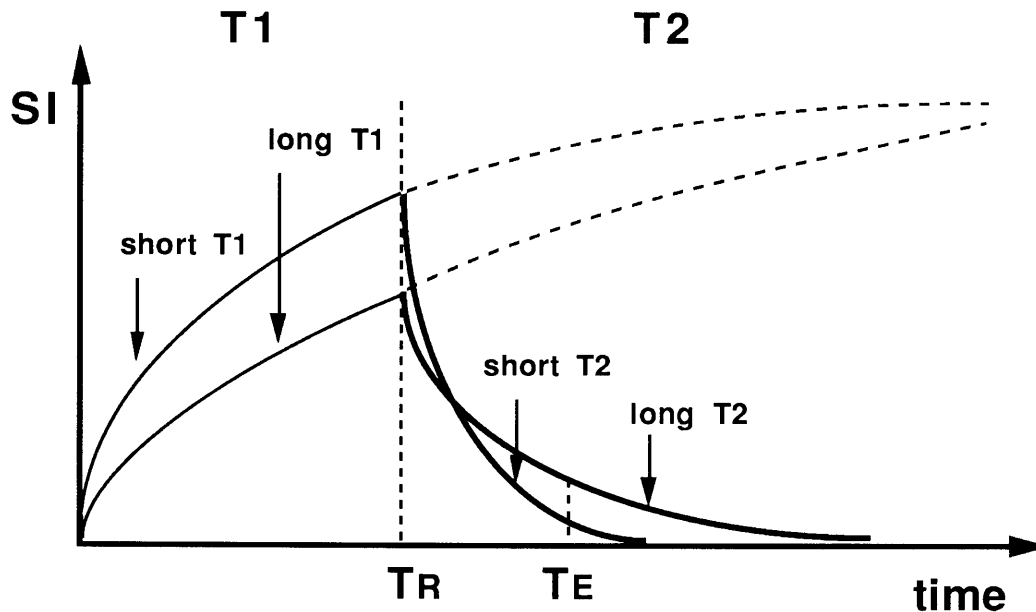


**Figure 1.7** Synthesis of Image contrast from a spin echo pulse sequence  
Schematic illustration of image contrast synthesis from two types of tissues with different relaxation characteristics. A  $90^\circ$  excitation pulse is followed by a  $180^\circ$  refocusing pulse, generating an echo at  $T_E$ .  $T_R$  determines the extent of  $T_1$  relaxation and  $T_E$  determines the extent of  $T_2$  relaxation.

Both  $T_1$  and  $T_2$  can determine the final signal intensity on an MR image. As seen from the diagram, manipulating  $T_R$  results in SI changes based on  $T_1$  characteristics while varying  $T_E$  brings changes in SI based on  $T_2$

characteristics.  $SI = M_z(0) \left[ 1 - e^{-\left(\frac{TR}{T_1}\right)} \right] \cdot e^{-\left(\frac{TE}{T_2}\right)}$



### 1.3 MR Contrast Agents

The purpose of magnetopharmaceuticals (MR contrast agents) is to selectively enhance the image contrast of the region of interest (normal or pathological tissues). This can be done by changing the magnetic environment of the protons, and thus the  $T_1$  and  $T_2$  relaxation times, providing measurable difference between normal and pathologic conditions *in vivo*. Differently from the conventional CT contrast agents (such as iodine-containing radiograph contrast agents), the MR contrast agents are not directly "seen" in the MR image. It is their indirect effects upon the relaxation mechanisms of surrounding protons which can be visualized as changes in signal intensity on the MR image (Brasch and Bennett 1988).

#### 1.3.1 Relaxivity

The efficiency by which MR agents enhance the proton relaxation rate is defined as relaxivity:

$$R_i = \frac{\Delta M}{\Delta T_i} \quad (1.9)$$

where  $T_i$  represents  $T_1$  or  $T_2$ ,  $M$  is concentration of the MR contrast agent, and  $R_i$  is  $T_1$  or  $T_2$  relaxivity. Relaxivities provide quantitative measurements of the effects of contrast agents on  $T_1$  and  $T_2$  relaxation times. In a typical relaxivity plot of a conventional contrast agent, inverse relaxation times are plotted against the concentration of contrast agents. The slopes of these curves represent the relaxivity and are expressed in  $(\text{mM}\cdot\text{sec})^{-1}$  or  $(\text{mmol/L}\cdot\text{sec})^{-1}$ .

### **1.3.2 Classification**

Based on the magnitude of their  $R_1$  and  $R_2$ , MR contrast agents can be classified as  $T_1$ - or  $T_2$ -dominant (Bydder, Felix et al. 1990). The agents that increase the  $1/T_2$  of proton to approximately the same extent as  $1/T_1$ , they are called  $T_1$  agents. The substances that increase  $1/T_2$  of proton to a much greater extent than  $1/T_1$ , are called  $T_2$  agents. Using most conventional pulse sequences,  $T_1$  agents (predominantly  $T_1$ -lowering agents) give rise to increases in MR signal intensity, therefore they are also called "positive" contrast agents. On the other hand,  $T_2$  agents largely increase  $1/T_2$  of tissue, hence lead to decreases in signal intensity and classified as "negative" contrast agents. Paramagnetic materials increase  $1/T_1$  and  $1/T_2$  approximately equally, whereas superparamagnetic agents predominantly increase  $1/T_2$ . Table 1.2 summarize the effect of these two types of agents on MR signal intensities for a given type of pulse sequence.

Paramagnetic agents include substances with one or more unpaired electrons, such as molecular nitric oxide, nitrogen dioxide, oxygen, or metal ions which have incompletely filled  $d$  or  $f$  orbitals (mostly transition metal ions). Most of the transition metal ions alone are extremely toxic to the human body, therefore chelation of the these ions with molecules such as diethylenetriamine-pentaacetic acid (DTPA) has been used to reduce their toxicity. Currently, the only MR contrast agent which has been approved by the United States Food and Drug Administration for clinical use is Gd-DTPA, representing the first generation of MR contrast agents introduced in the 1980s. This paramagnetic complex enhances predominantly the  $T_1$  relaxation rate of protons mainly through inner sphere relaxation (Lauffer 1987). Gd-DTPA has demonstrated useful enhancement of the MR image contrast of the central nervous system (Weinmann, Brasch et al. 1984; Hesselink, Healey et al. 1988; Unger, MacDougall et al. 1989). A typical dosage required for

effective contrast enhancement using this type of agents is approximately  $10^{-4}$  M. This concentration is lower than that of conventional iodinated radiographic contrast media for which  $10^{-2}$  M is an effective concentration, but higher than the effective concentration needed for radiopharmaceuticals ( $< 10^{-7}$  M).

The proton relaxation mechanism in a paramagnetic environment has been described in detail (Lauffer 1987). Briefly, there are three distinct types of interactions that contribute to the proton relaxation enhancement. First, when a water molecule binds in the primary coordination sphere of the metal ion and exchanges with the bulk solvent, the relaxation mechanism is called inner sphere relaxation. Second, when the water molecule passes the chelate due to translational diffusion, the relaxation mechanism is termed as outer sphere relaxation. Finally, the paramagnetic complex, with a large magnetic moment compared to protons, tumbles in solution at proper frequencies (characterized by a correlation time,  $\tau_c$ ) which stimulate nuclear relaxation, therefore enhances the  $T_1$  relaxation rate of the protons.

Research on superparamagnetic pharmaceuticals, representing a second class of MR contrast agents, started in 1986. These agents are particles with a much higher magnetic moment due to electron spin coupling in the crystal lattice, and they can significantly enhance the proton  $T_2$  relaxation rate (“ $T_2$ -agents”). Superparamagnetic agents include different types of inorganic iron particles which contain iron in different valency states and vary in their chemical composition, crystal structure, size and coating.

Superparamagnetic particulates, have a strong effect on the spin-spin (transverse) relaxation process of the nearby protons. The relaxation mechanism of these agents is a complex process which has been the topic of several papers, and remains an active area of research. Different from paramagnetic chelates, the superparamagnetic particulates has much higher magnetic moment and longer correlation time. The large magnetic moments of these

particulates in a magnetic field generate local field inhomogeneities. It is thought that as the protons diffuse through these field inhomogeneities, their Larmor frequencies lose coherence of phase, therefore, causing an increase in transverse relaxation rate of protons.

The high magnetic susceptibility, i.e. the ability to cause strong inhomogeneities in the magnetic field, is desirable for a MR contrast agent because it can significantly reduce the dosage required for sufficient contrast enhancement, thereby reducing its toxicity.

Table 1.3 summarizes currently available MR contrast agents and their potential applications (Brasch 1992).

**Table 1.2 Classification of MR Contrast Agents**

	Paramagnetic	Superparamagnetic
Effect on T <sub>1</sub>	↑↑	↑
Effect on T <sub>2</sub>	↑	↑↑
Effect on signal intensity	↑↑	↓↓
MR pulse sequence	T <sub>1</sub> weighted sequences	T <sub>2</sub> weighted sequences
Examples	Gd-DTPA	iron oxides

DTPA= Diethylenetriaminepentaacetic acid

Table 1.3 Currently available MR Imaging contrast agents

Contrast Agent Type			
Enhancement type	Extracellular	Intracellular or Cell -Bound	Gastrointestinal
Positive enhancing	Small Molecular weight Gadopentate dimeglumine Gadolinium DOTA meglumine Gadodiamide injection Nitroxides Macromolecular/blood pool Albumin-(Gd-DTPA) <sub>x</sub> Dextran- (Gd-DTPA) <sub>x</sub> Polylysine-(Gd-DTPA) <sub>x</sub> Paramagnetic liposomes	Hepatocyte-directed Gd-BOPTA Gd-EOB-DTPA Manganese DPDP Iron HBED Fe-EHPG RES-directed Paramagnetic liposomes Tumor-directed Metalloporphyrins Antibody-(Gd-DTPA) <sub>x</sub> Calcification-directed Gd-DTPA diphosphate	Water-miscible Gadopentate dimeglumine Ferric ammonium citrate Water-immiscible Vegetable oils Fats Sucrose polyester
Negative enhancing	Small Molecular weight Dysprosium DTPA Dy-DTPA-BMA Macromolecular/blood pool USPIO Albumin-(Dy-DTPA) <sub>x</sub>	Hepatocyte-directed Arabinogalactan USPIO RES-directed SPIO USPIO MION Superparamagnetic liposomes Lymph nodes SPIO USPIO MION Antigen-directed MION-immunoglobulin	Water-miscible SPIO Barium sulfate suspensions Clays Water-immiscible Gas-producing pellets Perfluoroocylbromide

BMA= bis-methylamide, BOPTA= benzyloxypropionictetraacetate, DOTA= tetraazacyclododecanetetraacetic acid, DPDP= dipyrldoxal diphosphate, DTPA= diethylenetriaminopentaacetic acid, EHPG= diastereomeric N, N' -ethylene-bis (2-hydroxyphenylglycine), EPB= ethoxybenzyl, HBED= N-N'-bis (2-hydroxybenzyl)ethylenediamine-N, N' -diacetic acid, MION= monocrytalline iron oxide nanopolymer, RES= reticuloendothelial system, SPIO= superparamagnetic iron oxide, USPIO= ultrasasmal superparamagnetic iron oxide.

## 1.4 Research Objectives

There is a need for the development of magnetopharmaceuticals for receptor, metabolic and functional MR imaging which requires a magnetic label which can leave the vascular space, which has a high magnetic susceptibility to enhance contrast at low tissue concentrations and the ability to be attached readily to carrier molecules for site-specific target delivery. Superparamagnetic contrast agents have a significantly higher magnetization and a much lower dosage requirement *in vivo*. Unfortunately, currently available iron oxides are not suited for targeting because their large size (0.2-1 $\mu$ m) results in rapid extraction by phagocytic cells in liver and spleen.

The overall goal of this thesis project was to synthesize, characterize and evaluate biocompatible superparamagnetic compounds that can be used *in vivo*. To assure the effectiveness of the label for various applications, there are several prerequisites: the superparamagnetic label had to be biocompatible, non-toxic, with long blood half-life and be able to escape the rapid recognition of the reticuloendothelial system. In addition, the label should be attachable to variety of carrier molecules and be detectable at low concentrations *in vivo*. In order to meet these targets, the following research objectives were developed:

1. Synthesize a variety of stable superparamagnetic label to determine the optimal magnetic properties ( Chapter 3);
2. Characterize the physical and chemical properties of these agents with respect to core structure and size, magnetic properties, chemical composition, stability, hydrodynamic parameters, and relaxation enhancement to protons in aqueous environment (Chapter 4);
3. Determine the *in vitro* cellular interactions and pharmacological behaviors of these agents in animal models (Chapter 5);
4. Determine the efficacy of the *in vivo* contrast enhancement and targetability to the liver of both unlabeled and labeled agents by MR imaging (Chapter 6).

## Chapter II

# Background

The basic principles of MR imaging, the importance of MR contrast agents and their classifications have been discussed in the previous chapter. The intent of this chapter is to use the basic physics of magnetism to identify parameters of evaluating magnetic materials. These parameters will later be used as criteria for selecting MR contrast agents. Previous methods of synthesis of iron oxide in industry will be summarized.

### 2.1 Magnetic Materials

The history of the development of magnetic materials is long. According to Chinese history, a legendary ruler of an ancient kingdom made use of the compass to direct his victorious battles against barbarian tribesmen before 2600 BC (1982). There is evidence that lodestone was discovered in Asia Minor as a natural magnet in Magnesia more than 3500 years ago.

Romans called the stone, which had the power to attract iron and other pieces of ore, and also to induce a similar power of attraction in iron, "magnes lapis", which means Magnesian stone, from which the words "Magnet" and "Magnetism" were derived. In the 12<sup>th</sup> century, William Gilbert in *De Magnete* established that the earth is a large magnet, and raised magnetism to a field of exact experimental science (Hawkins and Allen 1991).

### 2.1.1 Structures and Properties

All substances, whether solid, liquid or gas, display certain magnetic characteristics at all temperatures: magnetism is one of the basic properties of materials. In order to characterize the magnetic properties of materials more precisely, several parameters are used, defined in the following:

When a material is placed in a magnetic field,  $\mathbf{B}$ , it acquires a dipole moment. The magnitude of this dipole moment, depends upon the nature of the material, the applied magnetic field strength, and is proportional to its volume. Therefore, we define the dipole moment per unit volume induced in the material as *magnetization*,  $\mathbf{M}$ . The relation of  $\mathbf{M}$  to the applied magnetic field can be expressed as:

$$\mathbf{M} = \chi \mathbf{B} \quad (2.1)$$

where  $\chi$  is defined as the *magnetic susceptibility*, the most important magnetic material property.  $\chi$  depends on the temperature according to:

$$\chi = \frac{C}{T + \theta} \quad (2.2)$$

where  $C$  and  $\theta$  are both characteristic constants of each material. As the applied field strength is increased for any particular material, the magnetization reaches a constant value, defined as saturation magnetization,  $M_S$ , which is consequently also a material property.

The magnetic properties of an ion or atom are determined by the orientation and number of its electron spins. For metal oxides (transition metal oxides in particular), the individual electron spins are so strongly correlated in their motion that spin of an ion is better characterized by one total spin (atomic spin) than the individual electron spins. The atomic spins of neighboring ions may also be strongly correlated with each other to form a spin



sub-lattice. Depending on the magnitude, the orientation and the number of spin sublattices, the material possesses a characteristic internal magnetic field, as well as characteristic responses to an applied magnetic field. Regarding the various kinds of responses of materials to a magnetic field, we observe five basic categories:

1) ferromagnetic, 2) antiferromagnetic, 3) ferrimagnetic, 4) paramagnetic and 5) diamagnetic. The five main classes of magnetic materials and the criteria by which they are distinguished from each other are summarized in Table 2.1.

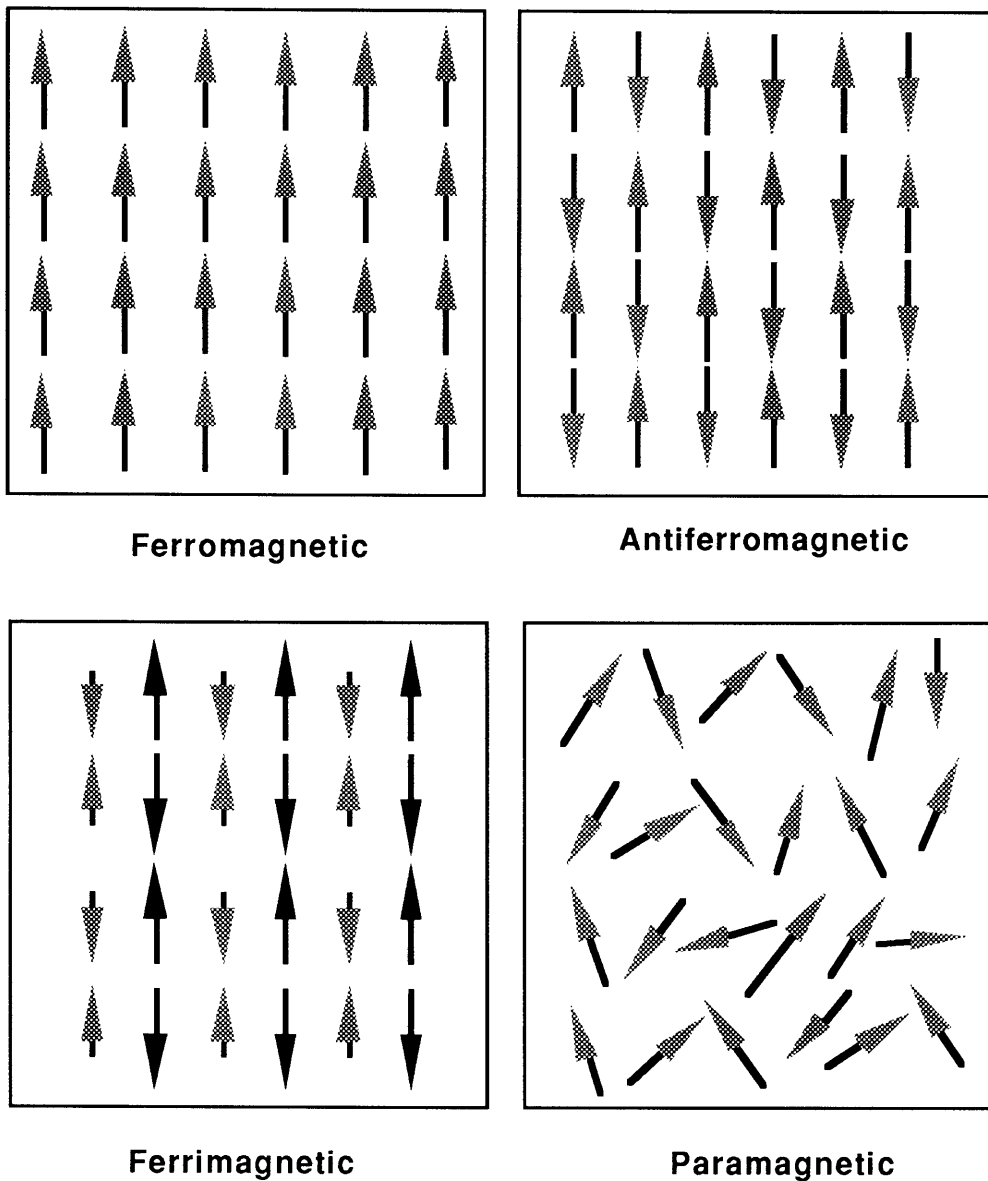
The atomic spin arrangements of various types of magnetic materials are schematically represented in figure 2.1. In ferromagnetic materials, the atoms with permanent dipole moments interact with each other to produce a parallel alignment in the crystal lattice. This generates a large magnetic susceptibility, and therefore strong response to the applied magnetic field. On the contrary, in antiferromagnetic materials, the dipole moments interact with each other to produce an anti-parallel alignment in the crystal lattice, resulting in a complete cancellation of the magnetic moment of the individual dipoles. Therefore there is no response to a magnetic field from antiferromagnetic materials. Similar to the antiferromagnetic alignment, ferrimagnetic materials have an anti-parallel atomic dipole coupling in the crystal lattice. However, the magnitudes of the oppositely aligned dipole moments are not equal, resulting a net magnetic moment when placed in a magnetic field. Ferrimagnetic materials therefore have a smaller magnetic susceptibility than ferromagnetic materials. In the case of paramagnetic materials, the dipoles in the crystal lattice are randomly oriented and do not interact with each other. When placed in a magnetic field, the magnetic moment of the material increase slowly in a linear fashion until saturation magnetization is reached.

Table 2.1 Classification of materials according to magnetic properties

Class	Ferromagnetic	Ferrimagnetic	Paramagnetic	Diamagnetic	Anti-ferromagnetic
Critical temperature	Curie temperature $T_c$	Curie temperature $T_c$	None	None	Néel temperature, $T_N$
Magnitude of $\chi$	Large (below $T_c$ )	Large (below $T_c$ )	$+10^{-5}$ to $+10^{-3}$	$-10^{-6}$ to $-10^{-5}$	$+10^{-5}$ to $+10^{-3}$
Temperature variation of $\chi$	$\chi = C/(T - t)$				
Spontaneous magnetization			None	None	None
Structure on atomic scale	Atoms have permanent dipole moments, interaction produces $\uparrow\uparrow$ alignment	Atoms have permanent dipole moments, interaction produces $\uparrow\downarrow$ alignment, but moments are unequal	Atoms have permanent dipole moments, No interactions between neighbouring moments	Atoms have no dipole moments	Atoms have permanent dipole moments, interaction produces $\uparrow\downarrow$ alignment
Examples:	Transition metals Fe, Co, Ni.	Magnetite, $\gamma$ -Fe <sub>2</sub> O <sub>3</sub> , Ferrites	O <sub>2</sub> , NO, Cr, Mn, ion of transition metals, e.g. Gd	Noble gases, Cu, Hg, Bi, H <sub>2</sub> , N <sub>2</sub> , most organic compounds	MnO, CoO, NiO, Cr <sub>2</sub> O <sub>3</sub> , CuCl <sub>2</sub> , MnS, etc.

Curie temperature: a critical temperature for only ferromagnetic and ferrimagnetic materials

Néel temperature: critical temperature for antiferromagnetic materials.



**Figure 2.1** Schematics of spin arrangements in various magnetic materials: In ferromagnetic materials, the atomic dipoles have a parallel alignment in the crystal lattice. In antiferromagnetic materials, dipole moments have an anti-parallel alignment, resulting a complete cancellation of the magnetic moment of the individual dipoles. Ferrimagnetic materials also have an anti-parallel atomic dipole coupling in the crystal lattice. However, the magnitudes of the oppositely aligned dipole moments are not equal. In the case of paramagnetic materials, the dipoles in the crystal lattice are randomly oriented and do not interact with each other.

### **Superparamagnetism:**

In addition to the five main categories of magnetic materials we have discussed previously, there is a special magnetic phenomenon which shares both properties of paramagnetic and ferromagnetic materials. It is of particular importance to describe such phenomenon because iron oxide particles, which were discussed in the previous chapter, may exhibit superparamagnetic behavior:

Frenkel and Dorfman first predicted in 1930 that a particle of ferrimagnetic (or ferromagnetic) material could consist of a single magnetic domain below a critical size. It has been defined that a single domain particles will have a uniform magnetization at any field strength. In 1949, Néel pointed out that if a single domain particle were small enough, the thermal fluctuation could cause direction of its magnetization similar to that of Brownian rotation.

Bean and Livingston, in 1959, observed that the magnetization behavior of single domain particles (isotropic) in thermodynamic equilibrium at all fields is identical with that of atomic paramagnetism but that they have an extremely large moment (Bean and Livingston 1959). This large magnetic moment does not result from the individual atoms, rather, it comes from thousands (depending upon the particle size) of atoms in the particle which are ferromagnetically coupled by exchange forces. When a magnetic field is applied to a suspension of small ferromagnetic particles, they are partially aligned by the field and partially disordered by the thermal motion, thereby exhibiting an over-all paramagnetism. These particles can be treated as macromolecules and a particle size can be also calculated from their response to a magnetic field. This thermal equilibrium behavior was called *superparamagnetism*, defined by the following two criteria:

- 1). The magnetization curve must show no hysteresis because that is not a thermal equilibrium property;
- 2). The magnetization curve for an isotropic sample must be temperature dependent to the extent that curves taken under different temperature conditions would superimpose when plotted against  $B/T$  after correction for the temperature dependence of the spontaneous magnetization.

### ***2.1.2 Ferrites***

Ferrites are complex magnetic oxides that contains the ferric oxide ( $\text{Fe}_2\text{O}_3$ ) as their basic magnetic component. The focus of the following discussion will be on this type of materials. Ferrites are important soft magnetic materials, and have been used in practical applications for more than half a century. The work of Hilpert in 1909 is generally accepted to be the first systematic study on the relationship between chemical and magnetic properties of the various binary iron oxides having the general composition:  $\text{MFe}_2\text{O}_3$ , where M represents a divalent metal. Six years later, the crystal structure of mineral magnetite was analyzed by Bragg and Nishikawa independently. Bragg discovered that other mineral spinels, such as  $\text{MgAl}_2\text{O}_4$  has the same crystal structure as magnetite. Thereafter, active research extended the knowledge of ferrites to more quantitative information on their curie temperatures and saturation magnetizations. The ferrites since then have been used as material for the cores in inductors and transformers. Then the discovery that polycrystalline ferrites have a rectangular hysteresis loop made it possible to use ferrites as memory elements, composing some of the most important parts modern microwave transmission and electronic computers.

It was not until 1948, however, that Verwey and Heilmann provided the simple relationship of the saturation magnetization of ferrites and their ion distribution over the tetrahedral and octahedral sites of the spinel lattice (Verwey and Heilmann 1947). Subsequently, Néel introduced the concept of partially compensated antiferromagnetism which is later defined as ferrimagnetism. Gorter and Schulkes proved this theory experimentally by the magnetization versus temperature curve. Neutron diffraction experiments by Shull, Wollan and Keohler on ferrite single crystals verified the ferrimagnetic ordering of the spins in  $\text{Fe}_3\text{O}_4$ .

The crystallography of ferrites falls in a natural manner into three types: 1) the cubic ferrites of the spinel type, 2) the cubic ferrites of the garnet type, and 3) the hexagonal ferrites. The following discussion will focus on the ferrites of spinel structure since it is the most relevant to this thesis research. The cubic ferrites are also called ferros spinels because they crystallize in the same crystal structure as the mineral spinel and they derive their general formula  $\text{MFe}_2\text{O}_4$  from that ( $\text{MgAl}_2\text{O}_4$ ) of spinel. In this formula, M represents a divalent ion of metal. Besides the divalency, the ionic radius of the metal should fall between 0.6-1.0 Å. Mg, Fe, Co, Ni, Cu, Zn and Cd all satisfy these two conditions and therefore form various single cubic ferrites. Magnetite which contains one ferrous ion and two ferric ions in each formula unit is a typical ferrite. The crystal structure of ferrites is based on a face-centered cubic lattice of the oxygen ion. Each unit cell contains eight formula units. Therefore there are 32  $\text{O}^{2-}$  anions, 16  $\text{Fe}^{3+}$  cations and 8  $\text{M}^{2+}$  cations in the unit cell, and the lattice constant is rather large, of the order of 8.5 Å. In each unit cell, there are 64 tetrahedral [A] sites and 32 octahedral [B] sites. These sites are so named because they are surrounded by four or six oxygen ions at equal distance respectively. In the mineral spinel the 16 trivalent cations occupy one-half of the [B] sites, and the eight divalent cations occupy one-eighth of the [A] sites. However, most ferrites

crystallize in an inverse spinel structure, in which the eight divalent cations occupy [A] and [B] sites. Table 2.2 summarizes the magnetic properties of different spinels.

Extensive research on the physical properties, especially the magnetic properties, of ferrites was carried out because of their importance as electronic materials (Smit and Wijn 1959). The following graph (Figure 2.2) shows the saturation magnetization ( $M_z$ ) versus temperature of several different ferrites. Among the ferrites shown in the figure, magnetite ( $\text{Fe}_3\text{O}_4$ ) has the highest saturation magnetization at body temperatures, and is therefore most suitable for use as an MR contrast agent.

**Table 2.2 Properties of Ferrites**

	MW	Density	$a_0$ (Å)	$\mu_m$ (cal)	$\mu_m$	$M_0$ (0 K)	$M_s$	$T_c$ (C)
$\text{ZnFe}_2\text{O}_4$	241.1	5.33	8.44	Antiferromagnetic	$T_N = 5\text{K}$	$M = 5\mu_B$	-	
$\text{MnFe}_2\text{O}_4$	230.6	5.00	8.51	5	4.55	560	400	-
$\text{FeFe}_2\text{O}_4$	231.6	5.24	8.39	4	4.1	510	480	585
$\text{CoFe}_2\text{O}_4$	234.6	5.29	8.38	3	3.94	496	425	520
$\text{NiFe}_2\text{O}_4$	234.4	5.38	8.337	2	2.3	300	270	585
$\text{CuFe}_2\text{O}_4$	239.2	5.35	8.7	1	1.3	160	135	-
$\text{MgFe}_2\text{O}_4$	200.0	4.52	8.36	0	1.1	140	110	440
$\text{Li}_{1.5}\text{Fe}_{2.5}\text{O}_4$	207.1	4.75	8.33	2.5	2.6	330	310	670
$\gamma\text{-Fe}_2\text{O}_3$	159.7	-	8.34	2.5	2.3	-	417	575
$\text{Mn}_3\text{O}_4$	228.8	4.84	5.75	-	1.85	218	185	42

$M_s$  = Saturation magnetization per gram, emu/g.

$T_c$  = Curie temperature

$a_0$  = Lattice parameters

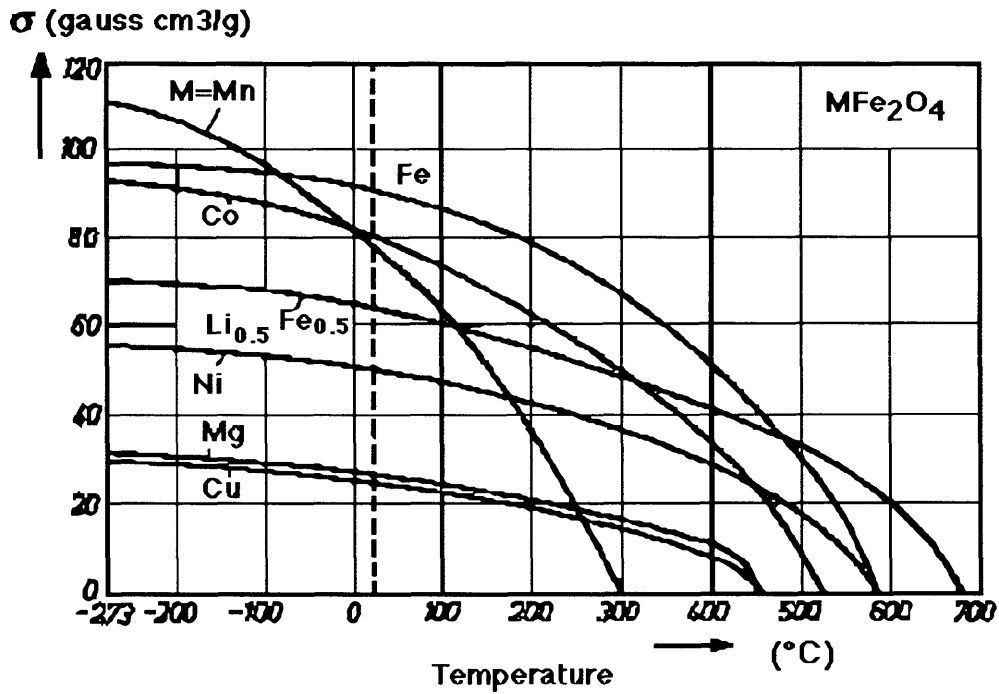


**Figure 2.2** Saturation magnetization of ferrites versus temperature

Crystalline magnetite was selected as core of the MR contrast agent because of its preferred magnetic properties. Magnetite belongs to the cubic ferrites which have the general formula  $MFe_2O_4$ , and a spinel crystal structure.  $Fe_3O_4$  is the ferrite which has the highest saturation magnetization at body temperature, and at low field strength (1.5T) among all ferrites



## 2.2 Magnetic Iron Oxides

Magnetite is the metal ferrite with the highest magnetization at room temperature, and it is therefore the most appropriate material for MR contrast agents. However, in the synthesis of iron oxides, various types iron oxides can be formed, depending upon the conditions. Although they all have similar physical appearances, their magnetic properties differ dramatically.

### 2.2.1 Physical Properties of Iron Oxides

Various physical, chemical and magnetic properties of iron oxides are summarized in table 2.3.

**Table 2.3 Physical properties of iron oxides**

Name:	$\alpha$ -Fe <sub>2</sub> O <sub>3</sub>	$\gamma$ -Fe <sub>2</sub> O <sub>3</sub>	Fe <sub>3</sub> O <sub>4</sub>
Structure:	<i>b.c.c.</i>	inverse spinel	inverse spinel
Physical appearance:	brown	brown	Black
$\mu_B$ /f.u.	0	4	5
$M_S$ (20°C)	-	$4.0 \times 10^{+2}$ G	$4.8 \times 10^{+2}$ G
magnetic category:	antiferromagnetic	ferrimagnetic	ferrimagnetic

*b.c.c.* = body centered cubic

$\mu_B$  = magneton

f.u. = formula unit

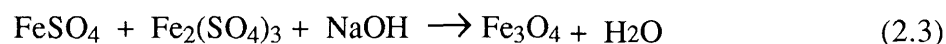
$M_S$  = Saturation magnetization (Gauss)

The material of choice for MR contrast agents among various possible metal oxides are magnetite (Fe<sub>3</sub>O<sub>4</sub>) or maghemite ( $\gamma$ -Fe<sub>2</sub>O<sub>3</sub>) because of their stability in aqueous solution and their high saturation magnetization at low field at body temperature. To understand mechanisms of formation and transformation of these iron oxides in aqueous solution is of

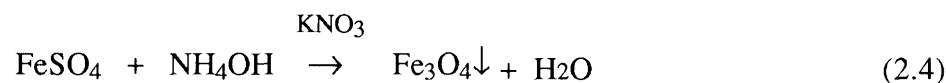
great importance for development of superparamagnetic contrast agents for magnetic resonance imaging. In the following discussion, reaction mechanisms which determine the formation of various iron oxides from aqueous solutions will be addressed in detail.

### 2.2.2 Reaction Mechanisms

Attempts to synthesize magnetic iron oxide from aqueous solutions were reported as early as in 1859 by Lefort (Lefort 1852; Lefort 1852). He reported the formation of black magnetic precipitates (magnetite) in solutions by reacting ferric sulfate and ferrous sulfate with boiling a NaOH solution (Equation 2.3). The black mixture formed was then boiled for an hour, and the precipitate did not settle readily.



In 1900, Haber synthesized the same magnetite by reacting a solution of ammonia with a solution of crystalline ferrous sulfate at boiling temperature in the presence of  $\text{KNO}_3$  (Equation 2.4). This method yielded larger magnetic particles which settled rapidly in solution.



Baudisch and Welo in 1920 reported another method which produced magnetite as a by-product when reducing  $\text{KNO}_3$  with freshly precipitated ferrous hydroxide in the presence of oxygen. The mixture was first greenish, then turned black with magnetic precipitates forming rapidly and settling in the solution.

From the syntheses described above, two methods of  $\text{Fe}_3\text{O}_4$  synthesis can be distinguished: Lefort's method formed magnetite from solution containing both ferrous and ferric ions and in a ratio of 1:2 which is necessary to form  $\text{Fe}_3\text{O}_4$ , and no oxidation is necessary during and after the precipitation. Haber's and Baudisch and Welo methods both involved precipitation of magnetite in hydroxide solution containing only ferrous ions. These two methods require oxidation of two thirds of ferrous ion to ferric ion during and after precipitation. Experimental results showed that there was no structural difference between the magnetites formed from the three methods, the only difference was the average size of the crystal.

As the application of magnetite in industry increased, large scale production of such materials became the focus of research in 1940s. More traditional process of magnetite production used gas-solid reactions at high firing temperature (1000-2000° C). This process mainly produces coarse scale, large quantities of magnetite, with relatively low purity.

The discovery of possibilities of using magnetic materials, ferrites in particular, for electronic computers pushed the research of synthesizing high quality magnetic materials to chemical precipitation. A wealth of literature is available on the synthesis of ferrite fine particles for recording media, and the detailed mechanism of formation of iron oxides was established by Misawa in 1977 (Misawa, Hashimoto et al. 1973; Misawa, Hashimoto et al. 1973; Misawa, Hashimoto et al. 1974).

It was not until 1938, that Elmore first successfully prepared a colloidal suspension of magnetite in water (Elmore 1938; Elmore 1938). The objective of such effort was to synthesize a so called "magnetic liquid" to observe the domain structure of magnetic materials. Elmore used Lefort's method to first precipitate small particles of magnetite,

then re-suspended the precipitate in soap solution to form stable colloids of magnetite fine particles.

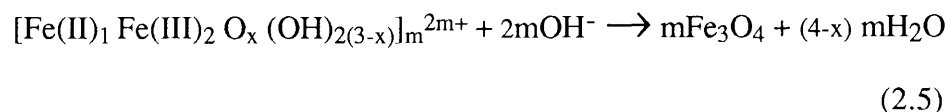
The development of colloidal suspensions of magnetite as ferrofluids was first reported in 1965, and most of the developmental work was accomplished in the late 1960s by Kaiser and Rosensweig. In their studies, various dispersed magnetite ferrofluids were prepared and their properties were evaluated. Kaiser concluded that the particle size in the final suspension depended upon the nature of the surfactant used. The stability of the final ferrofluid depended upon both the interaction between the polar heads of the surfactant and the surface of magnetite particles, and the interaction between the balance structure of the surfactant and the solvent systems. Solvent systems such as aliphatic hydrocarbons (kerosene), fluorocarbons, water, ethylene glycol, glycerol and esters were studied in detail. There were significant effects on the magnetic properties of such fluids in various solvent systems, and the length of the surfactant molecules played an important role as well.

In the 1970s, magnetic microspheres of iron oxides were introduced to biological science as a useful magnetic “labeling” for selective cell separation. In 1984, magnetite microcrystals were first discovered in bacteria. This brought the study of magnetic iron oxides in living systems to the attention of the scientific community.

The reaction mechanisms of iron in aqueous environments are determined by thermodynamic relationships, the oxidation rate of Fe(II) as well as by the structure and composition of initial and intermediate iron species. The existence of electrostatic and steric effects of anions such as  $\text{Cl}^-$ ,  $\text{SO}_4^{2-}$ ,  $\text{NO}_3^-$ ,  $\text{CO}_3^{2-}$  have influence on the configurations of intermediate complex cations and oxygen stacking, and therefore eventually affect the crystal structure and magnetic properties of the end-product.

Oxidation and deprotonation are two general pathways that many iron species in aqueous solution will go through. There are three intermediate complex structures in solution which are crucial in determining possible iron oxides formation and transformation. All three complexes are Fe(II) and Fe(III) ions held together by ol- and oxo-bridges which can be formed with the assistance of OH<sup>-</sup> groups in solution. The first two complexes which are green during synthesis can be represented as [Fe(II)<sub>2</sub> Fe(III)<sub>1</sub> O<sub>x</sub> (OH)<sub>y</sub>]<sup>(7-2x-y)+</sup> and [Fe(II)<sub>1</sub> Fe(III)<sub>1</sub> O<sub>x</sub> (OH)<sub>y</sub>]<sup>(5-2x-y)+</sup> respectively. In the formation of green complexes, the electrostatic and steric effects of coexisting anions such as Cl<sup>-</sup>, SO<sub>4</sub><sup>2-</sup>, which have stronger affinities to the iron species than ClO<sub>4</sub><sup>-</sup>, may influence the configuration of these complex cations and the oxygen stacking in the final crystals. Upon slow addition of OH<sup>-</sup>, magnetite can be formed from these green complexes. If violent oxidation takes place, iron oxyhydroxides are the final products.

When a mixture of Fe(II)<sub>1</sub>-Fe(III)<sub>2</sub> solution (pH ≈ 1.0) is neutralized, a dark red intermediate complex (the third one) is formed. Magnetite can be formed in aqueous solution by precipitation reaction and dehydration of dark red complex cation [Fe(II)<sub>1</sub> Fe(III)<sub>2</sub> O<sub>x</sub> (OH)<sub>2(3-x)</sub>]<sub>m</sub><sup>2m+</sup> as shown in the following reaction:



Upon further addition of OH<sup>-</sup> to the solution of dark red complex, a pH plateau appears at about 7.2 and fine black particles rapidly precipitate. The dark red complex has a configuration similar to that of Fe<sub>3</sub>O<sub>4</sub> since it is easily converted to Fe<sub>3</sub>O<sub>4</sub> in aqueous solution .

There are possibilities for other iron products to be formed during the synthesis of magnetite in aqueous solution depending on the specific reaction conditions. Possible

products include  $\gamma$ - and  $\alpha$ - iron oxides and  $\alpha$ -,  $\beta$ -,  $\gamma$ -, and  $\delta$ - iron oxyhydroxides (FeOOH). Because, for our purpose, we would like to eliminate any possible formation of iron products other than magnetite, the following considerations are important:

When Fe(III) exists in solution in excess amount, the reaction to form  $\alpha$ -Fe<sub>2</sub>O<sub>3</sub> becomes favorable. As noted previously,  $\alpha$ -Fe<sub>2</sub>O<sub>3</sub> is a diamagnetic material which does not fit in the requirement for MR contrast agents. It is not yet very clear what controls the formation of  $\gamma$ -Fe<sub>2</sub>O<sub>3</sub> in aqueous solution. It has been reported that the existence of NO<sub>3</sub> is an important factor for the formation of  $\gamma$ -Fe<sub>2</sub>O<sub>3</sub>.

Baudisch and Welo discovered that magnetite powder can be further oxidized upon heating (220 °C)  $\gamma$ -Fe<sub>2</sub>O<sub>3</sub>.  $\gamma$ -Fe<sub>2</sub>O<sub>3</sub> (also represented as (Fe)(Fe<sub>5/3</sub>~<sub>1/3</sub>)O<sub>4</sub> where ~ indicates a vacancy in the crystal lattice) has similar crystal structures as magnetite, yet only contain ferric ion in the crystal lattice.  $\gamma$ -Fe<sub>2</sub>O<sub>3</sub> is relatively stable in air, and has a smaller density as compared to magnetite. When  $\gamma$ -Fe<sub>2</sub>O<sub>3</sub> was further heated to 550 °C, a non-magnetic iron oxide  $\alpha$ -Fe<sub>2</sub>O<sub>3</sub> was formed.  $\alpha$ -Fe<sub>2</sub>O<sub>3</sub> has a different crystal structure than magnetite, with ferric ion completely coupled to each other in the crystal lattice which gives a zero net magnetic moment.

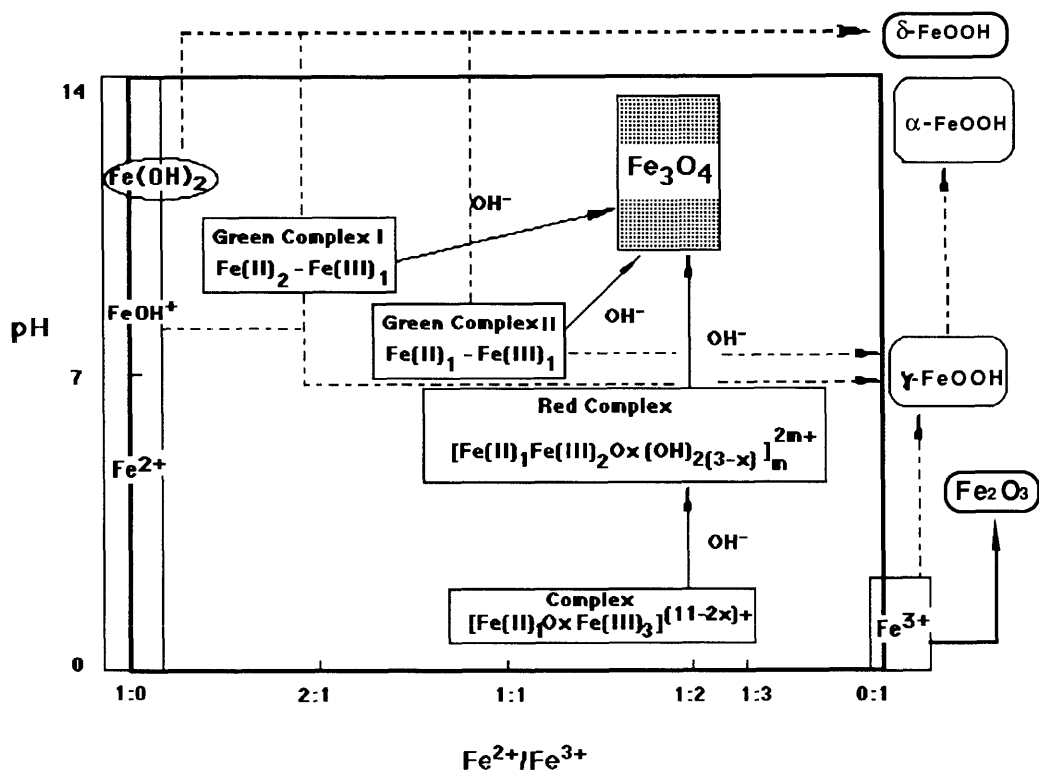


Figure 2.3 Reaction mechanism in aqueous solution

The x-axis indicates various initial  $\text{Fe}^{2+}/\text{Fe}^{3+}$  ratios, and the y-axis represent the pH conditions during the synthesis. Possible intermediate complexes and final composition of the products are shown in the corresponding positions on the diagram. The shaded box indicates the formation of magnetite from the solution, and other possible products such as different types of iron oxyhydroxides are also shown. The solid lines are slow oxidation pathways, and dashed lines represent rapid oxidation conditions.

Thus far, most of the effort has been focused on the synthesis of magnetic particles in the micrometer size range for the practical reasons mentioned previously. It is a challenging problem, however, to synthesize smaller (nm size) stable particulates from the known methods to fulfill the requirement of MR contrast agents. From the available literature, it can be concluded that parameters such as reaction temperature, initial concentrations of ferric and ferrous ions and oxidation rates have significant effect on the magnetic properties and physical size of the final product. It is also unknown how the use of various polymeric stabilizing agents effects the formation of magnetite. These aspects of synthesis will be investigated in chapter 3.



## **Chapter III**

# **Synthesis**

Although the reaction mechanisms of iron oxides have been investigated previously, the research efforts were mainly focused on their industrial applications as semiconductor materials and commercial permanent magnets. For the development of MR contrast agents, it is therefore necessary to examine in detail the synthesis of nanometer size magnetic iron oxide particle (referred to as monocrystalline iron oxide nanocompound, MION) in the presence of polymers. This chapter will present results from series of experiments which were used to optimize the MION synthesis. In addition, experiments were carried out to evaluate: 1) crystal structure of the core, 2) crystalline size distribution, 3) colloidal solution stability, 4) conjugation to carrier molecules.

### **3.0 An ideal Biocompatible Iron Oxide**

To further improve the sensitivity and specificity of MR imaging, the development of magnetopharmaceuticals for receptor, metabolic and functional diagnosis is desirable. This requires a magnetic label with a high magnetic susceptibility and small size to be detectable at low tissue concentrations, to be able to leave the vascular space, and to be readily attachable to carrier molecules for site specific target delivery. A model of such a compound is depicted in figure 3.1. It consists of a superparamagnetic core of several nanometers, surrounded by anchored surface polymers, which can subsequently be attached to a variety of target-specific carrier molecules.

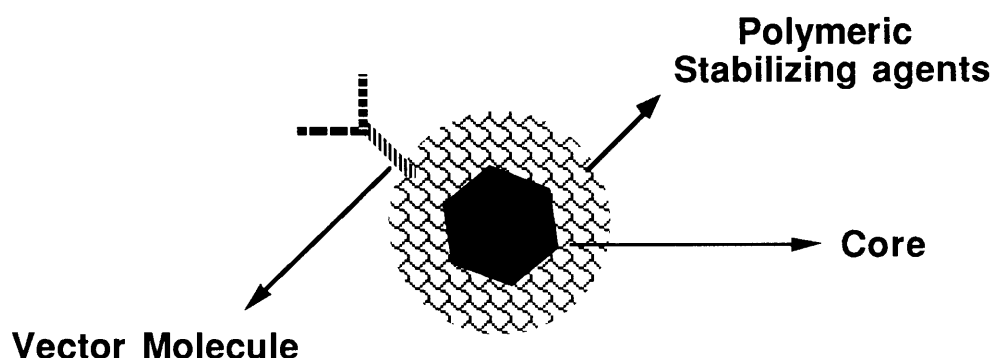


**Figure 3.1** MION: An ideal picture

Schematic representation of monocrystalline iron oxide nanocompound (MION). MION consist of a magnetically responsive core in nanometer range, solubilized with anchored surface polymers. It is hypothesized that MION can be readily reacted with a large variety of antigen-specific monoclonal antibodies, Fab fragments, or receptor-specific carbohydrates and lectins. As a result, labeled MION will have the potential to be directed to specific organs, tissues, cells, receptors, and antigens *in vivo* while exhibiting magnetic behavior detectable by MR imaging at nanomolar concentrations.

To approach the characteristics of such compound, the iron oxide synthesis methods described in the literature (Chapter 2) had to be optimized for the production of compounds with a particle size on the order of several nanometers. A variety of iron oxides were synthesized from common starting materials: Iron (II) chloride tetrahydrate ( $\text{FeCl}_2 \cdot 4\text{H}_2\text{O}$ ) and iron (III) chloride hexahydrate ( $\text{FeCl}_3 \cdot 6\text{H}_2\text{O}$ ) (Sigma Chemical Co., St Louis, MO.) were used as initial reagents. Dextran (Sigma Chemical Co., St Louis, MO.) was used as a stabilizing agent during the one-step synthesis. The solution was titrated with 2N NaOH until  $\text{pH} \approx 9$ . The resulting suspension was subjected to several cycles of centrifugation (13,000 RPM x 45 min, RT600B; Sorvall Instruments) to remove large iron oxide aggregates. A Sephadex CL-4B gel chromatography column (6x50 cm, Pharmacia LKB Biotechnology, Piscataway, NJ) was used to further purify the colloidal solution following

centrifugation. A sodium citrate buffer (0.1M, pH=8.4) was used as eluent. Samples were collected in 10 ml fractions which were then subjected to spectrophotometry (DMS100, Varian Instrument Group, Sugar land, TX) at 430 nm for measurement of iron concentration. The appropriate fractions of the elution volume were collected, and re-concentrated using a stirred ultrafiltration cell with a YM100 (molecular weight cut off 100 kd) filter (AMICON Model 8050, W.R. Grace & Co., Danvers, MA). Samples were lyophilized (Virtis Company, Inc., Gardiner, NY) and later redissolved in an isotonic Tris buffer. Figure 3.2 shows the synthesis and purification procedures of stable iron oxide colloidal suspensions schematically.

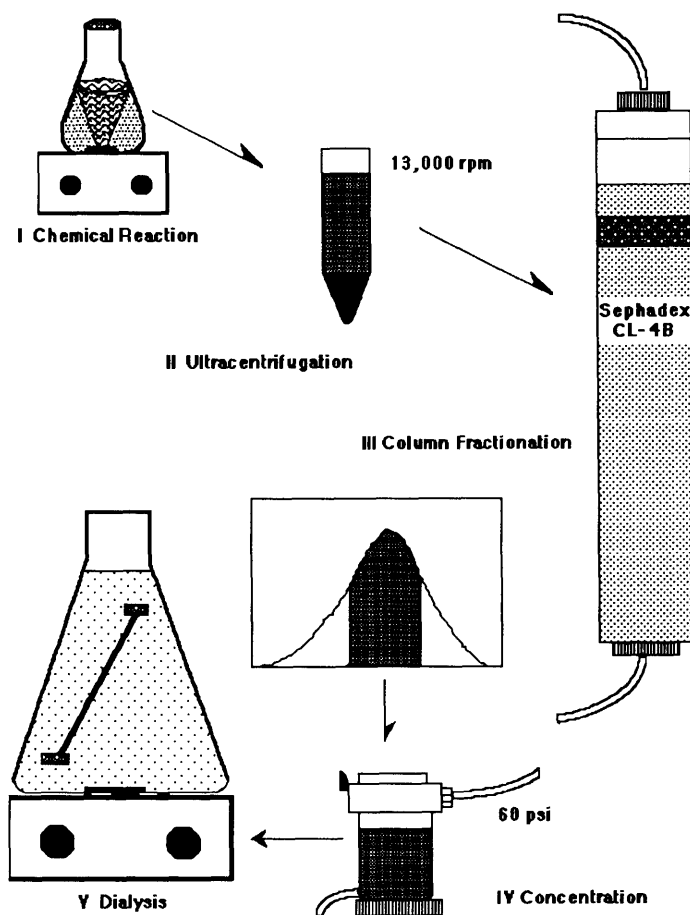


**Figure 3.2** Schematic of iron oxide synthesis

### 3.1 Core Structure

The purpose of this set of experiments was to determine an optimal initial ratio of  $\text{Fe}^{2+}$  to  $\text{Fe}^{3+}$  ions (the main parameter to influence the core structure) to form magnetic iron oxides upon oxidation in aqueous solution. Magnetite ( $\text{Fe}_3\text{O}_4$ ) and maghemite ( $\gamma\text{-Fe}_2\text{O}_3$ ) both have an inverse spinel structure. This characteristic structure determines the magnetic properties of the MION core. The magnetic properties depend upon the ratio of metal ions (i.e.  $\text{Fe}^{2+}/\text{Fe}^{3+}$ ) in the crystal structure.

The hypothesis was that different initial ratios of  $\text{Fe}^{2+}$  to  $\text{Fe}^{3+}$  ions in the reaction mixture would result in different ratios in the produced crystals, thus affecting the magnetic properties. A series of experiments was designed and carried out for the above purpose. Figure 3.3 indicates schematically the experimental set-up of this series of experiments. Iron (II) chloride tetrahydrate ( $\text{FeCl}_2 \cdot 4\text{H}_2\text{O}$ ) and iron (III) chloride hexahydrate ( $\text{FeCl}_3 \cdot 6\text{H}_2\text{O}$ ) (Sigma Chemical Co., St Louis, MO.) were used as initial reagents, dissolved in double distilled water at room temperature under constant stirring for 30 minutes. Solutions with various initial ratios of  $\text{Fe}^{2+}$  to  $\text{Fe}^{3+}$  ions were prepared. 2N sodium hydroxide solution (Sigma Chemical Co., St Louis, MO.) was used for the titration of the iron salts solution to complete the oxidation process. No stabilizing agents were used in this set of experiments to avoid possible interference in the X-ray diffraction analysis, and other parameters were kept constant. Following the oxidation, the solutions underwent centrifugation and the precipitates were washed with water three times. The reaction products were then tested for their magnetic properties with a horse-shoe magnet. The response to the magnet was used as a preliminary indication of their magnetic properties. If this test was positive, samples were freeze dried and X-ray powder diffraction and magnetic properties analyses were performed. Table 3.1 summarizes the reaction conditions and the experimental observations of this set of experiments.

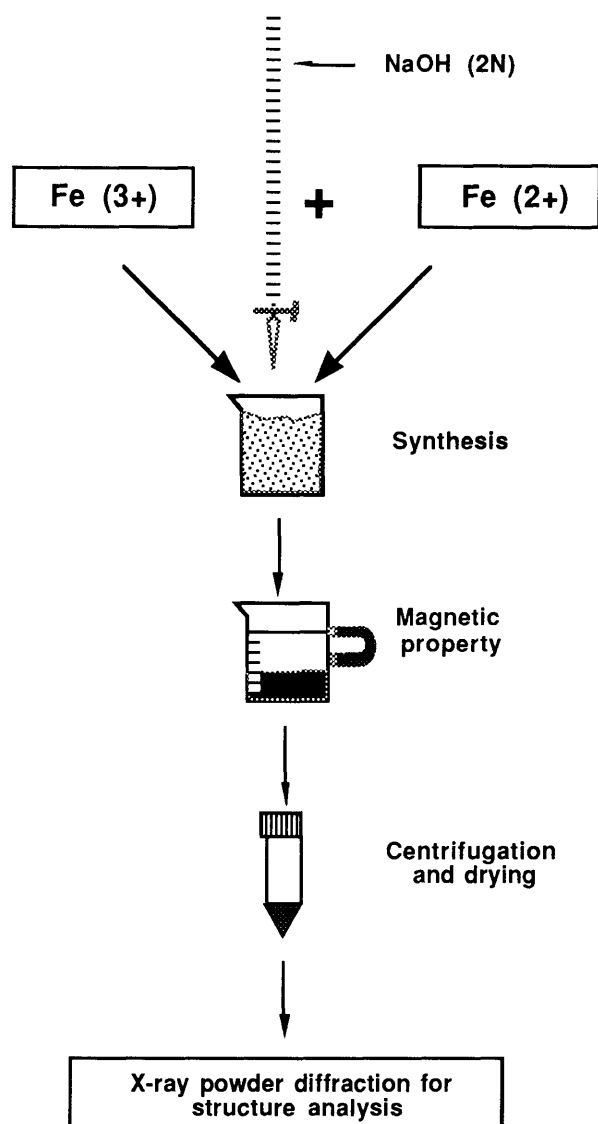


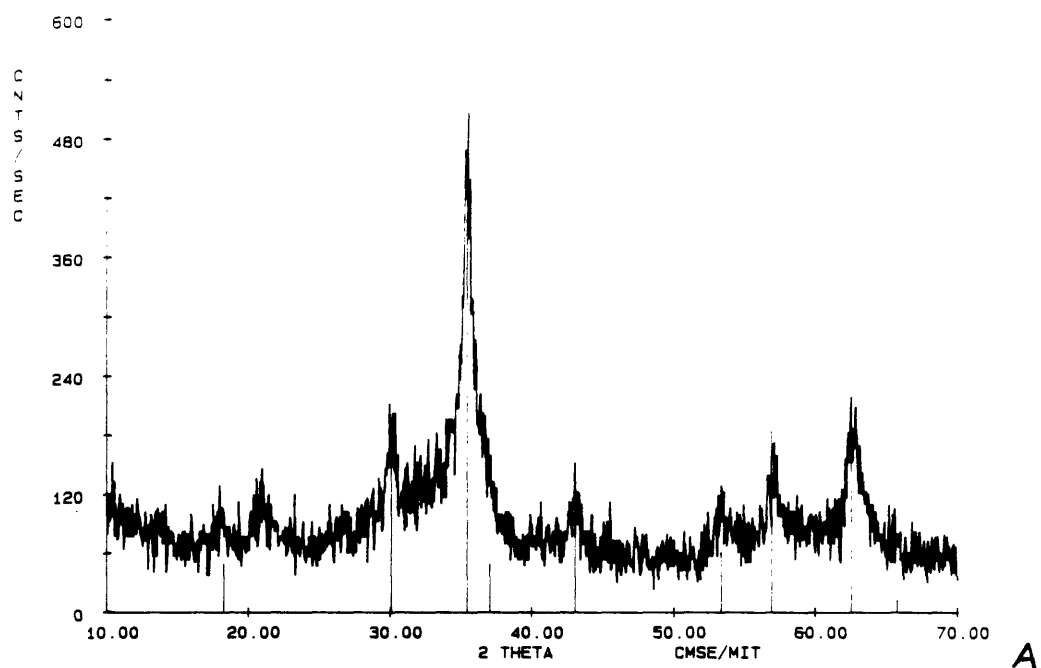
**Figure 3.3** Schematic representation of the experimental set-up of the ratio experiments. Solutions with various initial ratios of  $\text{Fe}^{2+}$  to  $\text{Fe}^{3+}$  ions were prepared. 2N sodium hydroxide solution was used for the titration of the iron salts solution to complete the oxidation process while other experimental parameters were kept constant. Following the oxidation, the reaction products were tested by a horse-shoe magnet as a preliminary indication of their magnetic properties. The solutions then underwent centrifugation, and precipitates were freeze dried for X-ray powder diffraction analyses.

X-ray powder diffraction was used to determine the crystal core structure of the MION preparations. A more detailed description of this technique will be given in chapter 4. Figure 3.4 shows X-ray diffraction spectra obtained from two batches synthesized with different initial iron ion ratios. "A" demonstrates a good correlation between the experimental data and the available literature values. However, "B" shows two major mismatch diffraction peaks as compared with the diffraction spectrum of magnetite indicating the presence of impurities. As a preliminary indication, the initial ratio of 0:1 solution yielded a non-magnetic end product (no response to the magnet). X-ray analysis further confirmed the structural difference between these samples. In summary, the initial ratio of ferric to ferrous ions should be less than or equal to 2.

**Table 3.1 Ratio Experiments**

Fe <sup>2+</sup> /Fe <sup>3+</sup> + Ratio	SQUID Analyses	X-ray diffraction	Observations
0:1	Diamagnetic	Non- magnetite	Red complex formed at low pH (<2). Upon further titration, brown precipitates formed at room temperature. No response to the magnet.
1:10	paramagnetic	Non- magnetite	Red complex formed at the beginning of the titration process. Precipitate showed no visible response to the magnet.
1:2	ferromagnetic	Magnetite	Green complex formed at low pH ( $\approx 3$ ), black precipitate formed upon heating at high pH (>9). Clearly visible response to the magnet.
1:1	super- paramagnetic	Magnetite	green complex formed upon slow titration and heating (80° C), black precipitate formed. Precipitate showed visible response to the magnet.
2:1	super- paramagnetic	Magnetite	Green complex formed at low pH ( $\approx 2$ ). Precipitate formed upon heating (80° C) showed visible response to the magnet. Excess Fe <sup>2+</sup> in supernatant after centrifugation.

Total reaction volume was 250 ml, temperature was 25° C, and titration rate was kept constant for all batches.



Z19227 8/ 1/91 S= 0.050 T=10.000  
PDF ( 1) =19.629 Fe<sub>3</sub>O<sub>4</sub>

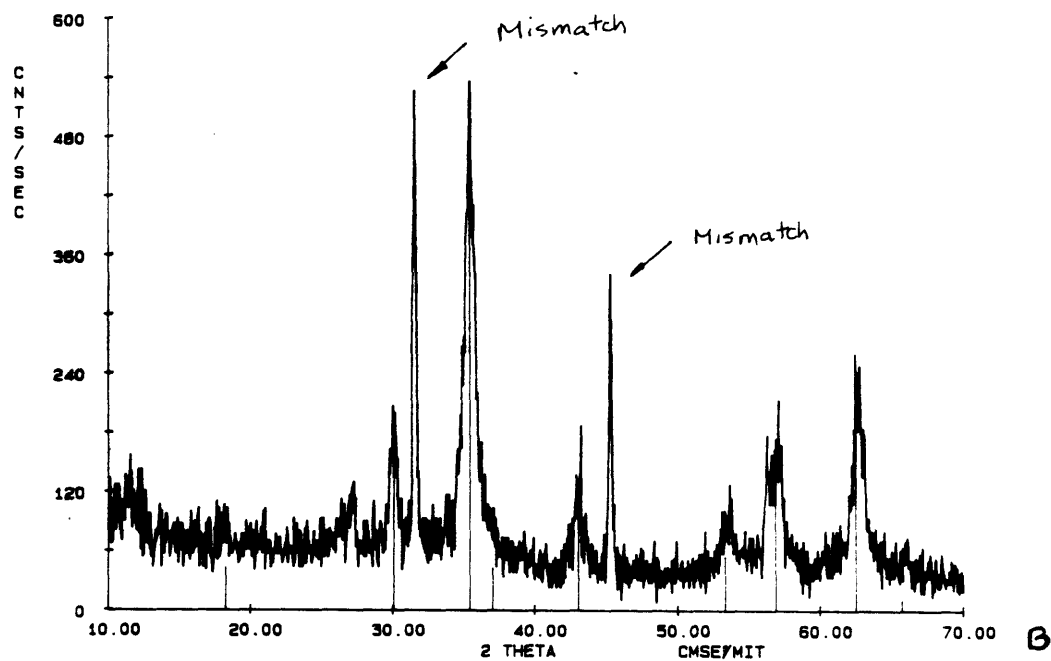


**Figure 3.4** X-ray diffraction spectra obtained from two batches of iron oxides synthesized with different initial iron ion ratios. Note the mismatch of diffraction intensities of sample B compared to the literature values for  $\text{Fe}_3\text{O}_4$  at 2 Theta of 32 and 46 degrees.



## 3.2 Core Size

To ensure adequate distribution of MION *in vivo* as a MR contrast agent, its size needs to be controlled carefully. The small size of an agent offers several advantages: first, it allows passage of these agents through the vasculature, a prerequisite for targeting; second, it minimizes the chance of recognition by the body's defense system (RES in particular); third, it reduces the toxicity and the chances of inducing immune responses when used *in vivo* while still retaining the magnetic properties needed for contrast enhancement.

The core size can be influenced by the synthesis temperature, and by the kind and concentration of the stabilizing agents used during synthesis. The initial reaction temperature has a significant effect on the crystalline size distribution formed from the oxidation process. Figure 3.5 indicates schematically the general approach for this set of experiments, designed to examine the temperature effect on particle size. Initial solutions of iron ions were prepared at different temperatures, then titrated by NaOH (2N) solution of the same temperature. The end product from each batch then underwent primary size analysis by light microscopy, filtering, membrane filtration and transmission electron microscopy.

Figure 3.6 shows scanning electron micrographs of freeze-dried MION preparations, synthesized at two different initial reaction temperatures. *A* was synthesized at 25° C, and *B* was synthesized at 4° C. The average particle size is much smaller at the lower initial temperature, and the particle size distribution was also narrower according to particle size analysis. The particle size of MION was analyzed with a high resolution transmission electron microscopy (HRTEM). A detailed description of this technique will be given in chapter 4. Figure 3.7 represents the particle size distribution of the two preparations shown in Figure 3.6. Diameters of 600 individual crystals from the

micrographs were used to calculate average particle size and distribution. Consistent with the TEM findings, the sample synthesized at 4° C has a narrower distribution and smaller average size than that of 25° C. Figure 3.8 demonstrates that the initial reaction temperature is an important parameter to control the average particle size in the final product (Figure 3.8a). As the initial temperature increases, the average particle size increases accordingly. In general, the increase in temperature will increase the rate of iron complex aggregation, leading to larger particle size in the final product. Note also at the lowest temperature, there is an increase in average particle size due to the high viscosity and poor mixing process near the freezing point. To synthesize nanometer scale magnetite particles, a temperature of 4° C is preferred.

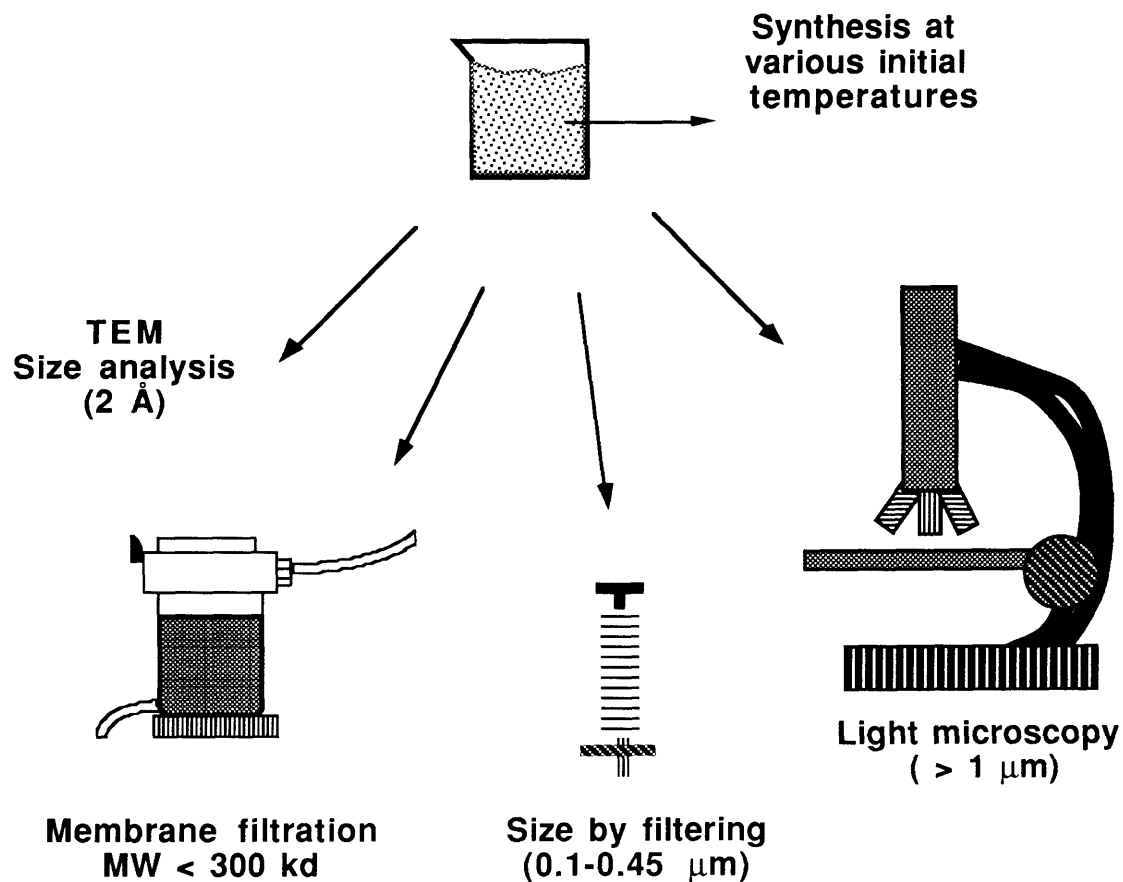


**Figure 3.5** Core size optimization experiment set-up

Solutions of iron ions were prepared at different initial temperatures. Oxidation was completed by titration with NaOH (2N). The end product from each batch then underwent primary size analysis by light microscopy, filtration and TEM.

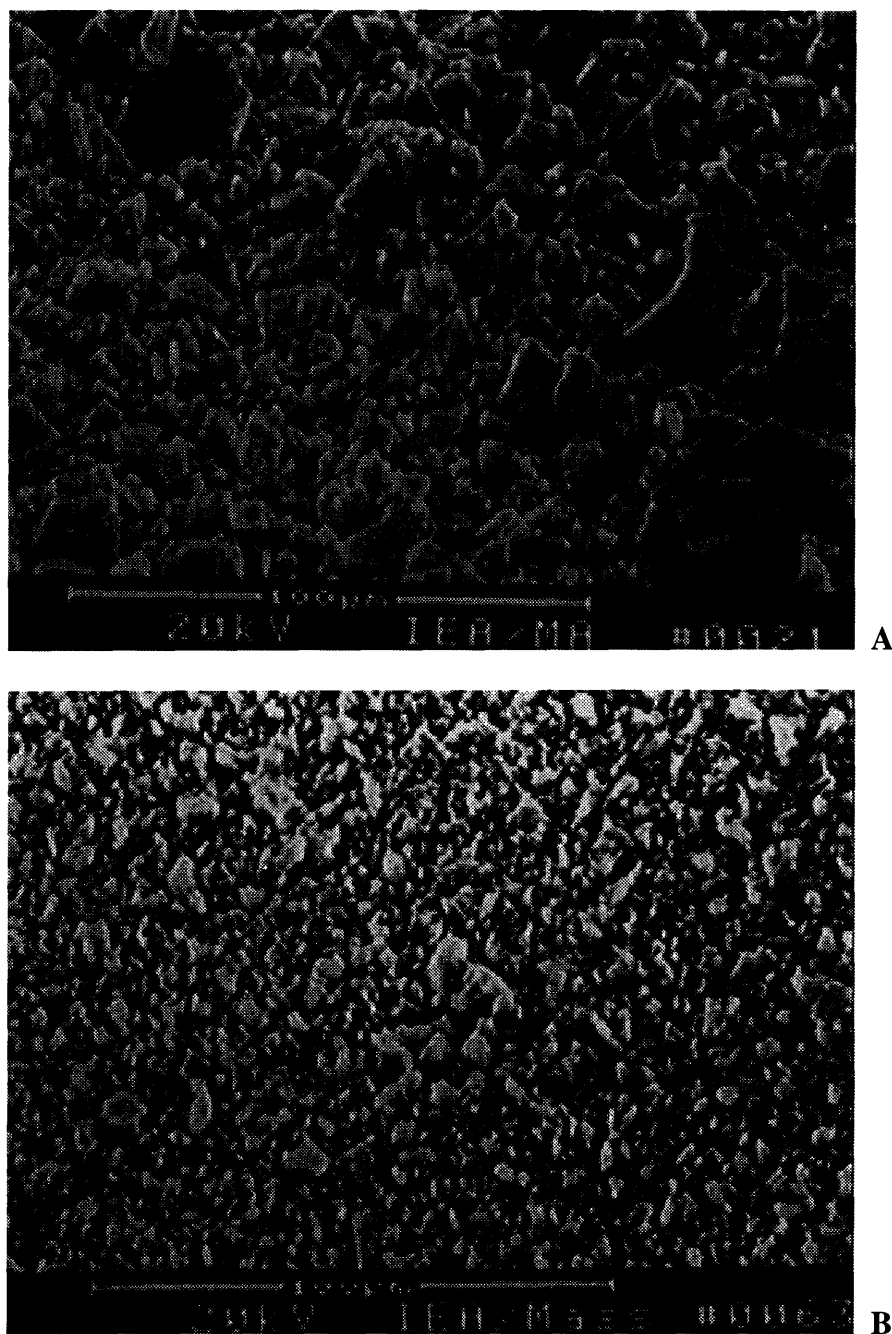


**Figure 3.6** Scanning electron micrographs of freeze-dried MION preparations synthesized at two different initial reaction temperatures. A was synthesized at 25 °C, and B was synthesized at 4 °C. The average particle size is much smaller at lower initial temperature, and the particle size distribution was also narrower according to particle size analysis.

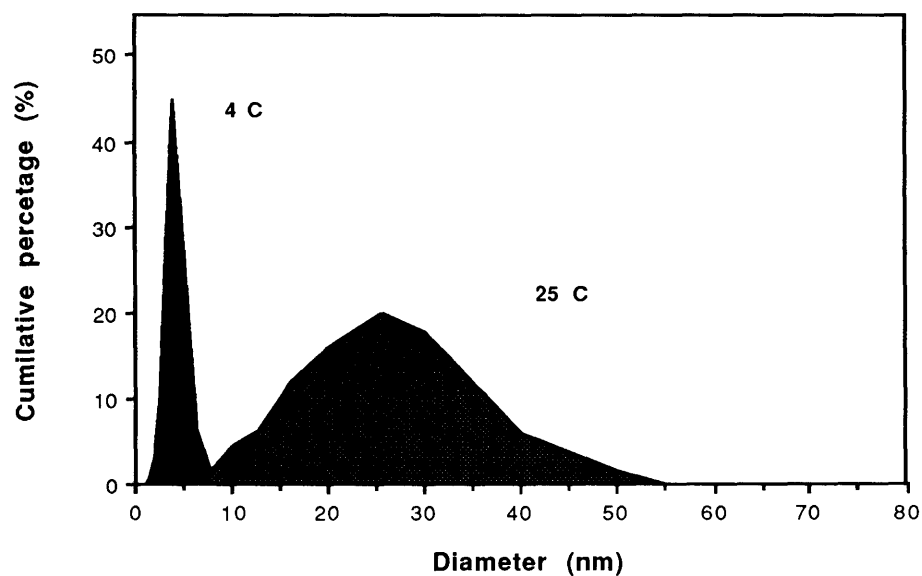


**Figure 3.7** Particle size distribution of two preparations from Figure 3.6. Particle size of MION was analyzed with high resolution transmission electron microscopy (HRTEM). Diameters of 600 individual crystals from the micrographs were used to calculate average core particle size and distribution. Consistent with the TEM findings, the sample synthesized at 4° C has a narrower distribution and smaller average size than that of 25° C.

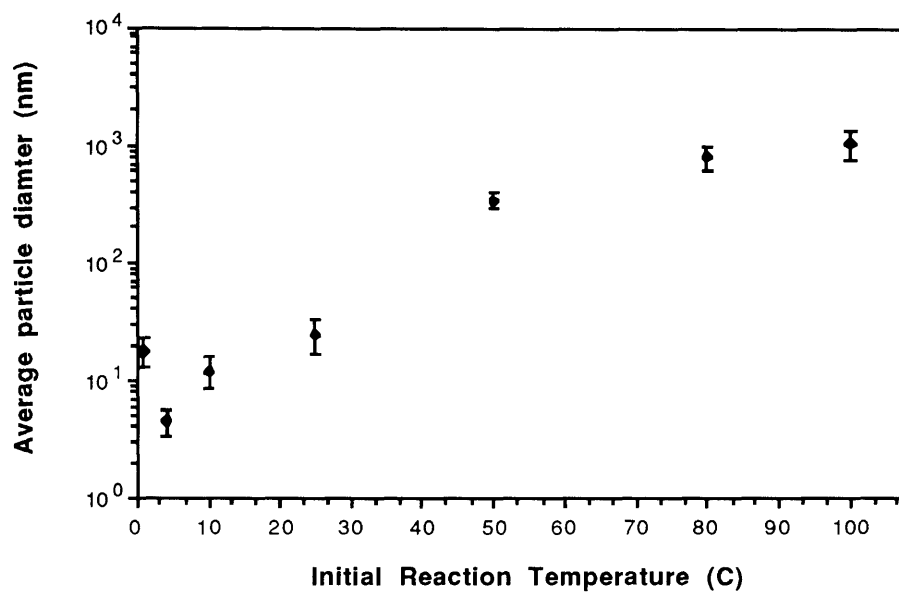


**Figure 3.8** The initial reaction temperature is an important parameter to control the average particle size in the final product. As the initial temperature increases, the average particle size increases accordingly. Note also at the lowest temperature, there is an increase in average particle size due to the high viscosity and poor mixing process at the near freezing point. For production of nanometer scale magnetite particles, temperature of 4° C is preferred.

### **3.3 Stability**

#### ***3.3.1 Polymeric Stabilizing Agents***

The effect of Dextran as a stabilizing agent on the iron oxide crystals was examined. Polymeric stabilizing agents play an important role in increasing the stability of the iron oxide colloidal solution (decrease aggregation), and to provide a means to conjugate them to carrier molecules or, in some cases, to serve as targeting molecules themselves.

Iron oxides were synthesized from solutions with initial Dextran concentrations ranging from 0 to 25 percent. Figure 3.9 shows the effect of Dextran concentration on formation of colloidal solution. At low initial Dextran concentration, nearly all iron oxide particles formed during oxidation precipitated from the solution. On the other hand, as the initial Dextran concentration increased to 20%, all iron oxide crystals were stabilized in colloidal form by the dextran polymers. The Dextran solution decreases the mobility of iron complexes and therefore inhibits their aggregation. A Dextran concentration of 15% was therefore chosen in the initial reaction solution. This concentration maximized the formation of colloidal iron oxides, and also minimized the high viscosity and poor mixing caused by high concentration of dextran polymers.

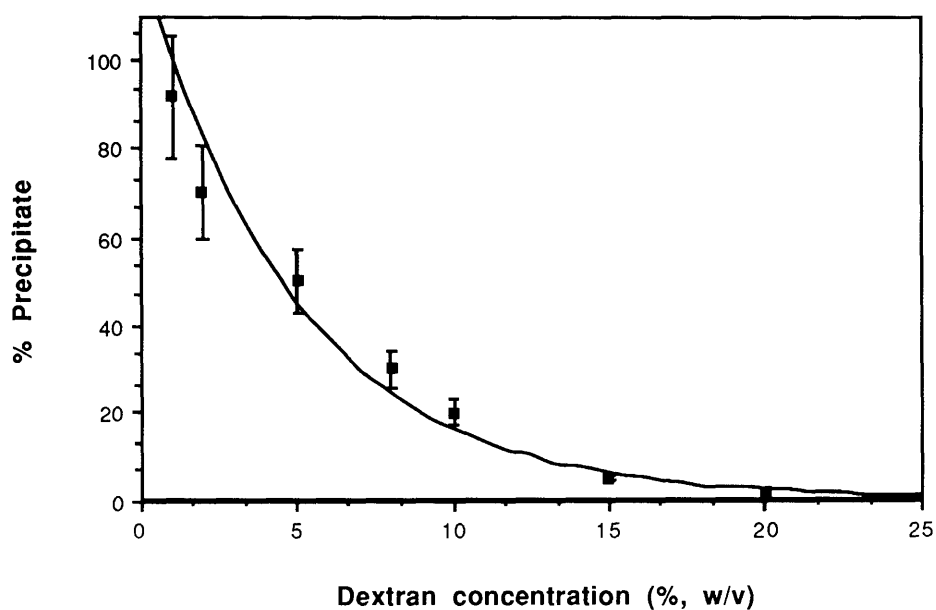


**Figure 3.9** The effect of polymeric stabilizing agents on formation of colloidal solution. In this graph, the percentage of precipitate at the end of the synthesis is plotted as a function of initial Dextran concentration (w/v).

### 3.3.2 Effect of Surface Coating on Magnetic Properties

Various polysaccharides were specifically chosen to alter the biodistribution of the iron oxide particles via *in vivo* targeting of sugar receptor systems on hepatocytes. These iron oxide compounds were synthesized as described previously (chapter 3.2.1), but instead of dextran the following polysaccharides were used: chitosan (ICN Biochemicals, Inc., Cleveland, Ohio), mannan (Sigma Chemical Co., St. Louis, MO), arabinogalactan (Aldrich



Chemical Company, Inc. Milwaukee, Wis), and fucoïdan (Sigma Chemical Co., St. Louis, MO).

The following table summarizes the relaxation rates of MION samples with different polysaccharide surface coatings. The relaxation rates obtained for the different compounds vary little, compared to the various caused by varying the size of the particle core (Table 3.2). This observation indicates that the surface coating has little effect on magnetic properties of the superparamagnetic core and can thus be used for coupling to a variety of carrier molecules.

**Table 3.2 Effects of surface coatings on relaxivity**

Compound	R1 (mmol/L sec <sup>-1</sup> )	R2 (mmol/L sec <sup>-1</sup> )	R2/R1
MION-Dextran 9.4 *	1.5	3.2	2.1
MION-Dextran 11.0 **	2.4	4.5	1.9
MION-Mannan	1.9	3.4	1.8
MION-Chitosan	1.4	2.2	1.7
MION-Fucoïdan	0.8	1.8	2.3
MION-Arabinogalactan	1.7	3.2	1.9

\* MW 9,400 dextran, \*\* MW 11,000 dextran

### 3.3.3 Stability of MION

The stability of MION preparations was examined under various storage conditions. The relaxivity value was used as an indicator of changes in stability. These experiments provide valuable information on future shelf-life stability of MION when used clinically.

Samples were subjected to thermal manipulations, and their relaxivities were measured under each condition. Table 3.4 summarizes the percentage relaxivity changes corresponding to the change in thermal conditions.

**Table 3.3 Thermal stability evaluation**

Storage Conditions	% change in R2*
4° C for 24 hours (control)	--
-10° C for 24 hours	-1.30%
-84° C for 24 hours	- 4.70%
freeze dried (redissolved)	0.50%
heated for 30 minutes	4.50%

\* < 5% is not statistically significant

It is evident that there is little change in the relaxivity following various forms of storage. Lyophilization resulted in the smallest change in R2 relaxation rates. The lyophilized MION can be easily redissolved in physiological buffer. This is especially useful because lyophilization is most convenient storage condition for future clinical application.

In summary, the optimized synthesis of MION is as follows:

FeCl<sub>3</sub>•6H<sub>2</sub>O (10 g) and FeCl<sub>2</sub>•4H<sub>2</sub>O (3.9 g) were dissolved in water at 4 °C as the initial reagents, and Dextran (150 g) (Sigma Chemical Co., St Louis, MO.) was used as a

stabilizing agent during the one-step synthesis. The solution was titrated with 2N NaOH until pH  $\approx$  9, when a dark complex formed. Dextran (Sigma Chemical Co., St Louis, MO.) was used as a stabilizing agent during the one-step synthesis. The solution was titrated with 2N NaOH until pH  $\approx$  9. The resulting suspension was subjected to several cycles of centrifugation (13,000 RPM x 45 min, RT600B; Sorvall Instruments) to remove large iron oxide aggregates. A Sephadex CL-4B gel chromatography column (6x50 cm, Pharmacia LKB Biotechnology, Piscataway, NJ) was used to further purify the colloidal solution following centrifugation. A sodium citrate buffer (0.1M, pH=8.4) was used as eluent. Samples were collected in 10 ml fractions which were then subjected to spectrophotometry (DMS100, Varian Instrument Group, Sugar land, TX) at 430 nm, the wavelength at which previous experiments had shown optimum absorbence of polymeric iron compounds. The appropriate fractions of the elution volume were collected, and re-concentrated using a stirred ultrafiltration cell with YM100 filter (AMICON Model 8050, W.R. Grace & Co., Danvers, MA). The concentrated sample was then dialyzed against Trisaminomethane (Tris) buffer (0.025 M, pH=7.2) to complete the preparation for clinical evaluation. Samples were lyophilized (Virtis Company, Inc., Gardiner, NY) and later redissolved in isotonic Tris buffer.

### 3.4 Conjugation to Carrier Molecules

Having optimized the synthesis of the MION core, the next important step was to establish conjugation of the magnetic label to a variety of carrier molecules to achieve in vivo targeting. In some cases, the surface coating of MION itself can serve as target specific molecules such as in the case for some same containing sugars described previously. Furtherre, there are two approaches in conjugating MION to a variety of carrier molecules. One is to establish covalent binding between the surface coating and the carrier molecules. The other is to achieve noncovalent electrostatic conjugation of MION and the carrier molecules.

As an example of conjugation of carrier molecules to the MION surface, MION was attached to indium-111-labeled human polyclonal Immunoglobulin (IgG). IgG can be used to target sites of acute inflammation. Indium-111 was attached to human polyclonal IgG (modified for intravenous use (Cutter Biological, Berkeley, CA)) via DTPA by the carboxy-carbonic anhydrate method in order to confirm the attachment of the protein to MION. The DTPA-coupled IgG was diluted to 8.8 mg/ml (protein/0.9% NaCl). Before column fractionation, IgG-DTPA was labeled with sterile, pyrogen free In-111-Cl<sub>3</sub> (10mCi/ml; Amersham, Arlington Heights, Ill) with citrate transchelation. Approximately 1.5  $\mu$ Ci of In-111-Cl was combined with 150  $\mu$ L of sterile 0.1 mol/L sodium citrate (pH=5.4) to which 100  $\mu$ l of DTPA-coupled IgG of 8.8 mg/ml was added. The solution was incubated at room temperature for 15 minutes. Radiochemical purity was then determined by chromatography (10 ml Sephadex G25 column; Pharmacia, Piscataway, NJ). Radioactivity was counted with a gamma counter (Wallac OY, Turku, Finland).

The conjugation of MION to In-111-labeled IgG was achieved by reacting 0.3 mg of IgG with MION containing 1mg of iron in a buffered solution of NaCl and NaPO<sub>4</sub> (0.145 M).

The mixture was then sonicated in an ice bath (Branson 450 sonifier; Branson Ultrasonics, Danbury, Conn). With this non-covalent method, the amino acid groups (predominantly histidine, serine and tryptophan) of IgG interact electrostatically with the hydroxyl groups on the surface of MION to form a stabilized conjugate in the colloidal solution. The resulting samples were evaluated with column chromatography and relaxation time measurements. Figure 3.10 shows the results of column chromatography of MION-In<sup>111</sup>-IgG complex, confirming the attachment of MION to IgG.

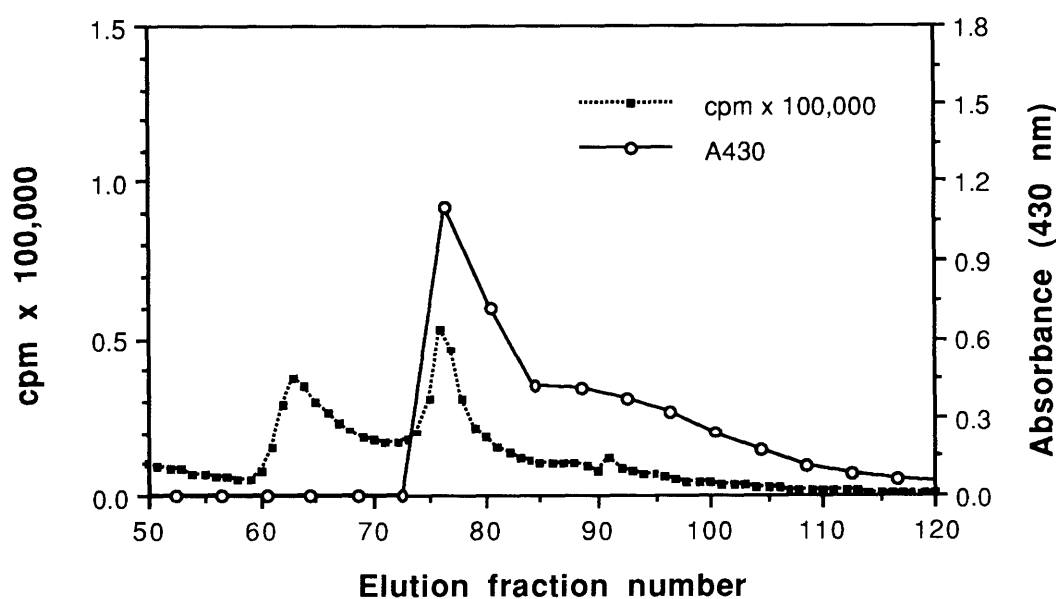


**Figure 3.10** Attachment of IgG to MION. Anion exchange column chromatography of the non-covalently bound MION-In<sup>111</sup>-IgG complex. The first In<sup>111</sup> peak corresponds to In<sup>111</sup>-IgG which has not attached to MION. The second In<sup>111</sup> peak corresponds to MION-In<sup>111</sup>-IgG complex. Absorbance of the elution fractions at 430 nm was used to determine the iron content of the product. Note that the iron peak determined by colorimetry overlaps with the In<sup>111</sup>-IgG-MION peak obtained from gamma counting.

The second example for conjugating MION to carrier molecules was Asialofetuin (ASF).

A model to study receptor specificity of a MR contrast agent is the system of asialoglycoprotein (ASG) receptors, localized on the hepatocytes. ASF is a plasma protein with high affinity to the ASG receptor. The attachment of MION to ASF can be accomplished by a periodate oxidation method which oxidize the surface coating (dextran in this case) of MION followed by attachment of specific molecules to the oxidized dextran (Dutton, Tokuyasu et al. 1979). MION-ASF was synthesized by reacting 0.3 mg of ASF (Sigma Chemical Company, St. Louis, MO) with 1 mg of MION with a periodate method. This complex was prepared for in vivo evaluation by MR imaging in a later chapter.

### **3.5 Summary**

The factors which affect MION core structure, size and stability in colloidal solution have been systematically investigated in this chapter. To summarize:

- Initial ratio of Fe(II) to Fe (III) is important to control the final chemical composition of the precipitate. According to the reaction mechanism, the initial ratio of Fe(III) to Fe(II) should be less than or equal to 2.
- Initial reaction temperature is important for control of the average particle size precipitated from the solution. For production of nanometer range magnetite particles, initial temperature was optimized at 4° C.
- Stabilizing agents, Dextran for example, are important to control the stability of the colloidal solution. The initial concentration of Dextran was optimized to be >15 %.
- Other polysaccharides and proteins were successfully conjugated to MION for target specific delivery. Changes in surface coating showed little influence on the magnetic properties of MION.

## **Chapter IV**

# **Physicochemical Characterization**

Having established the optimized synthesis for monocrystalline iron oxide nanocompound described in the previous chapter, a detailed physicochemical characterization of MION was carried out. Various techniques were used to evaluate the physicochemical properties of these agents. Figure 4.1 summarizes the characterization techniques used in this chapter. These include transmission electron microscopy (TEM) for core size estimation, X-ray powder diffraction for structural analysis, spectrophotometry for chemical composition analysis, laser light scattering (LLS) for the hydrodynamic radii measurement of MION, and superconducting quantum interference magnetometer and Mössbauer spectroscopy for magnetic property measurements. The relaxivities of MION in aqueous phantoms were also evaluated by NMR. Finally, a computer generated model of MION was created based on the obtained physicochemical parameters. In the following section, results from the above categories will be presented. For the characterization of some aspects of MION, more than one technique was used to eliminate any ambiguity, or to obtain supplemental information.



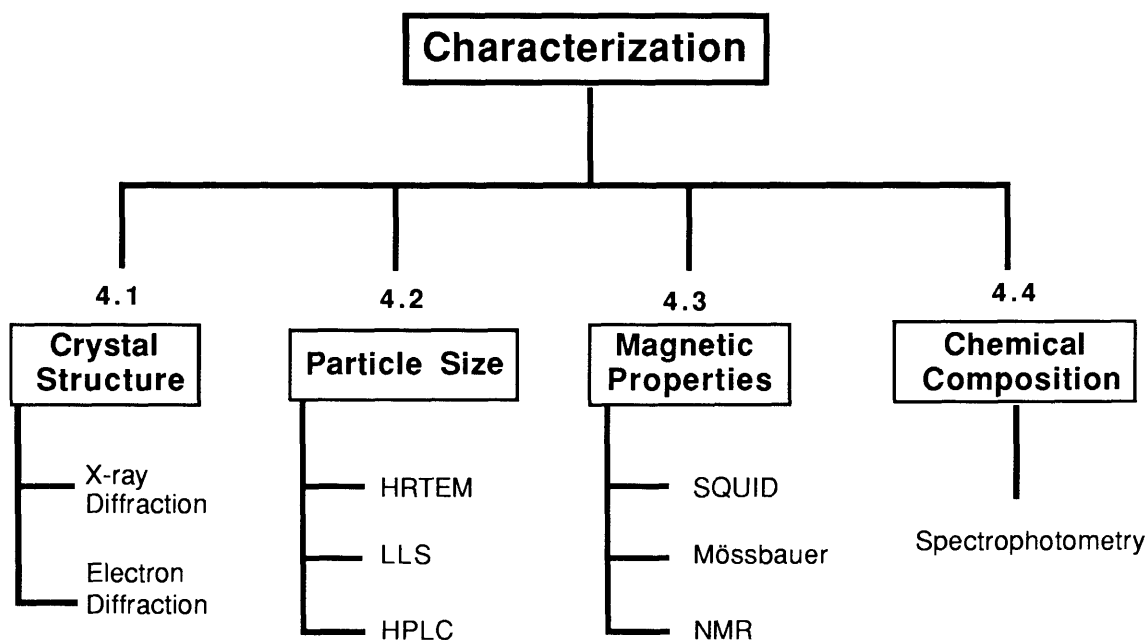


**Figure 4.1** Organization of physicochemical characterization techniques.

## 4.1 Crystal Structure

X-ray powder diffraction was used to determine the crystal core structure of MION. In this technique, a lyophilized sample powder is exposed to an X ray at various angles. The symmetries and intensities of the reflections (Bragg reflections) from the sample are recorded and graphed as a function of the beam angle ( $2\theta$ ). In our experiment, an X-ray diffractometer (REGAKU 300, Japan) was operated with a source wavelength of  $1.54 \text{ \AA}$ . The diffraction spectrum was obtained by continuously scanning angles from  $20^\circ$  to  $100^\circ$  at  $0.02^\circ$  resolution. The total scanning time was 4 minutes per sample.

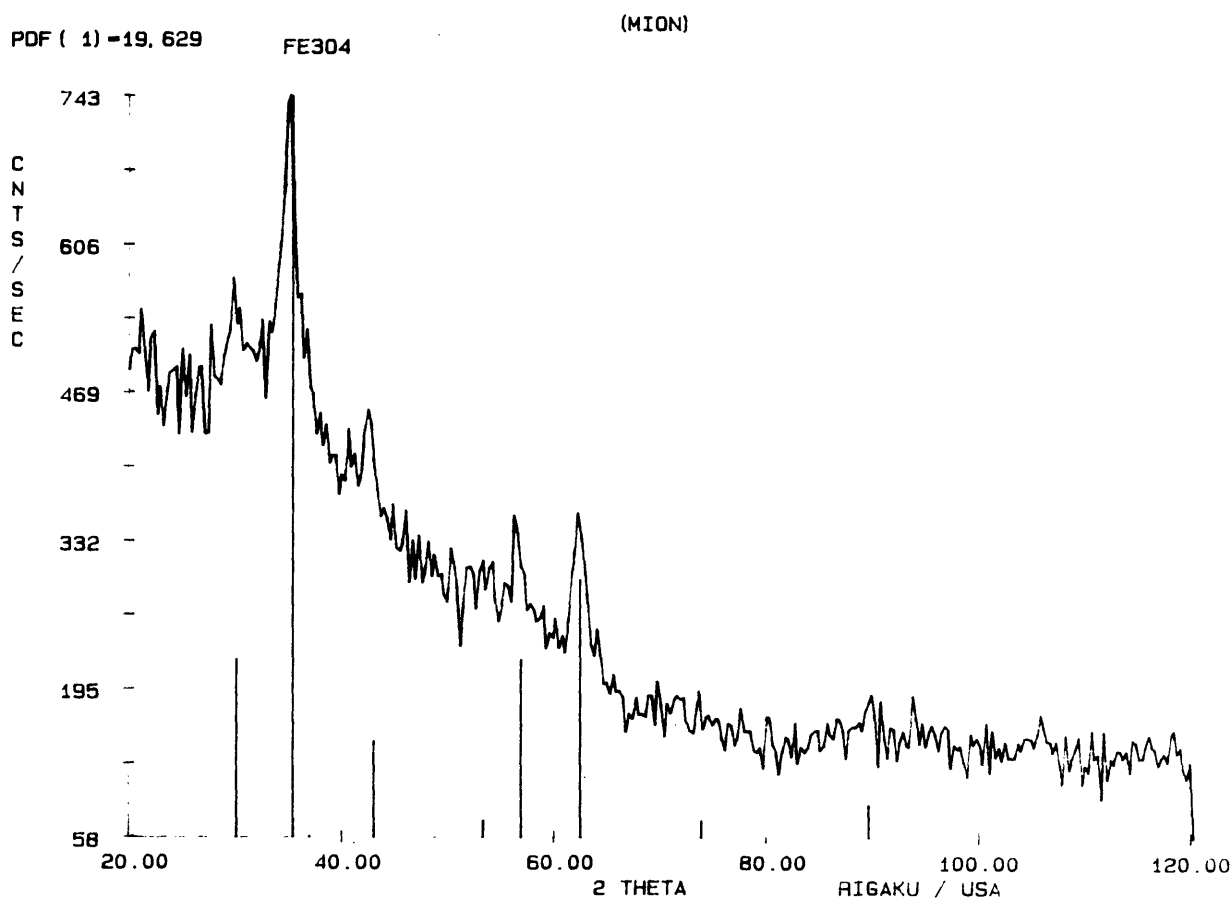
Figure 4.2 represents a typical X-ray diffraction spectrum obtained from a powdered MION. The diffraction intensity is plotted as a function of diffraction angle. The vertical lines represent literature values of  $\text{Fe}_3\text{O}_4$  published by the National Bureau of Standards (JCPDs, Washington, D.C., 1967). There is a good correlation between the experimental

data and literature values (> 94% agreement), both with respect to the diffraction angle and the relative intensity of the peaks, indicating the magnetite crystal structure of MION cores. If impurities would be present, other peaks would arise, or the relative intensities of the peaks would not match (as shown in Figure 3.4 b).

Electron diffraction experiments were performed on a high resolution transmission electron microscope (HRTEM) to confirm the X-ray diffraction data. A selected-area electron diffraction pattern of a MION core was obtained from HRTEM at an operating voltage of 200 KV as shown in figure 4.3. The camera length was calibrated using a gold standard, and the lattice spacings were then calculated from the diffraction patterns. The calculated lattice spacings were compared to the results from X-ray diffraction experiments, and are shown in Table 4.1. The diffraction patterns show that the MION core consists of a single crystal, and confirmed by the good agreement between these two sets of experiments.

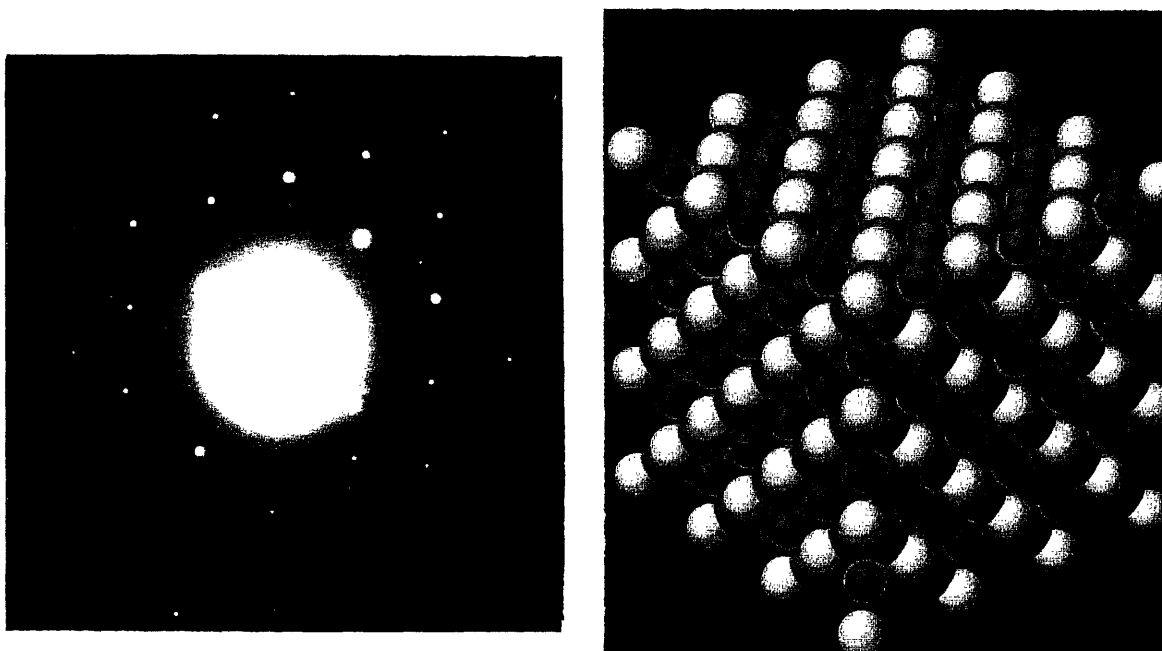
**Table 4.1 Lattice spacings in MION crystal**

<b>X-ray Data (Å)</b>	<b>EDP data (Å)</b>
4.85	4.82
2.97	2.97
2.53	2.56
2.10	2.12
1.72	1.74
1.62	1.62
1.49	1.51
1.33	1.34
1.28	1.28
1.21	1.21
1.12	1.12



**Figure 4.2** X-ray powder diffraction spectrum of MION

Both the symmetries and intensities of the diffraction spectrum confirmed the well ordered crystal structure. Despite of the similarities of the diffraction angles and intensities in the spectrum of MION sample, they are not identical to the published standards for magnetite, because of the surface bound dextran of MION. Note the difference between this spectrum and Figure 3.4A which was obtained without surface-bound dextran coating.

**e- Diffraction****Inverse Spinel****A****B**

**Figure 4.3** **A** is the diffraction pattern obtained from selected-area electron diffraction of a single crystal MION core. The operating voltage was 200 KV (JEOL-200 HRTEM, MIT). Camera length was calibrated using a gold standard, and lattice spacings were then calculated from the radii of the diffraction patterns (Table 4.1). The pattern is consistent with the model of magnetite. **B** shows the ideal packing of atoms in a unit cell of inverse spinel containing  $8[XY_2O_4]$ . The red spheres are oxygen atoms, white spheres representing tetrahedral sites, and octahedral sites. The magnetite crystal structure is an inverse spinel structure, where  $M(II)=Fe(II)$ , and  $Y(III)=Fe(III)$  (Verwey and Heilmann 1947).

## **4.2 Particle Size**

### ***4.2.1 Electron Microscopy (EM) Analysis***

The magnetic iron oxide cores of MION are electron dense and visible directly under a transmission electron microscope (TEM). Therefore high resolution TEM (HRTEM) can be used for particle size analysis of the MION core. Scanning electron microscopy (SEM) was used for the morphologic analysis of solid MION.

MION specimen for HRTEM and SEM were prepared by direct fixation of freeze dried MION powder or diluted solutions of MION on mixed cellulose ester (MCE) filters, followed by low temperature plasma etching, and carbon coating in a high vacuum coating unit. This preparation produced an intact carbon film which was sufficiently clear for analysis. HRTEM micrographs were taken with a JEOL 200 CX (point to point 2.6 Å) and ABT EM-002B (point to point 2.0 Å). Diameters of 600 individual crystals from the micrographs were used to calculate average particle size of MION preparation.

Figure 4.4 represents a typical HRTEM micrograph of MION. The electron dense cores show a characteristic hexagonal shape produced by the 2-D projection of the cubic crystal structure. The average particle size was  $4.6 \pm 1.2$  nm in diameter. No particle aggregates were present, and electron diffraction patterns confirmed that each core was a single crystal of magnetite.

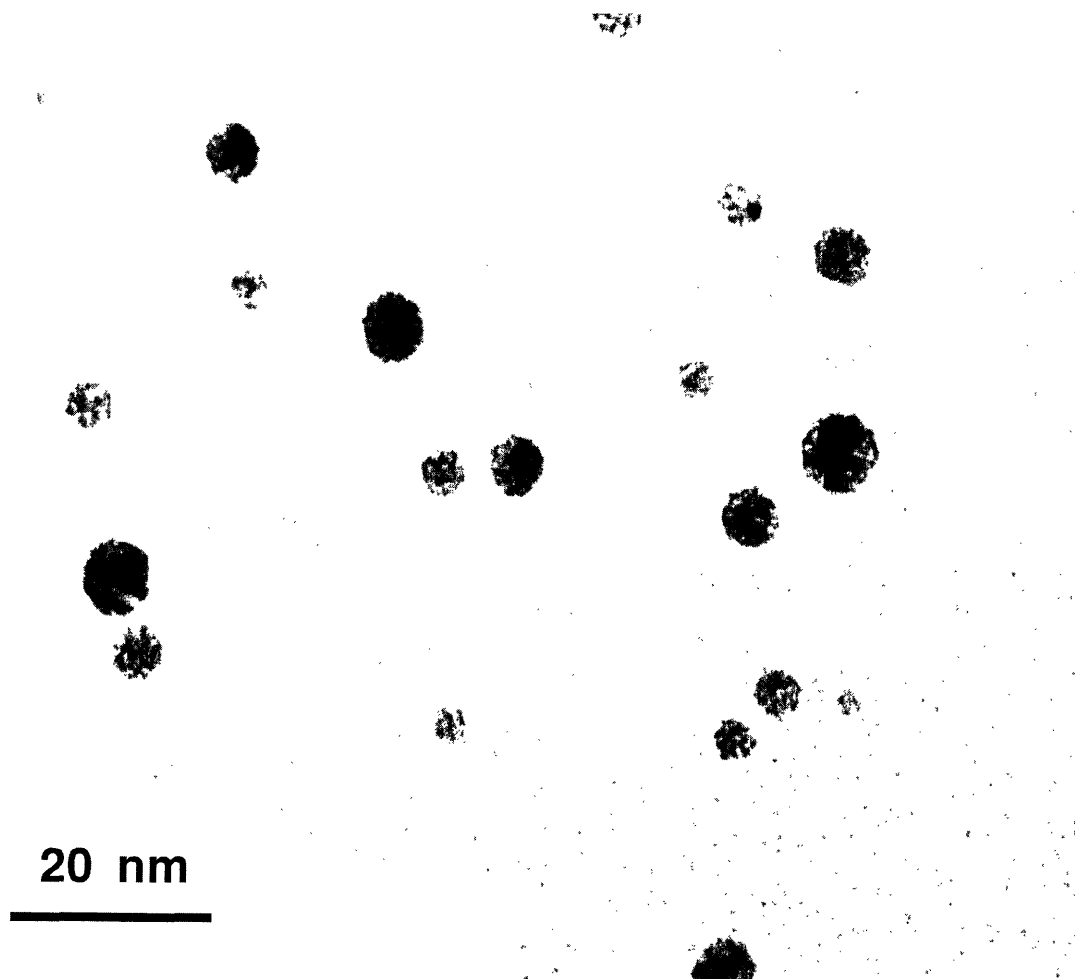


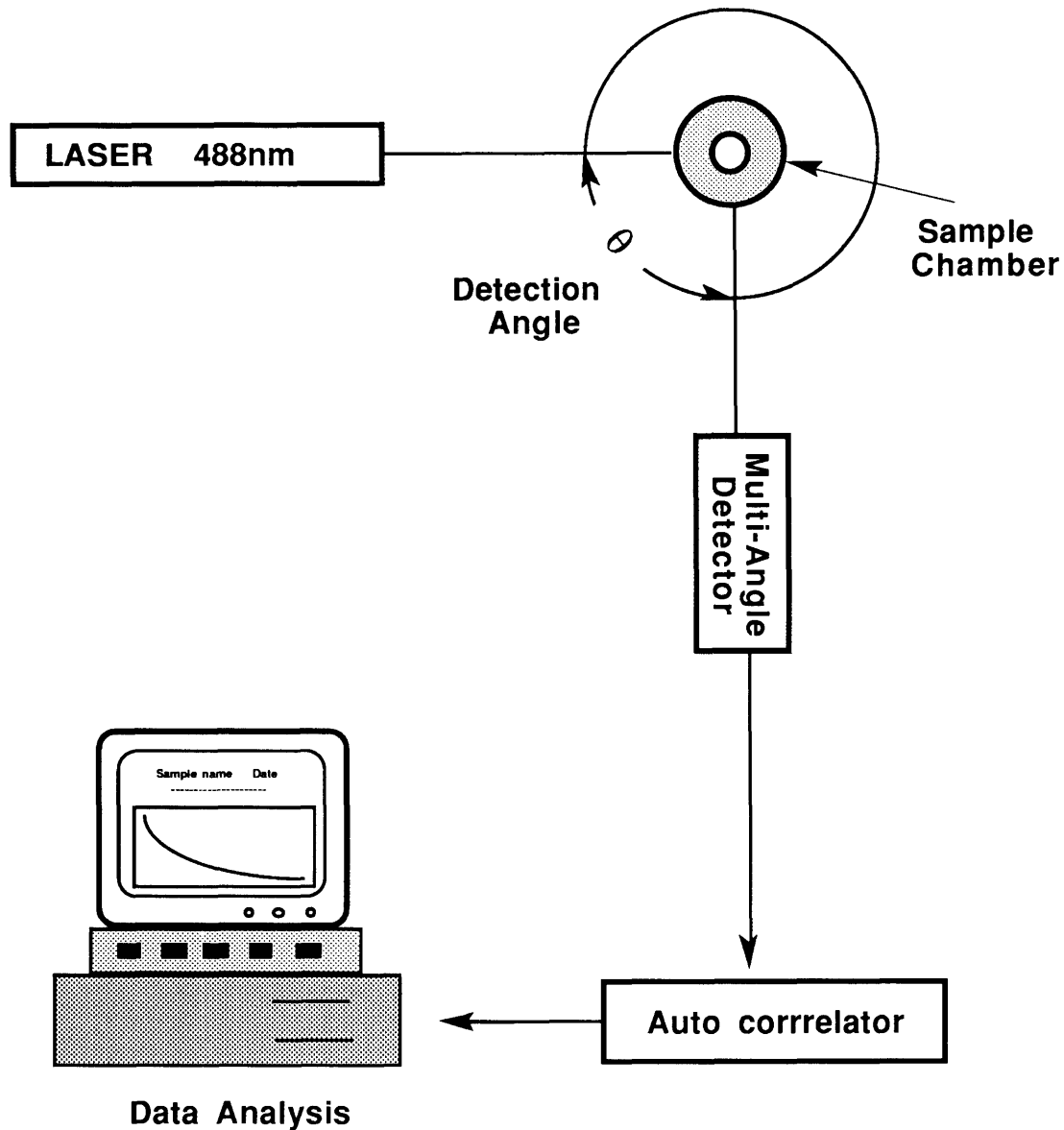
**Figure 4.4** A high resolution electron micrograph of a MION preparation. MION consists of an electron-dense crystalline core and surface bound dextran (not visible by electron microscopy). The cores appear to have a hexagonal shape by electron microscopy and typically measure  $4.6 \pm 1.2$  nm in diameter. The shape of crystals showed good correlation with the theoretical representation (Figure 4.3b). No particle aggregates were present, which makes this compound a unique label for targeting purposes.

#### **4.2.2 Hydrodynamic Radii by LLS**

The hydrodynamic radii of a colloidal solution can be measured by light scattering techniques, i.e. photon correlation spectroscopy (PCS). The size analysis of colloidal particles by PCS has been described in detail by Douglas et al. (Douglas, Illum et al. 1984). PCS theory is based on Brownian motion of particles dispersed in a liquid. Smaller particles move more quickly than larger ones, therefore the frequency at which the particles move is correlated to their sizes. In a typical light scattering experiment, the particles in the liquid are illuminated by a laser source, and the scattered light is analyzed using a photon correlator.

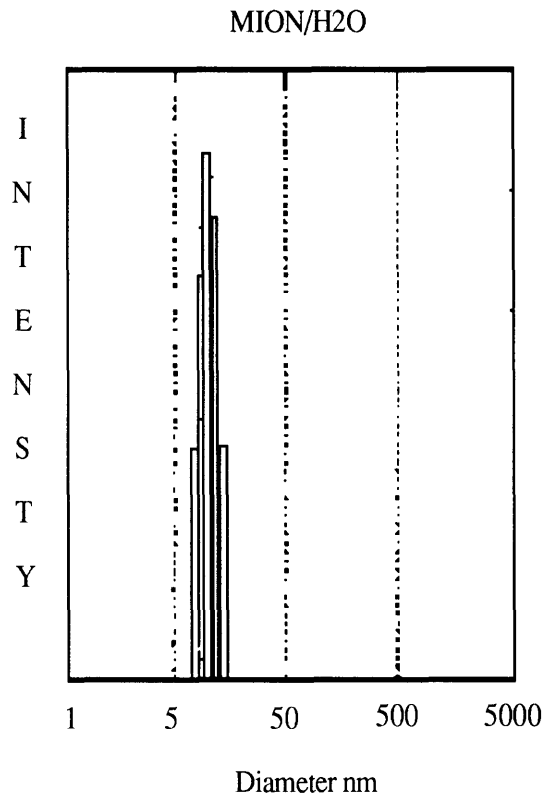
Laser light scattering (LLS) was performed to determine the overall size distribution of MION in aqueous media. In this case, photon correlation spectroscopy with multiple-angle scattering was used (Coulter Electronics, Inc., Model N4MD, Hialeah, FL). Figure 4.5 shows schematically the set-up of LLS experiments. A 4mW helium-neon 632nm laser was used as the light source. Scattering patterns at multiple angles were observed for each measurement. This technique allows instant determination of the particle size distribution in aqueous media.

Figure 4.6 shows the result of a typical LLS measurement of MION in aqueous solution. There is a unimodal distribution of colloidal MION, and the mean hydrodynamic diameter was determined to be  $15 \pm 3$  nm. This diameter is larger than that determined by TEM. The Brownian motion of the particles is a function of its hydrodynamic diameter. In the case of MION, the hydrodynamic diameter is that of the iron oxide core plus the thickness of the polymer coating, i.e. surface bound dextran.



**Figure 4.5** Schematics of laser light scattering equipment: a laser beam is directed to a sample chamber. A photon detector is set to collect the scattered light from the sample at multi angles from the laser source. Signals are then send to the autocorrelator and processed by computer. The frequency of the changes in the scattering signal are related to the brownian motion and hence to the hydrodynamic size of the particles.





**Figure 4.6** A typical LLS measurement of MION in aqueous solution. There was a unimodal distribution of colloidal MION, and the hydrodynamic diameter was determined to be  $15 \pm 3$  nm.

### **4.3 Magnetic Properties of the Core**

As discussed, the crystal structure, spin coupling conditions and size of a particle stand in close relation to the magnetic properties of a material. These magnetic properties manifest themselves in several ways. On a macroscopic scale there is the bulk response of a material to an external magnetic field, while on a microscopic scale there are the internal interactions of individual spins within the crystal lattice.

In the following studies, the bulk responses of solid MION samples were measured using a Superconducting Quantum Interference Device (SQUID) magnetometer. Mössbauer spectroscopy was then used to evaluate the interactions of Fe spins in the crystal lattice. Finally the relaxivities of MION were studied by NMR spectroscopy.

#### ***4.3.1 Superconducting Quantum Interference Device (SQUID)***

Measurements to determine the bulk magnetic susceptibility of MION samples were performed with a superconducting quantum interference device (SQUID). In this technique, samples are cycled between two coils which are located within a magnet. The magnetic moment of the sample can be calculated from the induced electrical current detected by the coils. Typical of superparamagnetic compounds is that the induced magnetization increases exponentially with increasing field strength, that there is no remnant magnetization at  $B_0 = 0$  T (no hysteresis), and that the induced magnetization increases with decreasing temperatures. In this experiments, the induced magnetization of MION was evaluated with a SHE SQUID magnetometer (SHE Corp. San Diego, CA figure 4.7). The MION samples were dried by lyophilization (Virtis Company, Inc.,

Gardiner, NY) prior to the experiment. A 0.08 cubic millimeter Teflon sample container, which holds 3 milligrams of MION powder, was used in the measurements.

The magnetization curve of MION obtained at fixed temperature of 310 K is shown in figure 4.9a, with external magnetic fields ranging from 0 to 50 KGauss (Tesla). The induced magnetization at 15 KGauss (field strength most commonly used for clinical imaging) is 68 emu per gram of iron. When the external field was removed (0 KGauss) there was no remnant magnetization. In addition, the temperature dependence of the induced magnetization was also evaluated at low field strength (Figure 4.9b). The field-cooled magnetization of MION at constant external magnetic field of 0.05 KG (Figure b) showed an abrupt increase of the magnetization as the temperature was decreased to 4 K. The critical temperature  $T_C$  is taken at the maximum  $dM/dT$  :  $T_C = 6 \pm 0.1$  K. At temperatures below  $T_C$ , the magnetization saturates to a constant value. This behavior is expected for superparamagnetic substances.

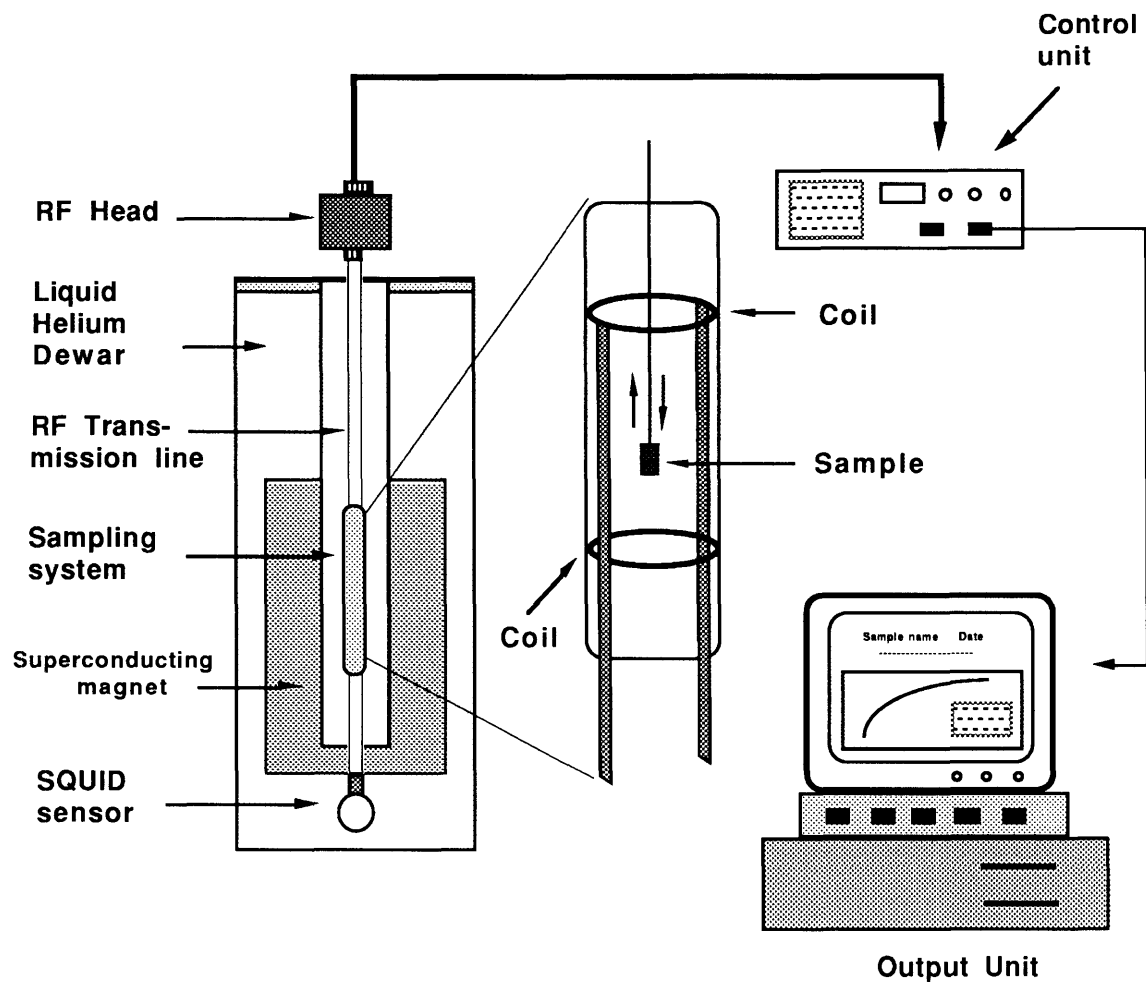
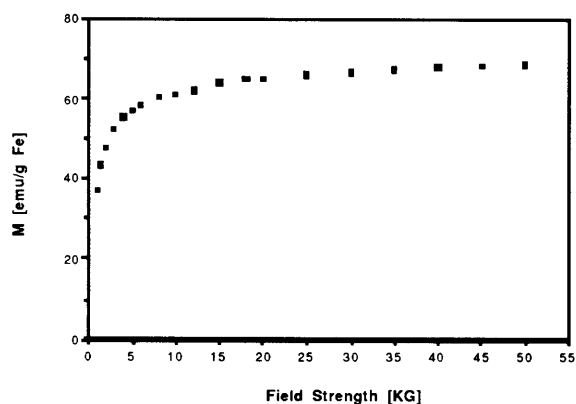
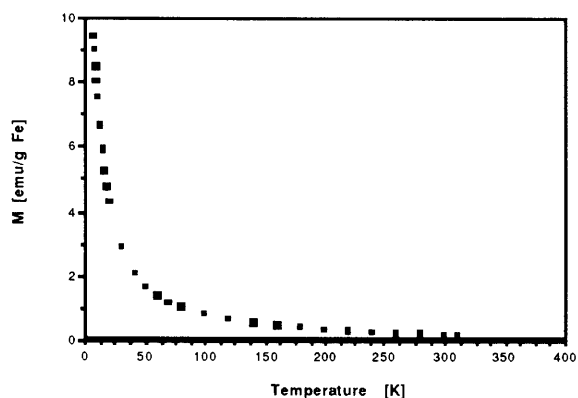


**Figure 4.7** Schematic representation of a typical Superconducting Quantum Interference Device (SQUID) for sensing external magnetic fields. The principal components are identified on the figure. The SQUID sensor and its associated input circuitry are operated at cryogenic temperatures. As illustrated in the figure, the necessary cryogenic environment is provided by immersing the SQUID and input circuitry directly in liquid helium which boils at 4.2 K under normal atmospheric pressure. A low thermal conductivity rf transmission line connects the SQUID sensor to the room temperature electronics, which consists of an rf head located at the helium drawer and a separate control unit where the output signal is obtained.



A



B

**Figure 4.8** Induced magnetization. The induced magnetization of MION (electromagnetic units [EMU]/g Fe) is plotted against the applied field strength (kG). **A.** There is an initial steep increase of magnetization at low field strengths. At 1.5 T the induced magnetization is 63.8 emu/g Fe (293 K). At higher field strengths induced magnetization increases to a lesser degree. Typical for all superparamagnetic iron oxides is the absence of sample magnetization when the field is removed (i.e. 0 T). **B.** The temperature dependence of the induced magnetization was further evaluated at a fixed field strength of  $5 \times 10^{-3}$  Tesla. There was an abrupt increase of the magnetization at a temperature of 4 K.

### **4.3.2 Mössbauer Spectroscopy**

Mössbauer spectroscopy was performed to determine the relaxation of individual spins within MION crystals. This method thus differs from the SQUID measurements which determine the magnetization of the bulk sample. Mössbauer spectroscopy is also capable of providing size estimates of crystals. Gamma-ray photons with frequencies of the order of  $10^{19}$  Hz and wavelengths of approximately 100 pm were used. The gamma-ray source is driven electromagnetically to and fro at a known speed, therefore the resonance matching the gamma-ray with the nuclear energy levels of the samples is achieved by Doppler shift. The shifts of resonance position and the splitting of resonance peaks are then recorded. Figure 4.10 schematically illustrates the set up of Mössbauer spectroscopy experiments.

In our experiment, Mössbauer spectroscopy was performed on a conventional constant acceleration zero-field variable temperature system (Lake Shore Cryotronic model DRC-70C). The spectrometer was equipped with "Supervaritemp" cryogenic dewars (Janis Research Corp.) and a temperature controller capable of maintaining sample temperatures in the range  $1.6 \leq T \leq 300$  K within 0.1K. The energy source used was a  $^{57}\text{Co}$  in Rh matrix maintained at room temperature. Standard peripheral electronics, pumping stations were used during data acquisition. The processing software on a Digital VAX740-VMS system was used for detailed Mössbauer spectral fitting and analysis.

The most important parameter that governs the magnetic behavior of small magnetically ordered particles of a given volume is their anisotropy energy constant  $K$ . The rate at which the saturation magnetization is reached with increasing applied magnetic field is sensitive to the value of  $K$ ; superparamagnetic relaxation phenomena associated with thermal excitation of the magnetization vector between equivalent easy axes of

magnetization also depend on K. The superparamagnetic relaxation time has an exponential dependence on the anisotropy constant K according to the following equation:

$$\tau_{\text{sup}} = \tau_0 e^{\frac{KV}{k_B T}} \quad (4.1)$$

where  $\tau_0$  is a temperature independent constant of the order of  $10^{-9}$  sec, V is the volume of the particle.  $k_B$  is Boltzmann's constant and T is the temperature.

The characteristic of superparamagnetic relaxation phenomena in the Mössbauer spectra is their gradual change from paramagnetically to magnetically split spectra (Figure 4.11) with decreasing temperature. For  $\tau_{\text{sup}} \ll \tau_L$ , paramagnetic spectra are obtained while for  $\tau_{\text{sup}} \gg \tau_L$  magnetically split spectra are observed. Here,  $\tau_L$  is the Larmor precession time of the iron nuclear spin in the internal magnetic field of the material.

Mössbauer spectroscopy was carried out on a freeze dried MION sample. The saturation internal magnetic field observed in the Mössbauer spectra of Figure 4.11 at low temperature was 505 KOe, which corresponds to a Larmor precession time  $\tau_L = 2.5 \times 10^{-8}$  sec for the  $^{57}\text{Fe}$  nuclear spin. The blocking temperature,  $T_B$ , at which equal intensities of paramagnetic and magnetically split component spectra were observed, was determined to be about 100 K. Electron microscopy indicated particle sizes 4.6 nm in diameter. The value of the anisotropy energy could therefore be determined by equating  $\tau_{\text{sup}}$  with  $\tau_L$ .

$$K = \frac{k_B T_B}{2V} \ln\left(\frac{\tau_L}{\tau_0}\right) \quad (4.2)$$

This yields an anisotropy energy  $K = 0.8 \times 10^6$  ergs/cm<sup>3</sup>, which is comparable to that determined by Morup et al. (Morup and Topsoe 1976) for 60 Å magnetite particles to be

$1.3 \times 10^6$  ergs/cm<sup>3</sup> (Haneda and Morrish 1977; Haneda and Morrish 1977; Haneda and Morrish 1977).

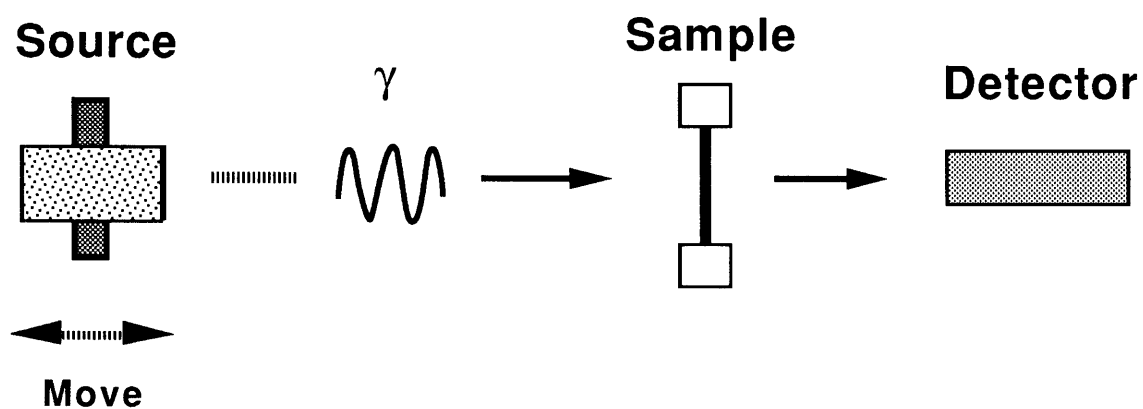


**Figure 4.9** Schematics of Mössbauer Experiment

The source is fixed to a diaphragm which can be moved electromagnetically to and fro at a known speed, and the Doppler shift is used to achieve resonance matching of the  $\gamma$ -ray frequency with the nuclear energy levels of the sample.



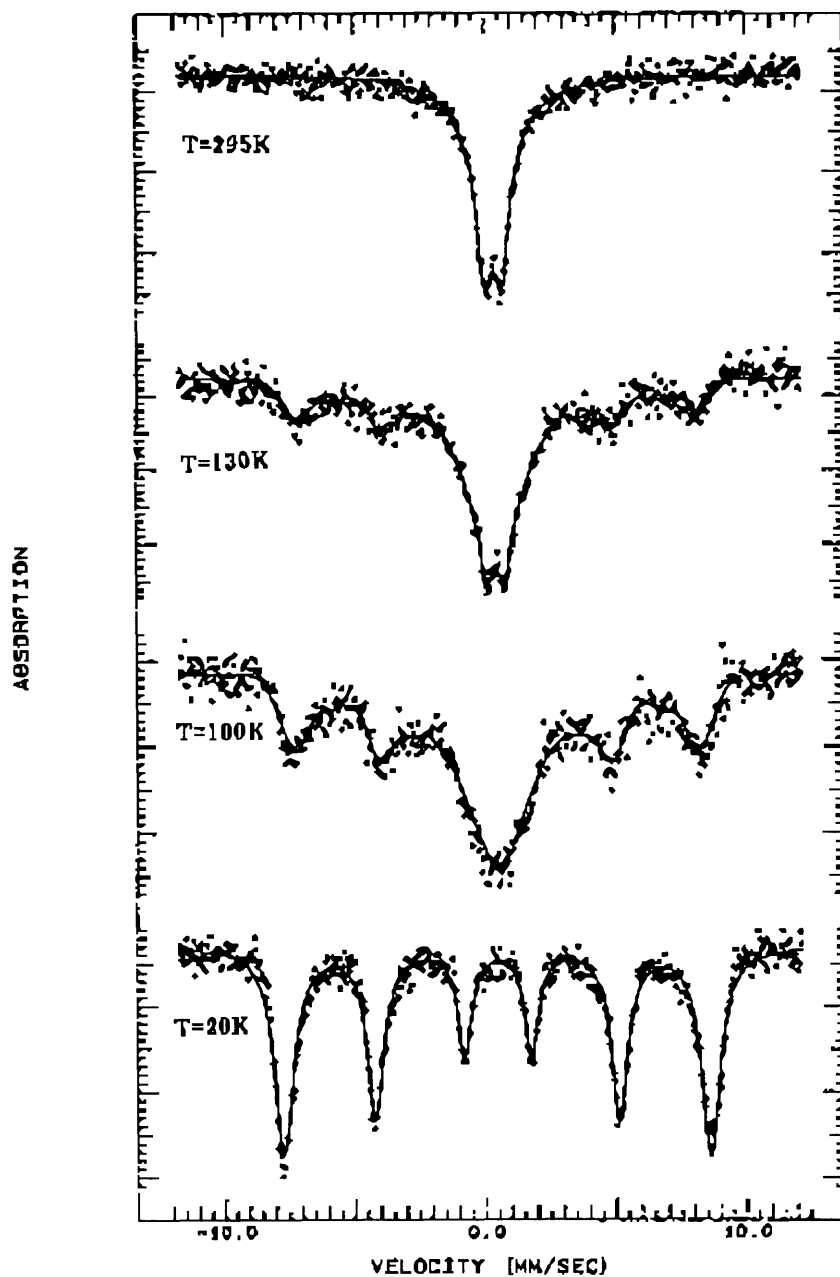


**Figure 4.10** Mössbauer spectra of MION-37 at various temperatures. The solid lines are fits to the data. At intermediate temperatures, a distribution of internal hyperfine fields was observed due to spin fluctuations. The spectra were strongly affected by superparamagnetic relaxation above 100 K. At 295 K, the magnetic splitting had collapsed completely.

### 4.3.3 NMR Relaxation Studies

The effect of the MION preparations on the T<sub>1</sub> and T<sub>2</sub> relaxation times of protons was measured with an IBM/Bruker PC minispec (Bruker Instruments, Canada) operating at a 0.47 Tesla field strength and at 37 °C. As described in chapter 2, the relaxivities are a good measure of the efficiency of MR contrast agents. Before each measurement was made, the spectrometer was tuned and calibrated. The pulse length for each experiment was not measured directly, rather a potentiometer with an arbitrary scale was used to adjust the pulse lengths while observing the FID on an oscilloscope. T<sub>1</sub> was measured from eight data points generated by an inversion-recovery pulse sequence. T<sub>2</sub> was measured from ten data points generated by a Carr-Purcell-Meiboom-Gill pulse sequence with a  $\tau$  of 1 msec. 10 echoes were collected for each cycle through the measurements. T<sub>2</sub> measurements were fit using a non-linear least square method assuming mono-exponential decay. Each measurement was repeated 3 times and individual results were averaged thereby yielding statistically meaningful measurements. Inverse relaxation times were then plotted against the iron concentration (Figure 4.12). The slope of these curves represents the relaxivity and is expressed in (mM•sec)<sup>-1</sup> or (mmol/L•sec)<sup>-1</sup>.

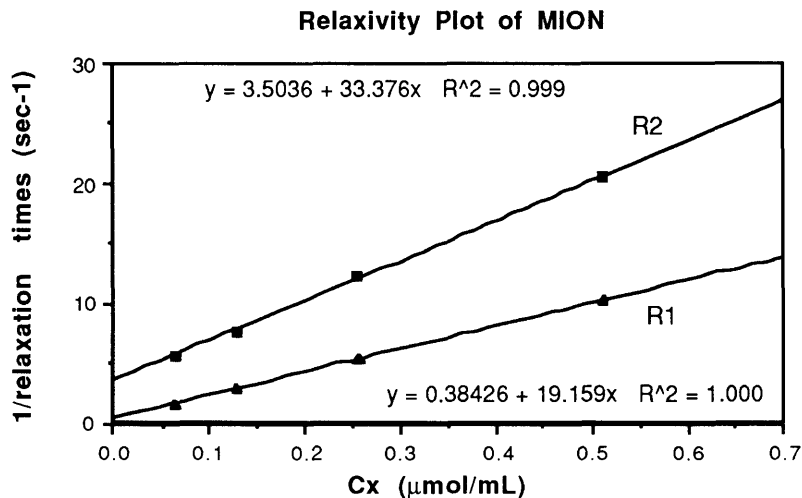


**Figure 4.11** A Typical relaxivity plot of MION

#### **4.4 Chemical Composition**

It has been reported that the amount of surface bound dextran of MION alters the agents biodistribution and its ability to interact with plasma proteins (Bogdanov, Papisov et al. 1992). Therefore it is important to determine and control the amount of dextran that binds to the surface.

Spectrophotometry was used to determine the iron and dextran content of highly purified MION. A DMS100 spectrophotometer (Varian Instrument Group, Sugar land, TX) was used to measure both iron and dextran concentrations (phenol/sulfuric acid method) (Dubois, Gilles et al. 1956). In this study, measurements were made at 410nm and 485 nm to determine the concentrations of iron and dextran respectively in MION samples.

Each sample for spectrophotometry study was prepared as follows: 25  $\mu$ l phenol reagent (80% by weight) was added to 1 ml of sample solution in a test tube, followed by rapid addition of 2.5 ml sulfuric acid (reagent grade 95.5%). The mixture was then allowed to cool to room temperature prior to each measurement. The dextran-phenol complex showed an absorption maximum at 485 nm. A series of standard Dextran T10 samples (concentration range: 10-200  $\mu$ g/ml) were prepared to generate a calibration curve at 485 nm. The same procedures were repeated for diluted MION samples. The concentration of dextran in each MION sample was then calculated from the calibration curve (Appendix B). The iron concentration of each sample was measured at 410nm using the HCl/peroxide method.

Two preparations of MION (37 and 46) with similar core size (approximately 5 nm) were examined. These two preparations were synthesized with different initial Dextran concentrations. Assuming that the magnetic core of the MION has an inverse spinel

structure, and a 5 nm core contains approximately 2400 iron atoms. The iron percentage (by weight) was then calculated. This result was then compared with elemental analysis performed by Galbraith Laboratories, Inc. (Knoxville, TN). The following table summarizes the results:

**Table 4.2 Chemical composition of two MION preparations**

	MION-37 (core size of 5 nm)	MION-46 (core size of 5 nm)
[Iron]	1.85 $\mu\text{mol/ml}$ (0.103 mg/ml )	0.944 $\mu\text{mol/ml}$ (0.053 mg/ml )
[Dextran]	0.008 $\mu\text{mol/ml}$ (80 $\mu\text{g/ml}$ )	0.0118 $\mu\text{mol/ml}$ (118 $\mu\text{g/ml}$ )
iron/dextran ratio	$\approx 230$	$\approx 80$
number of dextran per MION core	$\approx 10$	$\approx 30$
iron% (calculated)	46.7%	27%
iron% (elemental analysis)	48%	17%

Based on the available experimental data, a molecular model of MION was generated using a computer aided Chemistry program (CACHe, Tektronix, Inc.) to visualize the MION with surface bound dextran. This program allows construction of crystal structure and polymeric molecules and it performs calculations of energy minimization for a given secondary structure. Figure 4.13 shows the result of the MION model.

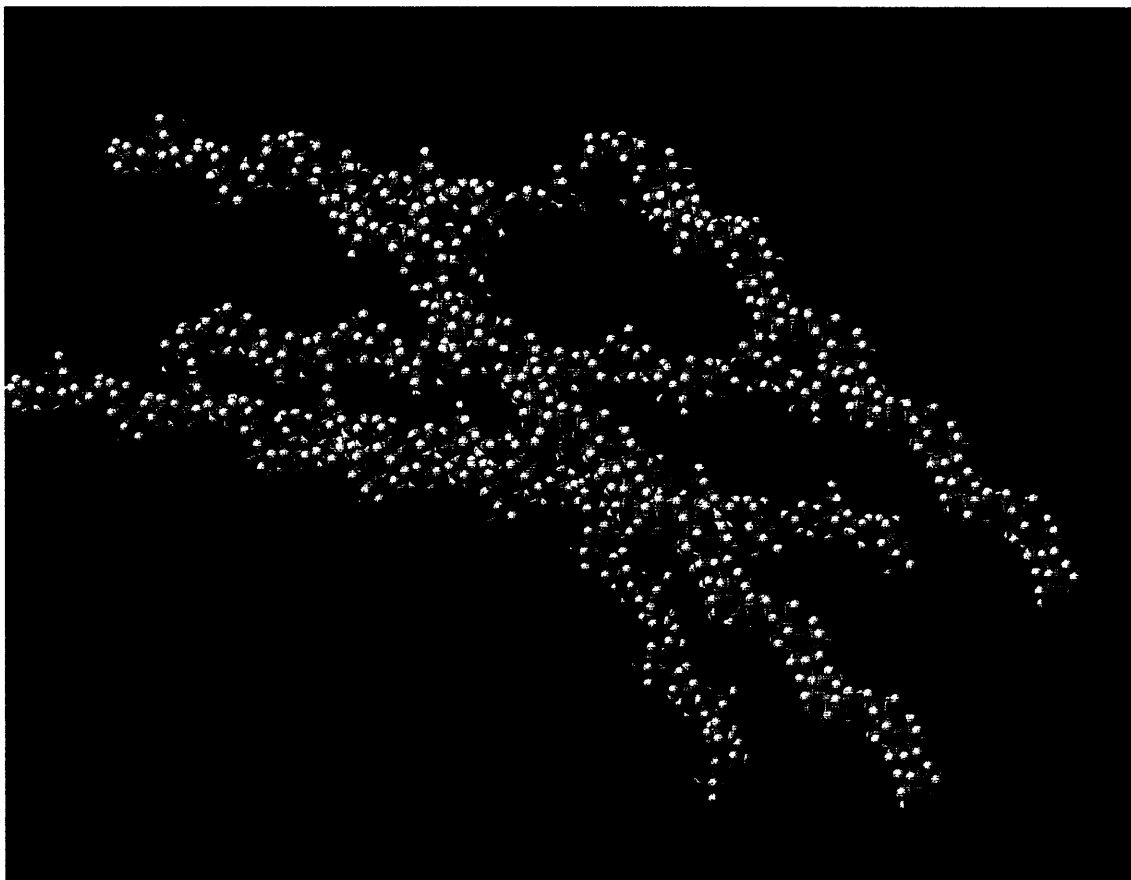


**Figure 4.12** Molecular model of a monocrystalline iron oxide nanocompound. Electron microscopy and electron diffraction studies indicate that the inner core of MION consists of an inverse spinel packing of oxygen atoms (red), and divalent and trivalent iron (green). Assuming a mean diameter of 4.6 nm, the average core would contain 2064 iron atoms. Each core contains a mean of 25 surface bound dextran molecules resulting in a schematic representation as shown in this figure (only 15 dextran molecules are depicted to show the central iron oxide core).

## **4.5 Summary**

In this chapter, we have evaluated the physicochemical properties of MION as a universal label for targetable MR imaging. MION is chemically well defined, highly pure, stable colloidal solution of dextran and magnetite single crystals with a molecular weight less than 300 kD. This compound is thus different from polydisperse iron oxide aggregates previously used for MR imaging. The magnetic properties of MION are typical of superparamagnetic compounds at room temperature.

The results indicate the feasibility of the synthesis of a well characterized iron oxide solution in which individual crystals are in the nanometer size range and still exhibit high magnetic susceptibility. MION has a magnetite central core with an average diameter of  $4.6 \pm 1.2$  nm, and an average hydrodynamic radius of  $20 \pm 5$  nm. The relaxivities of MION change dramatically with the central core structure, however, variation of surface polymeric coating has little effect on the relaxivities.

The amount of surface-bound dextran content can be varied with a given core size, and their opsonization properties will be evaluated in the following chapter.

## **Chapter V**

# **Biological Interactions**

The characterization of the physicochemical properties of MION with various techniques has been described in the previous chapter. The results from these studies indicate that MION has potent magnetic properties for use as a MR contrast agent.

In this chapter, experiments were performed to evaluate the interactions of MION with various biological components. First, the cellular response to these agents was evaluated in a model system of rat hepatocyte culture. Second, the interactions of MION with various blood components were studied by ultracentrifugation. Finally, the blood half-life of MION with various surface coatings was studied in rats.

### **5.1 Cellular Toxicity**

Hepatocyte culture was chosen as a model system for the evaluation of toxicity of MION. Upon the administration of MION, the response of cellular physiology can be monitored by the albumin secretion rate, one of the most sensitive indicators of cellular functions of hepatocytes.

#### ***5.1.1 Preparation of Hepatocyte Culture***

Hepatocytes were isolated from 2-month-old female Lewis rats by a modified procedure of Seglen (Seglen 1976). Briefly, the animals were anesthetized with ether, the liver, weighing approximately 8 grams, was perfused with 300 ml of calcium free Krebs Ringer

bicarbonate buffer, containing 5.5 mM glucose and 20 mM HEPES, pH 7.4, at a rate of 50 ml/min. The perfusate was maintained at 37° C and equilibrated with 95% O<sub>2</sub> and 5% CO<sub>2</sub>. The liver was subsequently perfused with a 0.05% collagenase (Type IV, Sigma, St. Louis, Mo.) solution containing 5 mM Ca<sup>2+</sup> for 10 minutes in a recirculating circuit. The resulting cell suspension was filtered through two nylon meshes with grid size of 250 and 62 µm. The cell pellet was collected by centrifugation at 50g for 5 minutes. Cells were further purified by a modified procedure of Kreamer et al (Kreamer, Staecker et al. 1986). The cell pellet was re-suspended to 50 ml, and 12.5 ml of cell suspension was added to 10.8 ml of Percoll and 1.2 ml of 10 x concentrated Dulbecco's modified Eagle medium (DMEM, 4.5 g/liter glucose). The mixture was centrifuged at 500 g for 5 min, and the cell pellet was washed with DMEM.

Type I collagen was prepared from rat tail tendon by a modified procedure of Elsdale and Bard (Elsdale and Bard 1972). Four tendons were dissected from each rat tail and stirred into 200 ml of 3% acetic acid overnight at 4 °C. The solution was filtered through four layers of cheesecloth and centrifuged at 12,000 g for 2 hours. The supernatant was precipitated with 40 ml of 30% NaCl. and the pellet was collected by centrifugation at 4000 g for 30 min. After two rinsing with 5% NaCl and 0.6% acetic acid, the pellet was dissolved in 50 ml of 0.6% acetic acid. The solution was dialyzed against 5 x 500 ml of 1 mM HCl and sterilized by evaporating 0.15 ml of chloroform through the solution. A 5-ml aliquot was lyophilized and weighed to determine the concentration.

Hepatocytes were cultured on gelled rat tail tendon collagen. Plates were prepared by distributing 1 ml of collagen gel solution evenly over a 60 mm tissue culture dish one hour prior use. Two million viable cells were seeded in 4 ml of complete medium, consisting of DMEM, supplemented with 10% fetal bovine serum, 0.5 U/ml insulin, 0.007 µg/ml glucagon, 0.02 µg/ml epidermal growth factor, 7.5 µg/ml hydrocortison, 200 U/ml



penicillin, and 200 µg/ml streptomycin. The second layer of collagen gel was spread over the cells after one day of incubation with 5% CO<sub>2</sub>. Thirty minutes were allowed for gelation and attachment before the medium was for gelation and attachment before the medium was replaced. The culture medium was changed daily. The in vitro hepatocyte culture was provided by the department of surgical research at Massachusetts General hospital.

### ***5.1.2 Enzyme-linked Immunosorbent Assay (ELISA)***

The collected media samples were analyzed for the rat albumin content by enzyme-linked immunosorbent assay (ELISA). Chromatographically purified albumin was purchased from Cappel (Cochranville, Pennsylvania). Antibodies to albumin were purchased from Cappel. The 96-well plates (NUNC-Immuno plate, Maxisorp, Newbury Park, California) were coated with 100 µl of 50 µg/ml rat albumin in 25 mM carbonate buffer, pH 9.6, overnight at 4 °C. The wells were washed four times with PBS plus 0.5% (v/v) Tween 20 (PBS-Tween). Fifty microliters of sample was mixed with an equal volume of antibody (800 ng/ml in PBS-Tween) before it was transferred to the wells. After overnight incubation at 4 °C, the wells were washed four times with PBS-Tween and were developed with 100 µl of 25 mM citrate and 50 mM phosphate, pH 5, plus 0.4 mg/ml o-phenylenediamine and 0,012% (v/v) hydrogen peroxide at room temperature. The reaction was stopped with 50 µl of 8 N sulfuric acid after seven minutes of incubation. The presence of bound antibodies was detected by conversion of o-phenylenediamine by conjugated peroxidase. The absorbance was measured at 490 nm with the Dynatech MR600 microplate reader (Chantilly, Virginia). Positive controls included known concentrations of purified rat albumin, transferrin, and fibrinogen added to culture medium, and negative controls included the culture medium and PBS-Tween. Concentrations of standards were calibrated by their absorbance at 280 nm, using 0.6 as extinction coefficient

for 1 mg/ml solution of albumin. Concentrations of samples were determined from a standard curve generated for each ELISA plate. Absolute rates of secretion were calculated from the concentration by multiplying the total volume of the medium (plus the volume of the collagen gel only on the day when it was introduced to the culture) and dividing by the elapsed time. Results for each sample, and replicate cultures agreed within 10% of each other (Dunn, Yarmush et al. 1989; Dunn, Tomkins et al. 1991; Dunn, Tomkins et al. 1991).

### ***5.1.3 MION Incubation:***

Two groups of hepatocyte dishes were incubated with MION and MION-ASF respectively. Two dishes in each group were used as controls, the rest was incubated with 100 and 200  $\mu\text{mol/dish}$  concentrations of MION. These concentrations are  $10^5$  times that of required clinical dosage. The cells were viable for two weeks during which the culture medium was changed daily. The albumin secretion rates were evaluated by analyzing the amount of albumin by ELISA techniques described above.

Results from the study are shown in Figure 5.1, depicting the albumin secretion rate of hepatocytes in the cell culture versus the time (in days) after incubation with MION and MION-ASF. The gradual increase in albumin secretion rate is typical for newly isolated rat hepatocytes in a double sandwiched gel, indicating the recovery of cell function after isolation (Dunn, Tomkins et al. 1991). Even at the high MION concentrations ( $10^5$  times clinical dosage) used, the effect of MION on the albumin secretion rate of the hepatocytes is statistically insignificant. Similar results were obtained with MION-ASF.

Based upon this experiment, it is expected that MION can be used at the clinical dosage without any measurable toxic effects to the liver.

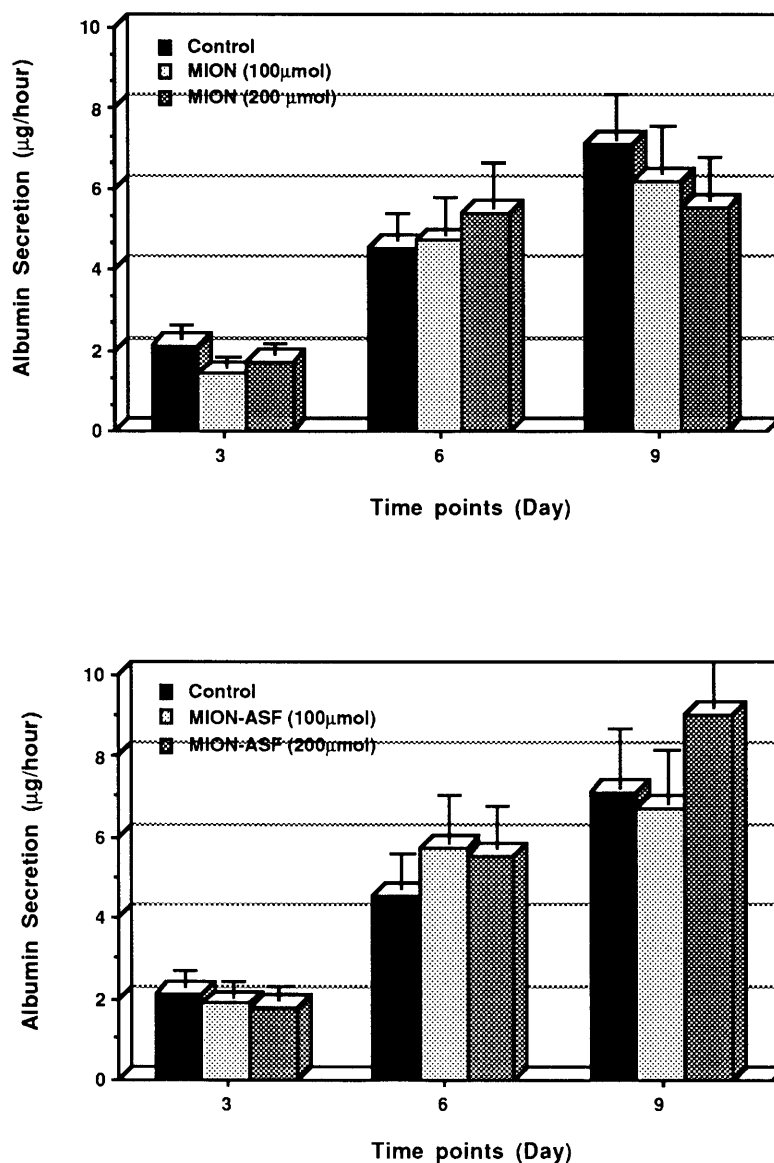


**Figure 5.1** The albumin secretion rate of hepatocytes in the cell culture as a function of time (in days) after incubation with MION and MION-ASF. The gradual increase in albumin secretion rate is typical for newly isolated rat hepatocytes in a double sandwiched gel, indicating the recovery of cell function after isolation. Even at the high MION concentrations ( $10^5$  times clinical dosage) used, the effect of MION on the albumin secretion rate of the hepatocytes is statistically insignificant.

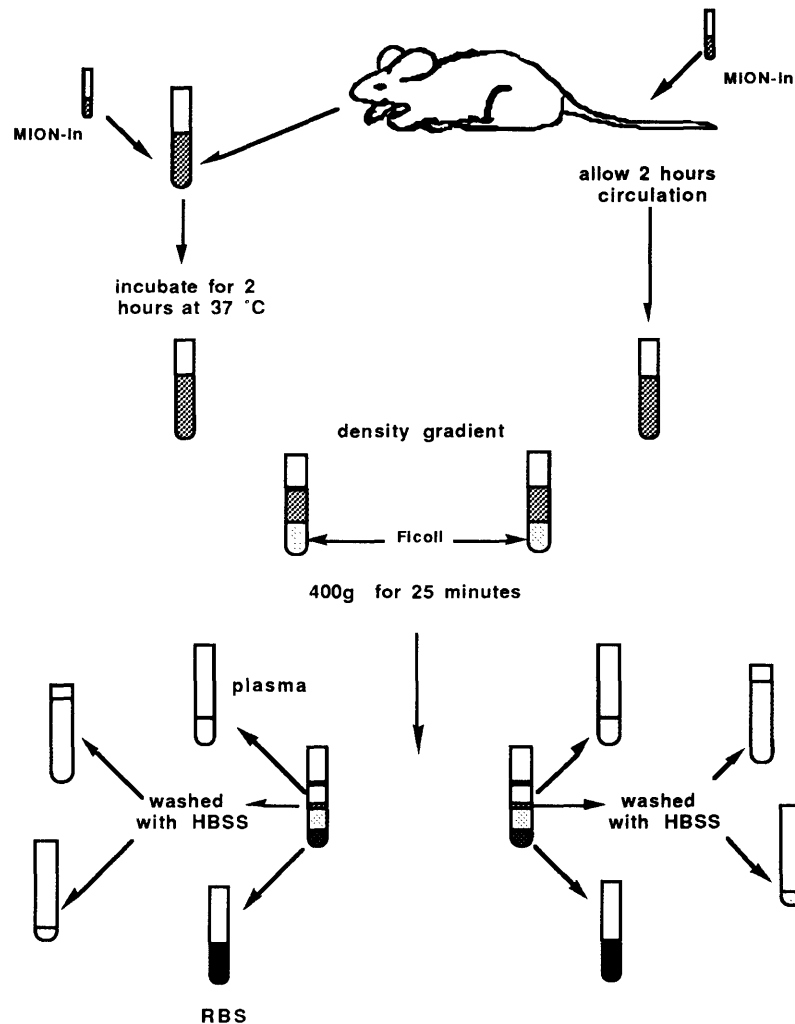
## **5.2 Interaction with Blood Components**

The *in vivo* behavior of a "foreign" object is influenced by its association with blood components. Association with blood components makes such objects more easily recognizable, resulting the enhanced removal from circulation. The purpose of the experiment was to determine to what extent MION binds to blood components after intravenous administration.

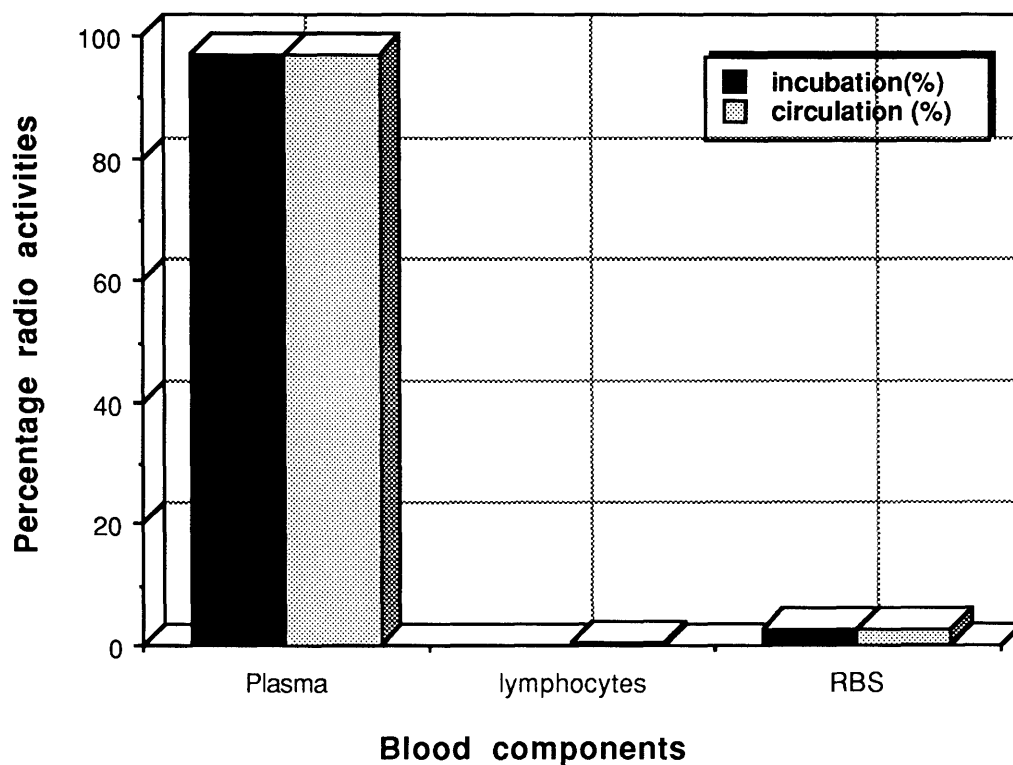
In this set of experiments MION with a radio labeled ( $^{111}\text{In}$ ) core (MION-In) was used. The procedure of the experiment is shown in Figure 5.2.  $^{111}\text{In}$  core-labeled MION (approximately 100-200 ng) was incubated for two hours with 1 ml of fresh drawn citrated whole rat blood. Following the withdrawal of blood,  $^{111}\text{In}$  core-labeled MION was injected intravenously into the rat. After two hours 1 ml of the rat blood was drawn from the *in vivo* circulation. Ficoll-metrizoate density gradients were used to fractionate the whole blood (both from *in vitro* and *in vivo* experiments) into plasma, leukocyte and erythrocyte fractions. The radioactivities of these fractions were counted using a high efficiency gamma counter (Hewlett Packard Auto-Gamma Scintillation Spectrometer, Hewlett Packard Instruments, Chicago, IL).

Figure 5.3 shows the radioactivity of each blood component obtained from *in vitro* incubation and *in vivo* circulation. After incubation of MION with whole blood, 96.5-98% of MION was found in the plasma fraction, while the cell-associated MION (1.7-2.8%) was found predominantly in the erythrocyte fraction. Similar results were obtained from the blood sample when MION was injected intravenously, although it has to be recognized that the radioactivity in the rat blood decreased over the course of the experiment, due to the removal of some of the MION-In from the circulation. During the two hours incubation, no significant amount of MION was associated with the leukocyte and erythrocyte

fractions, suggesting that MION did not bind to the leukocyte and erythrocyte significantly during the course of a typical patient examination in the clinical setting.



**Figure 5.2** Experimental set-up for evaluating the interactions of MION with blood components:  $^{111}\text{In}$  core-labeled MION (approximately 100-200 ng) was incubated for two hours with 1 ml of fresh drawn citrated whole rat blood. Simultaneously,  $^{111}\text{In}$  core-labeled MION was injected intravenously in a rat. 1 ml of the whole rat blood was drawn after two hours in vivo circulation. Ficoll-metrizoate density gradients were used to fractionate the whole blood into plasma, leukocyte and erythrocyte fractions. The radioactivities of these fractions were counted using a high efficiency gamma counter.



**Figure 5.3** Percentage radioactivity of MION associated with different components of whole rat blood. After incubation of MION with whole blood, 96.5-98% of MION were found in plasma fraction, where cell-associated MION (1.7-2.8%) were found predominantly in erythrocyte fraction. Similar results were obtained from the blood sample when MION was injected intravenously.

### 5.3 Blood half-lives of MION

Blood half-life is an important biological property, and it can be used to evaluate the targetability of MR contrast agents. If the blood half-lives of the contrast agents are short,

the chances of delivering the agents to the target sites are small. Therefore, a efficiently long blood half-lives are desirable. Blood half-lives of MION with various surface coatings were measured in Sprague-Dawley rats (n = 5 per compound). The anesthesia was induced by Katamine, xylasine and Acepromocine (check spelling) at dosages of 50, 5, 2.5 mg/kg body weight respectively, and was maintained with half of the induction dose every 45 minutes for six hours. A 19-Gage catheter was inserted to the right femoral artery for the blood sampling and one to the right femoral vein for intravenous administration of contrast agents. Blood samples were drawn before the administration of contrast agents (as controls) and at multiple time points after the intravenous injection. The relaxation times of the blood samples were measured and averaged over 5 animals tested for each preparation.

T<sub>2</sub> varies linearly with the MION concentration in the blood sample, so that the concentration of MION in the blood at each point in time could be calculated from its T<sub>2</sub> relaxation time. Thus, the percentage of initial concentration in the rat blood was plotted as a function of time. Figure 5.4 shows a typical exponential decay of unlabeled MION, from which its blood half-life was calculated. Intravenously injected unlabeled MION has a blood half-life of 45 ± 5 minutes in rats. Table 5.1 summarizes the blood half-lives of MION coated with different polysaccharide surfaces. The unlabeled MION (Dextran coated) has the longest blood half-life among the various polysaccharide-coated MION preparations. This is expected because the polysaccharide-coatings were specifically selected to target the galactose receptors on the liver cells, whereas unlabeled MION was designed to be “invisible” to the immune system and the phagocytic macrophages in liver and spleen, and non-specific to the receptor system mentioned above.

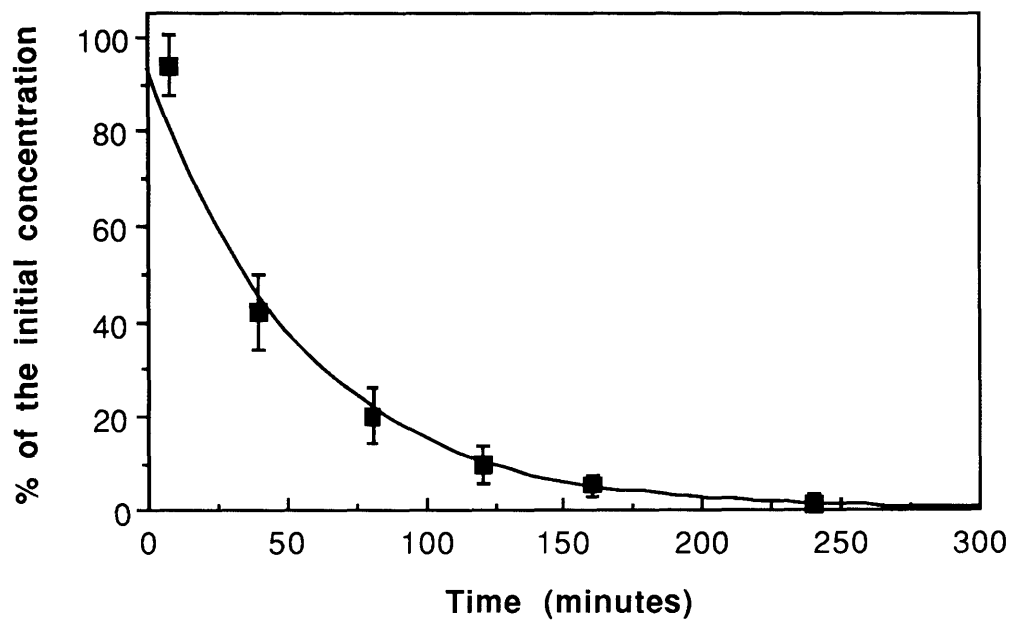


**Figure 5.4** A typical blood half-life plot of an unlabeled MION in rats. The fraction of initial concentration of MION in the blood is plotted as a function of time. The decay follows an exponential function from which the blood half-life was calculated.

**Table 5.1 Blood half-lives of MION samples**

MION-surface coating	Blood half-lives (minutes)
MION (unlabeled)	$45 \pm 5$
MION-Mannan	$25 \pm 5$
MION-Chitosan	$5 \pm 3$
MION-Fucoidan	$15 \pm 5$
MION-Arabinogalactan	$10 \pm 3$



## Chapter VI

# In vivo MR Imaging

In the previous chapters, physicochemical properties (especially the relaxivities) of MION samples were evaluated in aqueous solution. In this chapter, the feasibility of MION as receptor or immuno-specific contrast agents *in vivo* was studied by MR imaging. This is the ultimate test in the development of MR contrast agents. These experiments can provide evidence of the applicability of MION agents in future clinical diagnosis.

### 6.1 Conventional MR Imaging

#### 6.1.1 Animal Preparation

Sprague-Dawley rats (500-700 g body-weight, Charles River Laboratories, Wilmington, MA; ) were used as the animal model for *in vivo* experiments. The anesthesia was induced by Katamine, xylasine and Acepromocine (check spelling) at 50, 5, 2.5 mg/kg dosage respectively, and was maintained with half of the induction dose every 45 minutes. A 19-Gage catheter was inserted to the right vein for intravenous administration of contrast agents.

#### 6.1.2 Imaging Experiment

Pulse sequences used in the MR imaging experiments were optimized on a 1.5 T Signa (GE, Milwaukee, WI) system, where MR imaging was performed. Animals were placed supine in a standard GE knee coil. Spin echo (SE) images were obtained at SE 2000/30

(TR/TE) as control images before administration of the contrast agents. One hour after intravenous injection of unlabeled MION or other polysaccharides coated MION preparations (10  $\mu\text{mol/kg}$  body-weight), a series of coronal images was acquired using the same imaging techniques. Signal changes in the liver were recorded with an automatic region-of-interest program implemented on the imaging system. Figure 6.1 shows typical MR images obtained before and after (pre and post) the administration of unlabeled MION. Note the decrease in signal intensity of the liver region.

The contrast enhancement by polysaccharides coated MION were compared to unlabeled MION and saline injections with respect to their ability to reduce liver signal intensity. Following intravenous administration of 10  $\mu\text{mol/kg}$  body-weight of various contrast agents, liver signal intensities decreased noticeably. The following table summarizes the relative changes in liver signal intensity from SE 2000/30 images.

**Table 6.1**

<b>Relative signal intensity change</b>	
<b>Compound</b>	<b>Liver SI change (%)</b>
MION (unlabeled)	-14
MION-Mannan	-27
MION-Chitosan	-20
MION-Fucoidan	-15
MION-Arabinogalactan	-37

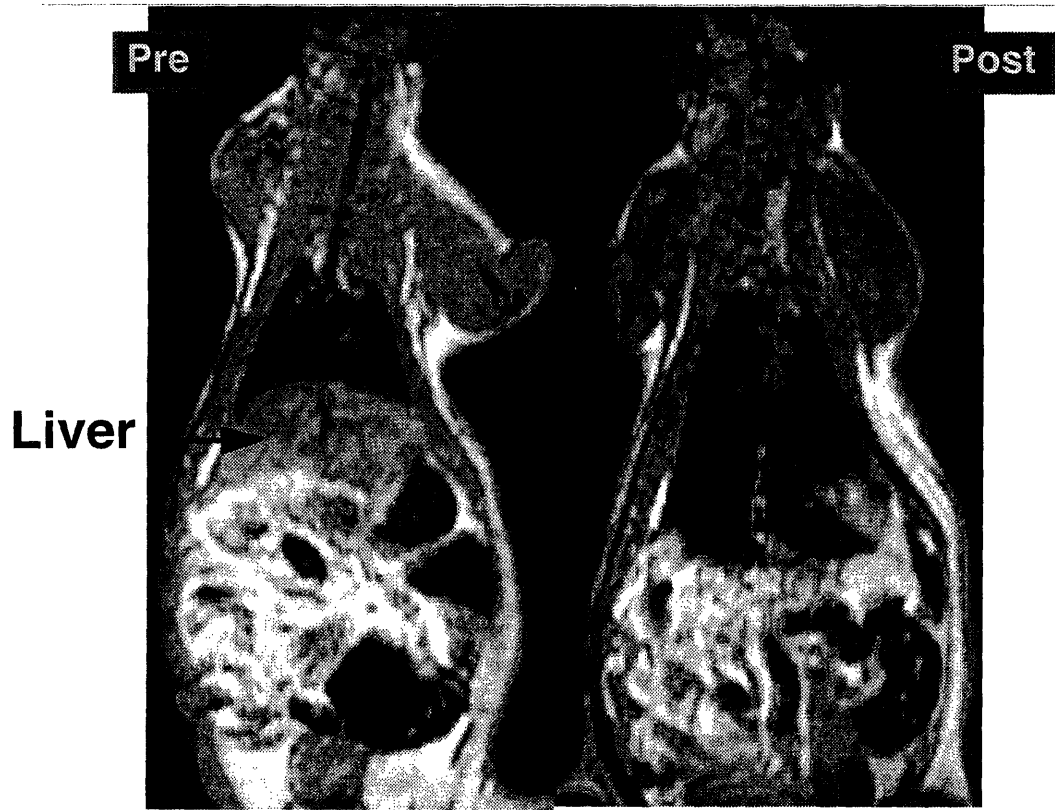


**Figure 6.1** Coronal MR images (SE 2000/30) of a rat obtained before and after administration of unlabeled MION (pre and post). The injection dosage was 10  $\mu\text{mol/kg}$  body-weight. Note the localization of the agent in the liver region shown as general reduction of signal intensity of the liver. This is a typical example of contrast enhancement by MION as a T2 agent, also regarded as a negative agent.

## 6.2 Fast *in vivo* MR Imaging of MION and MION-ASF

Fast imaging techniques (i.e., images acquired in a few seconds or less) can be useful in reducing number of artifacts associated with many types of physiologic motion such as respiratory and cardiac motion. In addition, fast MR techniques have the potential for imaging dynamic processes. Echo planar imaging (EPI) is significantly different from standard MR imaging methods in which one phase-encoding step is applied after each rf excitation. With 2DFT methods, only one projection is acquired with each TR interval, so that the image acquisition time is relatively lengthy (Kantor, 1990). In contrast, the EPI method acquires all projections needed to create an image after a single RF excitation. This is accomplished by rapidly oscillating the frequency-encoding gradient during the envelope of a spin-echo signal. First, as in a 2DFT SE sequence, a spin echo is produced by application of a 90° and 180° RF pulse, with the echo peaking at the echo time. However, rather than applying a single phase-encoding gradient and a constant frequency-encoding gradient, the frequency-encoding gradient is rapidly oscillated during the build-up and decay of the spin-echo. A series of gradient echoes are thereby produced, each of which is separately phase-encoded by application of a very brief phase-encoding gradient pulse. Because all of the data are acquired after a single RF pulse, the  $T_R$  is nearly infinite. As a result, the images are free from  $T_1$  weighting and can be strongly  $T_2$  weighted, with the degree of  $T_2$  weighting dependent on the value of  $T_E$ . Therefore  $T_2$  contrast agents (MION) are particularly well suited for use with EPI.

The pharmacokinetics of MION and MION-asialofetuin were assessed *in vivo* using echo planar imaging. With an acquisition time of 40 msec, multiple coronal images can be obtained displaying organs of interest (liver, spleen, kidneys, muscle, brain). Measurements of liver signal intensities were obtained, and plotted as a function of time after administration of MION and MION-ASF. Because MION and MION-ASF have

identical magnetic core properties and relaxivities, it can be concluded that more MION-ASF was directed to the liver than the unlabeled MION. The MR signal intensity decay rate caused by MION-ASF indicates the rapid uptake of the agent by the liver. In the case of unlabeled MION, on the other hand, the MR signal intensity decays rapidly immediately after intravenous administration, and then decreases gradually over the sampling period of 30 minutes. These findings are further evidence for the directability of the modified MION.

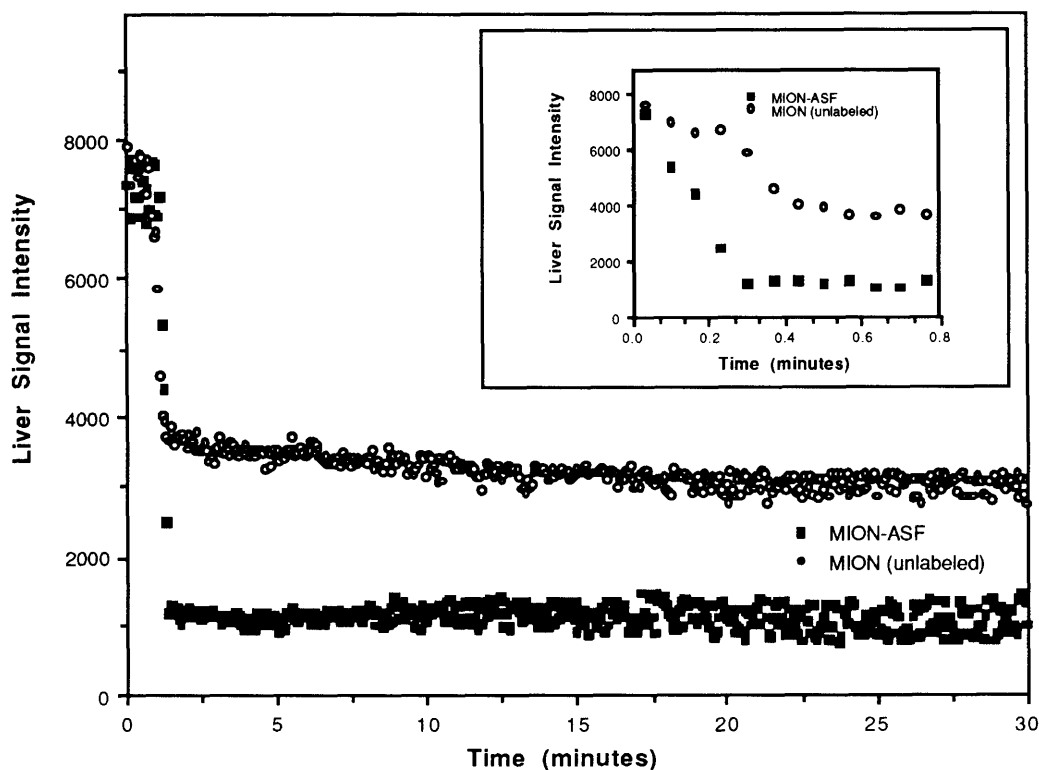


**Figure 6.2** Liver signal intensity decreased significantly after administration of equal dosage ( $10 \mu\text{mol Fe/kg}$ ) of MION and MION-ASF. Because MION and MION-ASF have identical magnetic core properties and relaxivities, it can be concluded that more MION-ASF was directed to the liver than the unlabeled MION.

## Chapter VII

# Discussion and Future Directions

The work presented in this thesis is the development of a new class of MR contrast agents for receptor- and immuno-specific imaging. The results have shown the importance and feasibility of synthesizing chemically well defined superparamagnetic compounds that can be used as universal labels in MR contrast agents. Furthermore, the targeting of such a magnetic label to selected tissues by attaching specific carrier molecules has been successfully demonstrated.

Paramagnetic ions, (e.g. Gd, Mn) can be used as T<sub>1</sub> labels for target specific MR imaging if the ions are chelated via DTPA. Gd-DTPA is thus far the only FDA approved MR contrast agent for use in clinical practice. Gd has a high toxicity when detached from DTPA although in order to achieve measurable contrast enhancement in MR imaging, a high dosage is required. Commercially available iron oxide based contrast agents have previously been suggested for MR imaging, but those aggregates too large in size to be used as a universal label, since target specific delivery requires a well defined label with a size small enough to pass through the capillary endothelium. The smaller the size of the label, and the better shielded from recognition, the higher its probability of successful delivery to the targets. In order to retain a high magnetic susceptibility at this small size (nm range), a well defined chemical composition and crystal structure are required.

Through a systematic investigation of the factors which affect core structure, size and stability of iron oxide particles synthesized in aqueous solution, monocrystalline iron oxide nanocompound (MION) was designed and optimized as a universal label for target specific MR imaging. The reaction conditions including the initial ratio of Fe(II) and Fe (III) and

reaction temperature were optimized to ensure the formation of magnetite for the MION core with an average size in the nanometer range. The stability of a colloidal solution of MION was optimized by using Dextran polymers in the initial reaction mixture. In addition, Other polysaccharides and proteins were successfully conjugated to MION by covalent and non-covalent attachments for target specific delivery. Changes in surface coating showed little influence on the magnetic properties of MION.

X-ray powder diffraction analyses indicated that MION consists of a central magnetite-like core. Electron diffraction patterns obtained from HRTEM investigation confirmed that each MION central core was a single crystal. Colorimetric analysis for glucose revealed that there were approximately 20-30 dextran molecules attached to the surface of a 5 nm MION core. The dextran rod-like molecules are non-flexible, increasing the overall size from 5 nm to 20 nm in aqueous solution. This concept was used for antibody binding without chemical alterations of the conjugates. Preferable MION preparations for targeting purposes however, were shown to have maximum number of dextran molecules per iron oxide core to shield it from strong interaction with plasma proteins.

Monocrystalline iron oxide studied exhibited a strong induced magnetization at clinical field strengths (68 emu/g Fe at 1.5 T). The individual spins within the iron oxide crystals followed the superparamagnetic theory with hyperfine splitting of 505 KOe. The induced magnetization is a direct result of the structure of the iron oxide core and the its size. The current results and those of a previous study seem to indicate that the size and chemical structure of the iron core is the major determinant for the magnetic effect of the stabilized iron oxide complex. Surface modification has little or no effect on the relaxivities of MION preparations (Shen, Weissleder et al. 1991).

In order to be approved for clinical application, MION has to be shown safe in use. Therefore, the first steps have been taken is evaluate the biological interactions of MION with a variety of biological systems. The response of in vitro hepatocytes to the incubation with high concentrations of MION did not show statistically significant changes in the normal cell functions. To minimize the recognition of MION by the immune-system, the Dextran content of MION was optimized. This also improved the stability of MION colloidal solution. The MION can be lyophilized when need to be stored for longer period of time, and can be easily redissolved in a physiological buffer. This make the future storage and preparation in a clinical environment convenient. By changing the surface polymeric coatings of MION, the blood half-lives and in vivo destination could be altered. In vivo MR imaging experiments have shown that the use of MION at a dosage more than 1000 or  $10^6$  times (taking iron particles and atoms as a unit respectively) lower than that of iodinated radiographic contrast agents, can result in a factor of four decrease in the signal intensity of the liver. In addition, iron is a non-foreign element to the human body: one 10  $\mu\text{mol/kg}$  dosage is equivalent to a few days of iron intake for an average person.

In summary, prototypic monocrystalline iron oxide compounds have been characterized by physicochemical methods. Although several preparations have been used, the results indicate that the magnetic core is solely responsible for the efficiency of MR contrast enhancement of the targeted complexes, irrespective of surface attachments. Surface attached macromolecules on the other hand have been shown to be largely responsible for the biological properties of the compounds.

The research field for MR contrast agents is rapidly expanding. A 1990 survey found that 48 companies and 86 other organizations are active in this area of research. There exists a wide variety of potential magnetic labels and even greater range of potential applications of MR contrast agents. However industry and funding agencies have shown substantial



interest, the resources available are limited. It is therefore necessary to direct these resources to the research on the most promising and flexible agents. Gd-DTPA has already gained approval by the US FDA and has started to show its efficacy in clinical practice. However, its toxicity at required dosage and clustered conjugation to carrier molecules limit its applicability. MION has now been well characterized physically and has shown to be a flexible, targetable and effective magnetic label, making it one of the most promising contrast agents to be developed as a universal label.

Based upon the results of this thesis research, the road is now open to the investigation of the conjugation to a large variety of carrier molecules and their efficacies of in vivo targetabilities. Immuno-specific and receptor-specific targeting of liver as well as pancreas, for example will have important clinical applications. In addition, MION can be used as an effective indicator to assess a variety of organ functions and physiological parameters (such as blood flow, perfusion, deoxygenation, etc.). It is not difficult to see that together with more sophisticated imaging software and rapidly improving imaging hardware, MION can be used to evaluate quantitatively as well as qualitatively the physiological functions and pathophysiological conditions.

As a result of this thesis research, it is now possible to synthesize magnetic labels with a well defined size and structure, which could greatly facilitate further research on the mechanism of relaxation of  $T_2$  agents. For example, particles of any size and any magnetic moment can now be synthesized by careful control of the reaction temperature and substitution of Fe (II) by other divalent metal ions. Experimental data acquired from a range of such particles can provide useful insight for the development and verification of relaxation theory of protons.

Finally, the scaled-up production of MION with reliable and uniform properties is an important next step in the development of MION towards clinical applications.

Targeting of MION via specific carrier molecules is becoming and will remain an exciting research field where many results from these research will increase the efficiency and accuracy of clinical diagnosis, providing the possible early detection of diseases. This in turn will allow more effective treatment and improve the quality of life of patients.

---

## References

- Arnold, J. T., S. S. Dharmatti, et al. (1951). J. Chem. Phys. **19**: 507.
- Bean, C. P. and J. D. Livingston (1959). "Superparamagnetism." J. Appl. Phys. **30**(4): 120S-129S.
- Bloch, F., W. W. Hansen, et al. (1946). "Nuclear induction." Phys. Rev. **69**: 127.
- Bogdanov, A., M. Papisov, et al. (1992). Opsonization of dextran-stabilized iron oxides with plasma proteins. 11th Annual Scientific Meeting of Society of Magnetic Resonance in Medicine, Berlin, Germany,
- Brasch, R. (1992). "New Directions in the Development of MR Imaging Contrast Media." **183**(1): 1-11.
- Brasch, R. and H. Bennett (1988). "Considerations in the choice of contrast media in MR imaging." Radiology **166**: 897-899.
- Bydder, G., R. Felix, et al. (1990). Contrast Media in MRI. Bussum, The Netherlands, Medicom.
- Damadian, R. (1971). Science **171**: 1151.
- Dickinson, W. C. (1950). Phys. Rev. **77**: 1151.
- Douglas, S. J., L. Illum, et al. (1984). "Particle size and size distribution of poly(butyl 2-cyanoacrylate) nanoparticles. 1. Influence of physicochemical factors." J. Colloid Interface Sci. **101**: 149.
- Dubois, M., K. A. Gilles, et al. (1956). "Colorimetric Method for Determination of Sugars and Related Substances." Analy. Chem. **28**(3): 350-356.
- Dunn, J. C. Y., R. G. Tomkins, et al. (1991). "Hepatocytes in collagen sandwich: Evidence for transcriptional and translational regulation." :
- Dunn, J. C. Y., R. G. Tomkins, et al. (1991). "Long-term in vitro function of adult hepatocytes in a collagen sandwich configuration." Biotech Prog **7**: 237-245.
- Dunn, J. C. Y., M. L. Yarmush, et al. (1989). "Hepatocyte function and extracellular matrix geometry: long-term culture in a sandwich configuration." FASEB J **3**: 174-177.
- Dutton, A., K. Tokuyasu, et al. (1979). "Iron-dextran antibody conjugates: general method for simultaneous staining of two components in high-resolution immuno-electron microscopy." Proc Natl Acad Sci **76**: 3392-3396.
- Elmore, W. C. (1938). "Ferromagnetic Colloid for Studying Magnetic Structures." Phy. Rev. **54**: 309-310.

- Elmore, W. C. (1938). "The Magnetization of Ferromagnetic Colloids." Phy. Rev. **54**: 1092-1095.
- Elsdale, T. and J. Bard (1972). "Collagen substrate for studies on cell behavior." J. Cell Biol. **54**: 626-637.
- Fisher, M., S. Wall, et al. (1985). "Hepatic vascular anatomy on magnetic resonance imaging." AJR **144**(4): 739-46.
- Gilbert, H. and A. Kagan (1976). Metastases: Incidence, detection and evaluation without histologic confirmation. Fundamental aspects of metastases. Amsterdam, North Holland Publishing Company.
- Haneda, K. and A. H. Morrish (1977). "Magnetite to Maghemite Transformation in Ultrafine Particles." J. de. Phys. supplmt(C1): C1-321- C1-323.
- Haneda, K. and A. H. Morrish (1977). "On the Hyperfine Field of  $\gamma$ -Fe<sub>2</sub>O<sub>3</sub> Small Particles." Phy. Lett. **64A**(2): 259-262.
- Haneda, K. and A. H. Morrish (1977). "Vacancy Ordering in  $\gamma$ -Fe<sub>2</sub>O<sub>3</sub> Small Particles." Solid State Commun. **22**: 779-782.
- Hawkins, J. M. and R. Allen (1991). The Oxford Encyclopedic English Dictionary. Oxford, Clarendon Press.
- Hesselink, J., M. Healey, et al. (1988). "Benefits of Gd-DTPA for MR imaging of intracranial abnormalities." J Comput Assist Tomogr **13**(2): 266-74.
- Housefield, G. N. and J. Ambrose (1973). Br. J. Radiol. **46**: 1016.
- Knight, W. D. (1949). Phys. Rev. **76**: 1259.
- Kreamer, B. L., J. L. Staecker, et al. (1986). "Use of a low-speed, iso-density percoll centrifugation method to increase viability of isolated rat hepatocyte preparations." In Vitro Cell Dev. Biol. **22**: 201-211.
- Kumar, A., D. Welti, et al. (1975). J. Magn. Reson. **18**: 69.
- Lauffer, R. B. (1987). "Paramagnetic Metal Complexes as Water Proton Relaxation Agents for NMR Imaging: Theory and Design." Chem. Rev. **87**: 901-927.
- Lauterbur, P. C. (1973). Nature **242**: 190.
- Lefort, M. J. (1852). "Memoire sur l'oxyde de fer magnetique et ses combinaisons salines." Compt. Rend. Acad. **69** (LXIX)(2): 179-180.
- Lefort, M. J. (1852). "Memoire sur les oxydes ferroso-ferriques et leurs combinaisons." Compt. Rend. Acad. **34** (XXXIV): 488-491.
- Lindström, G. (1950). ibid **78**: 817.

- Misawa, T., K. Hashimoto, et al. (1974). "The Mechanism of Formation of Iron Oxide and Oxyhydroxides in Aqueous Solutions at Room Temperature." Corros. Sci. **14**: 131-149.
- Misawa, T., K. Hashimoto, et al. (1973). "Formation of Fe(II)<sub>1</sub>- Fe(III)<sub>1</sub> Intermediate Green Complex on Oxidation of Ferrous Ion in Neutral and Slightly Alkaline Sulphate Solutions." J. Inorg. Nucl. Chem. **35**: 4167-4174.
- Misawa, T., K. Hashimoto, et al. (1973). "Formation of Fe(II)<sub>1</sub>- Fe(III)<sub>3</sub> Green Complex on Oxidation of Ferrous Ion in Perchloric Acid Solution." J. Inorg. Nucl. Chem. **35**: 4159-4166.
- Morup, S. and H. Topsoe (1976). "Mössbauer Studies of Thermal Excitations of Magnetically Ordered Microcrystals." Appl. Phys. **11**: 63-66.
- Proctor, W. C. and F. C. Yu (1950). Phys. Rev. **77**: 717.
- Purcell, E. M., H. C. Torrey, et al. (1946). "Resonance absorption by nuclear magnetic moments in a solid." Phys. Rev. **69**: 37.
- Rabi, I. I., S. Millman, et al. (1939). Phys. Rev. **55**: 526.
- Seglen, P. O. (1976). "Preparation of isolated rat liver cells." Methods Bio. **13**: 29-83.
- Shen, T., R. Weissleder, et al. (1991). Macromolecular and particulate iron oxide compounds for MR imaging. 10th Annual Scientific Meeting of Society of Magnetic Resonance in Medicine, San Francisco, CA,
- Smit, J. and H. P. J. Wijn (1959). Ferrites. New York Eindhoven, John Wiley & Sons.
- Unger, E., P. MacDougall, et al. (1989). "Liposomal Gd-DTPA: effect of encapsulation on enhancement of hepatoma model by MRI." Magn Reson Imaging **7**(4): 417-23.
- Verwey, E. J. W. and E. L. Heilmann (1947). "Physical Properties and Cation Arrangement of Oxides with Spinel Structures." J. Chem. Phys. **15**(4): 174-180.
- Weinmann, H., R. Brasch, et al. (1984). "Characteristics of Gd-DTPA complex: a potential NMR contrast agent." AJR **142**: 619-25.

## Appendix (Facilities)

The SQUID magnetometer and Mössbauer Central Facility at MIT has operated since the mid-1980's as an interdisciplinary shared research resource center for microscopic magnetic characterization of materials.

The Mössbauer spectroscopy laboratory consist of two conventional constant acceleration spectrometers equipped with Janis Research Corp. "Supervaritemp" cryogenic dewars. One is a zero-field variable temperature system with a Lake Shore Cryotronic model DRC-70C temperature controller capable of maintaining sample temperatures of range  $1.6 \leq T \leq 300$  K with in 0.1K. The other, in addition to temperature variation with a TRI-Research T-2000 temperature controller with  $1.6 \leq T \leq 400$  K, is also equipped with a Nb<sub>3</sub>Sn superconducting magnet by American Magnetic Corp. capable of producing a longitudinal (i.e. parallel to the direction of the g-ray) magnetic field of  $H_0 \leq 8$  T. Standard peripheral electronics, pumping stations, data acquisition and processing systems are also available. Elaborate software for detailed Mössbauer spectral fitting and analysis has been developed and operates on a Digital VAX740-VMS system.

The SQUID magnetometer is by SHE Corporation with temperature and field variation of  $1.6 \leq T \leq 400$  K and  $H_0 \leq 5$  T. It has a magnetic moment sensitivity down to  $10^{-6}$  emu. It is computer interfaced with a Hewlett-Packard 86B computer system equipped with two HP-9121 disk drives. Data acquisition may be performed under manual and computer control. The latter mode of operation allows lengthy data acquisition to be done automatically under continuous operation.

The MGH-NMR Center is comprised of clinical, research, education and administration areas. The research area contains a whole body echo planar imager (General Electric and Advanced NMR systems, Woburn), a 2.0 T small magnet laboratory, a 4.7 T laboratory (CSI, General Electric Corp., Fremont, Ca), a 6.0 T (Oxford Instrument Ltd., Osney Mead, UK) and a 9.4 T laboratory (Bruker 9.4 T MSL system). There are also multiple 0.47 T tabletop PC20 Minispec NMR instruments (IBM, Danburg, CT), biochemistry, chemistry, immunology, surgery and computer laboratories within the facility.